Supplementary Information

Salting-in electrolyte enables reversible heavy p-block electrochemistry in water

Yang-Feng Cui[1,6], Ming Zhang[3,6], Yunhai Zhu[4], Haobin Song[1,5], Yifan Li[1], Nan Zhao[5], Wenjing Li[5], Ying Shirley Meng[2✉], & Hui Ying Yang[1✉]

[1]Department of Materials Science and Engineering, College of Design and Engineering, National University of Singapore, Singapore 117575, Singapore.

[2]Pritzker School of Molecular Engineering, University of Chicago, Chicago, Illinois 60637, United States

[3]School of Materials and Energy, University of Electronic Science and Technology of China, Chengdu 611731, China.

[4]State Key Laboratory of New Textile Materials and Advanced Processing, Wuhan Textile University, Wuhan 430200, China.

[5]Pillar of Engineering Product Development, Singapore University of Technology and Design, Singapore 487372, Singapore.

[6]These authors contributed equally: Yang-Feng Cui and Ming Zhang.

✉e-mail: shirleymeng@uchicago.edu; yanghuiying@nus.edu.sg

This file includes: Supplementary Figs. 1−80, Notes 1−10, Tables 1−4 and References

Table of Contents:

Supplementary Note 1. First-principles exploration of cation–anion–H_2O coordination (Supplementary Figs. 1–23)

Supplementary Note 1.1. ESP of HPE cations and auxiliary anions (Supplementary Fig. 1)

The ESP of a molecule arises from the combined influence of its nuclei and electrons at every point in the surrounding space[1]. At any specific location, the value of ESP reflects the net contribution from all nuclei and electrons. Whether ESP is positive or negative in a given region depends on which effect dominates: the attractive potential generated by the positively charged nuclei or the repulsive potential produced by the electron cloud. Areas of positive electrostatic potential tend to attract nucleophilic (electron-rich) sites, whereas negative potential regions preferentially interact with electrophilic (electron-deficient) sites. A key characteristic of ESP is commonly visualized on the molecular surface defined by an outer electron density contour, typically 0.001 a.u. (electrons bohr^{-3}). We first computed the ESP of a series of HPE cations to examine their intrinsic electrophilic strength. Because these ions are nearly spherical, the values of ESP on their molecular surfaces are relatively uniform, enabling a qualitative ordering of their electrostatic potential magnitudes. As shown in left of Fig. 1d, the ESP follows the trend:

$$Pb^{2+} < Sn^{2+} < Bi^{3+} < Sb^{3+} < Te^{4+} < Se^{4+}$$

increasing from 0.544642 a.u. for Pb^{2+} to 1.3587 a.u. for Se^{4+}. This reflects the combined effect of increasing formal charge and decreasing effective ionic volume along the series. H_2O molecule is an amphoteric molecule that exhibits both positive and negative electrostatic potential regions: the most negative ESP is located at the oxygen lone-pair site (–0.063 a.u.), while the most positive ESP is found at the hydrogen sites (0.083 a.u.). This dual character enables water to interact electrostatically with both cationic and anionic species. In this context, the positive ESP of HPE cations interacts attractively with the electron-rich oxygen sites of H_2O molecules. The strength of this interaction correlates with the ESP magnitude of HPE cations, being weakest for Pb^{2+} and strongest for Se^{4+}, which helps explain the increasing electrostatic driving force for hydration and hydrolysis along the series.

After examining the ESP characteristics of HPE cations and H_2O, we next consider the auxiliary anions, whose size and charge distribution play a decisive role in governing their electrostatic interactions with counter cations and H_2O molecules (right Fig. 1c, and Supplementary Fig. 1). Figure 1f correlates each molecular vdW volume of anions with its ESP extrema, providing a compact descriptor of anion electrostatics. The vdW volume denotes the effective three-dimensional space occupied by an anion, reflecting both steric size and the spatial extent of charge delocalization. In general, smaller, charge-localized anions show more negative ESP, whereas larger, charge-delocalized anions exhibit weaker negative ESP, establishing a clear inverse relationship between size and ESP magnitude. Halide anions fall in the strongly negative, localized regime with low surface anisotropy: Cl^- has a concentrated negative

ESP of –0.233 a.u., while Br^- and I^- are slightly less negative (–0.216 and –0.197 a.u., respectively), consistent with their larger radii and greater polarizability that spread charge over a broader surface. Symmetric oxyanions such as trigonal NO_3^- and tetrahedral ClO_4^- distribute charge over multiple oxygen centers, yielding intermediate lowest-ESP values (–0.227 and –0.198 a.u., respectively) and low-to-moderate anisotropy; although weaker Coulombic partners than the Cl^-, they still present well-defined nucleophilic patches at oxygen. OAc^- is distinctly anisotropic: the carboxylate oxygens exhibit a deep lowest ESP of –0.245 a.u., whereas the methyl terminus is much less negative (lowest ESP = –0.120 a.u.). This spatial heterogeneity produces directional ESP—strong attraction at oxygen but weak interaction at the hydrocarbon end—that can influence interfacial orientation and ligand exchange. Fluorinated pseudo-halides, including tetrahedral BF_4^- and octahedral PF_6^-, are nearly isotropic; their lowest-ESP values (–0.216 a.u. and –0.196 a.u., respectively) fall within a moderately negative range, reflecting extensive charge delocalization over electronegative fluorine atoms. Finally, sulfonyl anions localize negative potential at S=O sites while distributing the remainder over fluorinated or alkyl peripheries: MSA^- and OTf^- show intermediate lowest-ESP values (−0.216 and −0.196 a.u., respectively) with clear anisotropy between sulfonyl lobes and alkyl/fluoroalkyl termini, whereas $TFSI^-$ lies at the largest-volume, softest extreme with a broad ESP span from –0.184 to –0.087 a.u., arising from conformational flexibility and charge delocalization across two sulfonyl groups and a perfluoroalkyl backbone.

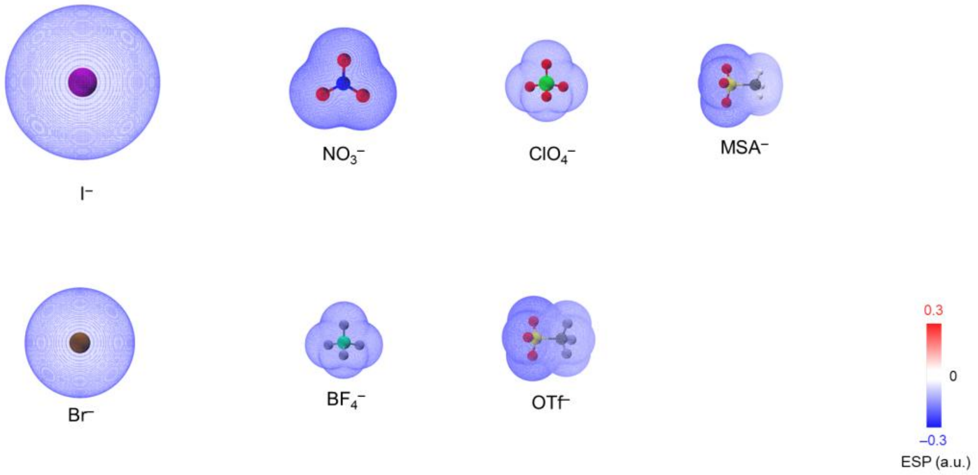

Supplementary Fig. 1 | Surface ESP distributions of different anions.

Supplementary Note 1.2. AIMD simulations of hydrated auxiliary cation structures (Supplementary Figs. 2, 3)

To preliminarily screen potential auxiliary cations for their hydration behavior, we performed AIMD simulations on a series of representative ions in bulk water. The examined cations encompass monovalent alkali metal ions (Li^+, Na^+, and K^+), divalent main group ions (Be^{2+}, Mg^{2+}, and Ca^{2+}), first-row transition-metal ions (Cr^{2+}, Mn^{2+}, Fe^{2+}, Co^{2+}, Ni^{2+}, Cu^{2+}, and Zn^{2+}), and trivalent Al^{3+}. Supplementary Fig. 2 presents the cation-oxygen radial distribution functions (RDFs) and corresponding CN profiles, averaged over the trajectories, while Supplementary Fig. 3 displays representative snapshots of the resulting hydration structures. Distinct and systematic trends are observed across the auxiliary cation series (Supplementary Fig. 2). Alkali monovalent ions exhibit a gradual broadening of the g(r) peak and an increase in CN from Li^+ (CN = 4.25) to K^+ (CN = 6.60), consistent with the progressive weakening of electrostatic interactions and the formation of more diffuse hydration shells as ionic radius increases. Be^{2+} forms a compact tetrahydrate $[Be(H_2O)_4]^{2+}$ (CN = 4.04) with a sharp and narrow g(r) peak, reflecting its small ionic size and high charge density. Mg^{2+} shows a well-defined first-shell peak and CN = 6.00, characteristic of a stable octahedral solvation structure of $[Mg(H_2O)_6]^{2+}$. Ca^{2+}, however, exhibits distinctly different hydration behavior. Its g(r) profile features a broader first peak, and the CN lies between 7 and 8 (7.34 in the present trajectory), indicating a flexible hydration environment capable of accommodating both seven- and eight-coordination structures. This flexibility is corroborated by Supplementary Fig. 3, which reveals both $[Ca(H_2O)_7]^{2+}$ and $[Ca(H_2O)_8]^{2+}$ structures. In contrast, transition-metal (TM) ions (Mn^{2+}, Fe^{2+}, Co^{2+}, Ni^{2+}, and Zn^{2+}) display sharp first-shell peaks and CN values close to 6, indicative of rigid octahedral hydration environments. However, Cr^{2+} shows a lower average CN of 5.03, likely reflecting a less stable hydration shell with dynamic fluctuations associated with its Jahn-Teller activity, while the slightly reduced CN of Cu^{2+} (5.77) is consistent with the well-known axial elongation induced by Jahn-Teller distortion. Al^{3+} exhibits the sharpest first-shell peak among all cations, with CN = 6.00, signifying a strongly bound and geometrically constrained octahedral hydration shell.

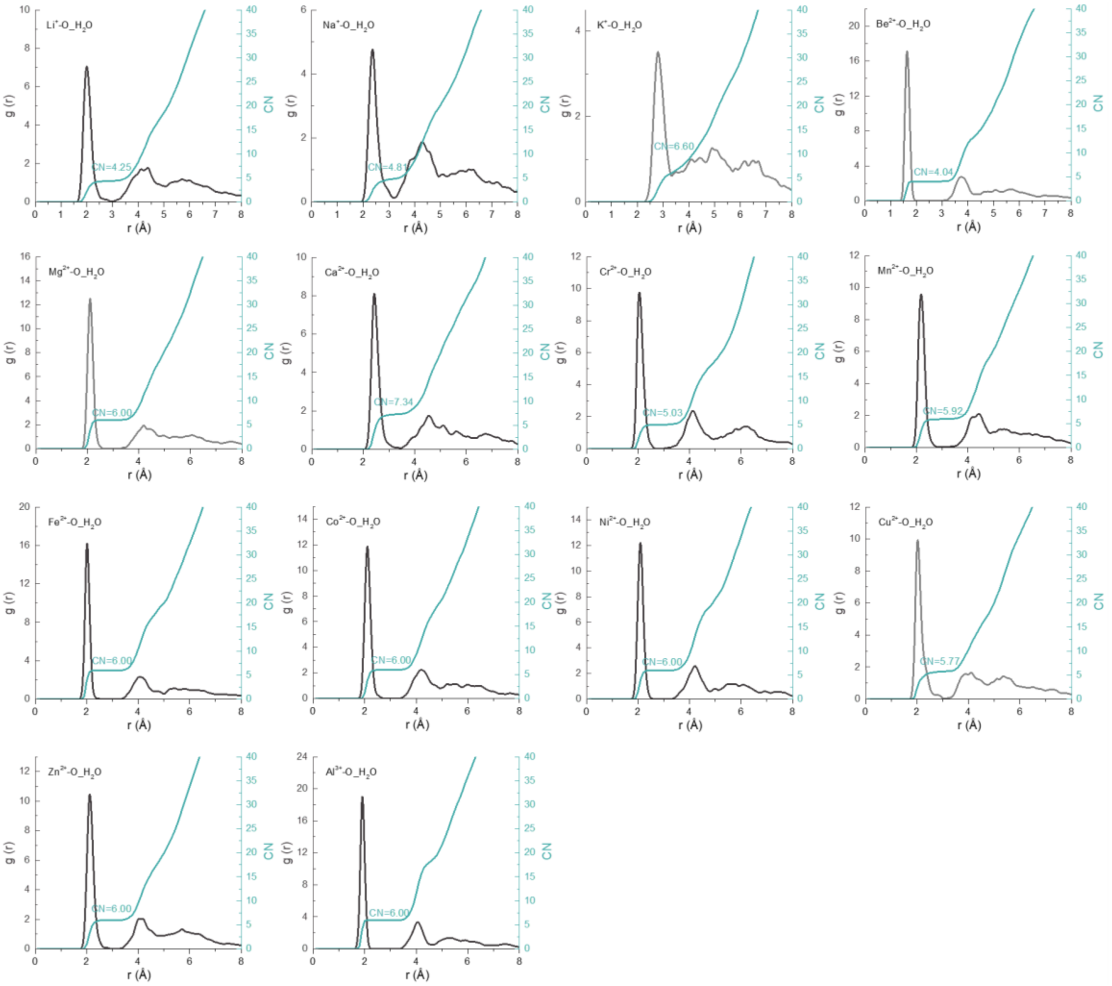

Supplementary Fig. 2 | Hydrated structures of auxiliary cations in water. RDFs and CNs between cations and O atoms of H_2O, obtained from AIMD simulations of a single cation solvated by 56 H_2O molecules.

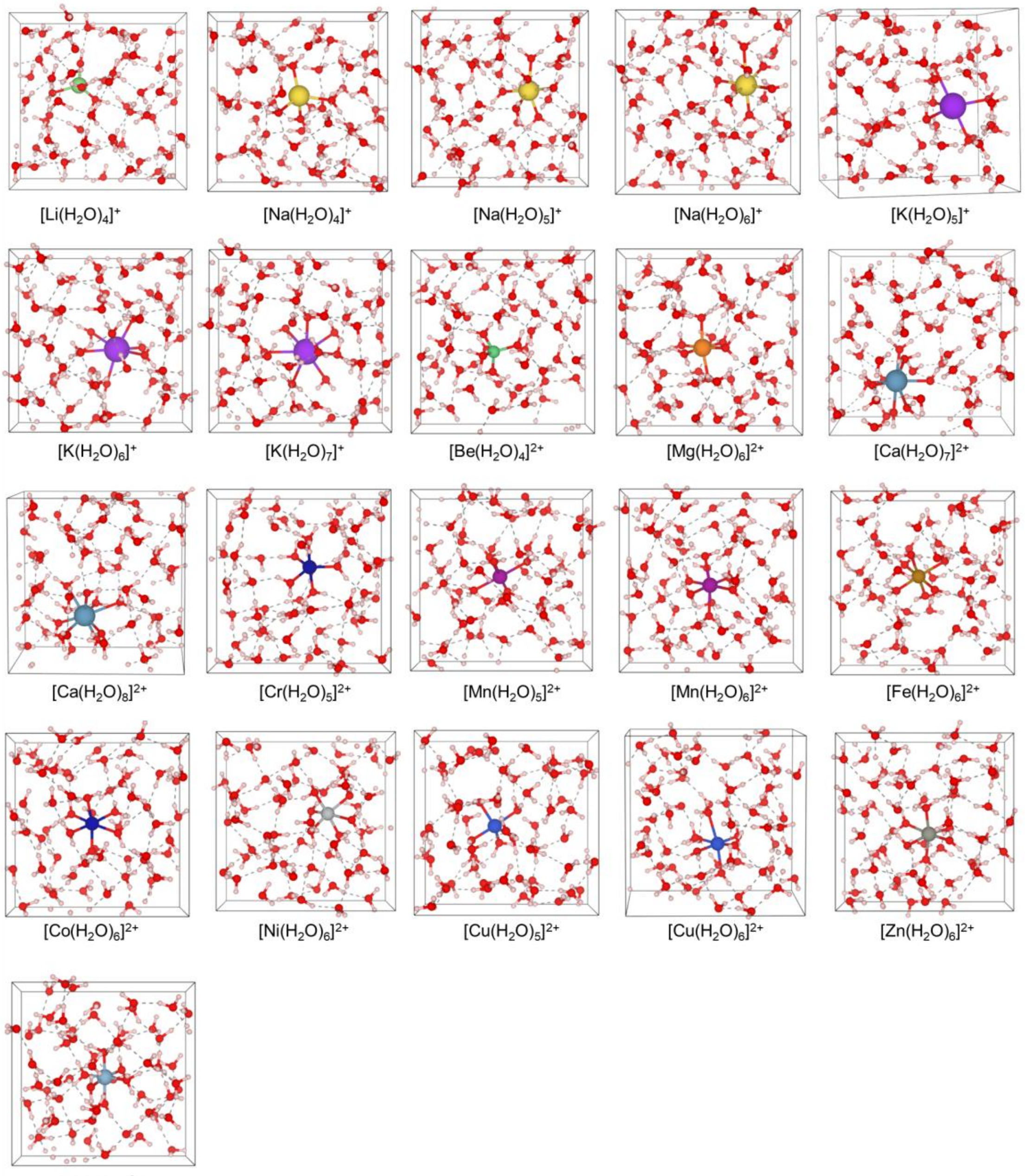

$[Li(H_2O)_4]^+$ $[Na(H_2O)_4]^+$ $[Na(H_2O)_5]^+$ $[Na(H_2O)_6]^+$ $[K(H_2O)_5]^+$

$[K(H_2O)_6]^+$ $[K(H_2O)_7]^+$ $[Be(H_2O)_4]^{2+}$ $[Mg(H_2O)_6]^{2+}$ $[Ca(H_2O)_7]^{2+}$

$[Ca(H_2O)_8]^{2+}$ $[Cr(H_2O)_5]^{2+}$ $[Mn(H_2O)_5]^{2+}$ $[Mn(H_2O)_6]^{2+}$ $[Fe(H_2O)_6]^{2+}$

$[Co(H_2O)_6]^{2+}$ $[Ni(H_2O)_6]^{2+}$ $[Cu(H_2O)_5]^{2+}$ $[Cu(H_2O)_6]^{2+}$ $[Zn(H_2O)_6]^{2+}$

$[Al(H_2O)_6]^{3+}$

Supplementary Fig. 3 | Representative hydrated cation structures. Snapshots from AIMD simulations illustrating the resulting hydration configurations of auxiliary cations in water.

Supplementary Note 1.3. DFT-optimized hydration structures and binding energies of auxiliary cations (Supplementary Figs. 4, 5)

Building on the AIMD screening (Supplementary Figs. 2, 3), we next performed DFT geometry optimizations for all hydrated solvation structures sampled along the trajectories to quantify first-shell coordination and binding strength. For each cation, low-energy hydrated structures consistent with the CN of AIMD were optimized, and the total hydration binding energy was calculated relative to isolated cations and H_2O molecules (Supplementary Fig. 4). This procedure enables a direct comparison of preferred CNs and first-shell binding strengths across the auxiliary cation series. All AIMD-identified solvation structures were successfully optimized without H_2O molecules escaping to outer solvation shells, indicating that the sampled hydration structures correspond to stable local minima. To further rationalize the trends, we analyzed the DFT results in conjunction with ionic charge density and ionic radii (Supplementary Figs. 4, 5)[2]. Monovalent alkali ions (Li^+, Na^+ and K^+) exhibit low total hydration binding energies (–3.85 to –5.00 eV), reflecting their intrinsically weak electrostatic interactions with H_2O due to low charge densities. Among them, Li^+, with the smallest ionic radius, stabilizes a compact tetrahydrate $[Li(H_2O)_4]^+$ structure, whereas K^+, with a much larger ionic radius, can accommodate up to seven water molecules ($[K(H_2O)_7]^+$). However, its low charge density results in a diffuse hydration shell and weak binding energies. In contrast, the divalent Be^{2+}, Mg^{2+} and Ca^{2+} series exhibits a systematic increase in CNs of H_2O molecules from 4 to 8 with increasing ionic radius. Be^{2+}, with the highest charge density and smallest radius, stabilizes a tight tetrahedral hydration shell $[Be(H_2O)_4]^{2+}$ with the most negative binding energy (–17.58 eV) among the three. By comparison, TM ions (Cr^{2+}, Mn^{2+}, Fe^{2+}, Co^{2+}, Ni^{2+}, Cu^{2+} and Zn^{2+}) cluster in a region of intermediate charge density and ionic radius similar to Mg^{2+} (Supplementary Fig. 5). Correspondingly, they exhibit comparable binding energies (–12.7 to –16.4 eV), consistent with their well-known rigid hydration environments. Al^{3+}, distinguished by its small radius and very high charge density, forms a strongly bound $[Al(H_2O)_6]^{3+}$ octahedral structure with the most negative binding energy of –31.66 eV among all examined structures. Taken together, these results highlight Ca^{2+} as a unique case: owing to its relatively high charge density and ample spatial capacity for accommodating H_2O molecules, Ca^{2+} can achieve high hydration numbers (up to eight) while maintaining substantial binding strength and symmetric coordination. This distinctive combination of high CN and strong hydration endows Ca^{2+} with an exceptional ability to sequester bulk water through hydration, making it an optimal auxiliary cation candidate for the dual-salt design strategy.

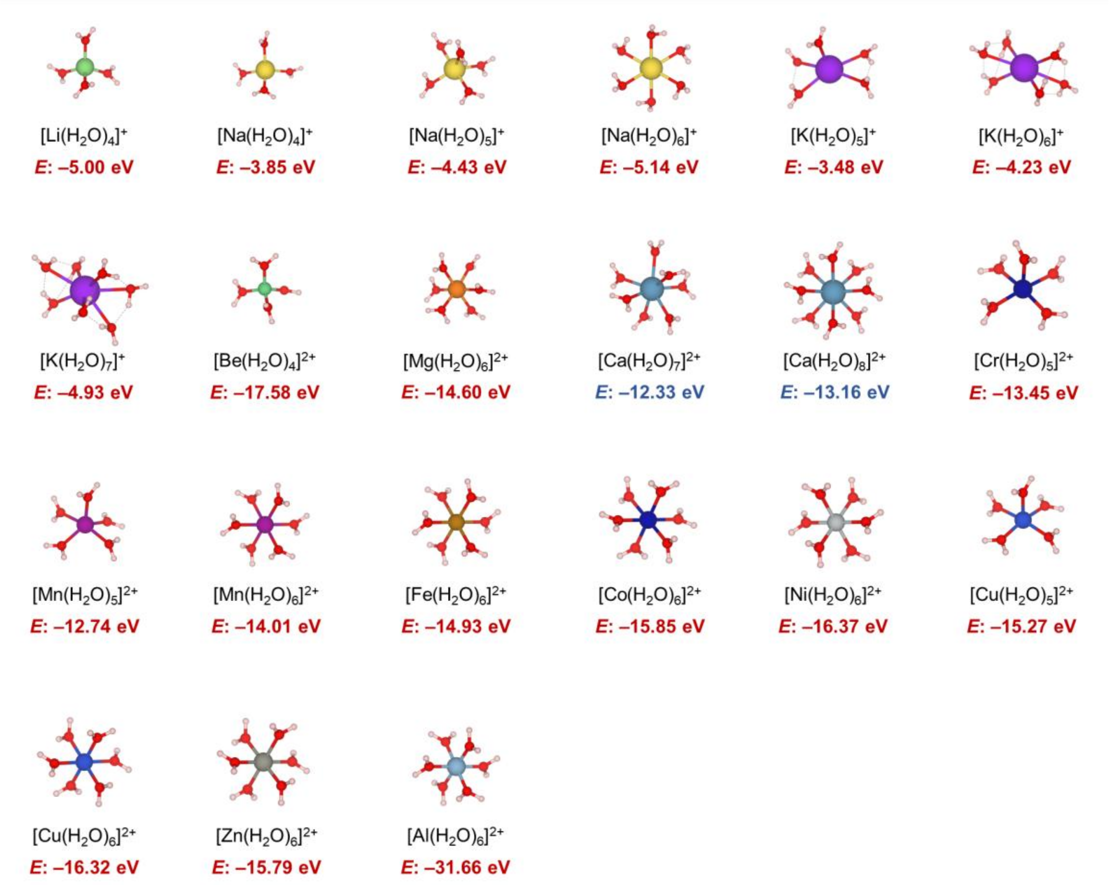

Supplementary Fig. S4 | DFT-optimized hydrated cation structures. Representative optimized configurations of hydrated cations and their corresponding binding energies (*E*).

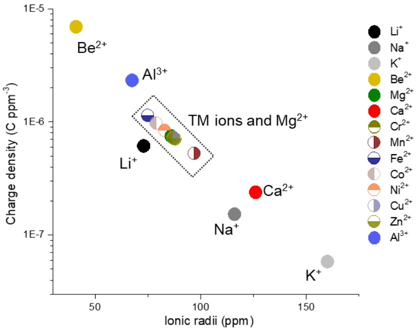

Supplementary Fig. S5. | Basic parameters of auxiliary cations used in this work. Ionic radii and charge density of Li^+, Na^+, K^+, Be^{2+}, Mg^{2+}, Ca^{2+}, Cr^{2+}, Mn^{2+}, Fe^{2+}, Co^{2+}, Ni^{2+}, Cu^{2+}, Zn^{2+} and Al^{3+}.

Supplementary Note 1.4. DFT-optimized structure and binding energy for anion-coordinate Ca^{2+} and Pb^{2+} structures (Supplementary Figs. 6–8)

Guided by the above analysis, we treat the cationic ESP as a first-order predictor of anion affinity: a more positive ESP strengthens the Coulombic driving force for binding. Accordingly, any anion that already prefers Pb^{2+} over Ca^{2+} should bind higher-ESP HEP cations (Sn^{2+}, Bi^{3+}, Sb^{3+}, Te^{4+} and Se^{4+}) at least as strongly—typically more so—thereby validating our screening principle. Ca^{2+} and Pb^{2+} thus serve as complementary benchmarks. Ca^{2+}, selected as the auxiliary cation in our dual-salt design, is strongly hydrated yet weakly ion-paired; it is therefore sufficient that its anion affinity remains lower than that of the HPE cations so the anion stays labile while Ca^{2+} sequesters water. Pb^{2+}, in contrast, exhibits the lowest ESP among the HPE cations considered; if an anion binds Pb^{2+} more strongly than Ca^{2+}, the same anion will, by electrostatic continuity, bind all higher-ESP HPE cations at least as strongly. For each anion, we identified the most negative ESP site and used that locus as the coordination handle to the metal center. Stepwise coordination, MX_n^{2-n} with n = 1–4 (M^{2+} = Ca^{2+} or Pb^{2+}; X = Cl$^-$, Br$^-$, I$^-$, ClO$_4^-$, NO$_3^-$, OAc$^-$, BF$_4^-$, PF$_6^-$, MSA$^-$, OTf$^-$, and TFSI$^-$), were constructed and DFT-optimized to local minima (Supplementary Figs. 6–8). The corresponding binding energies quantify the interaction strength between the central cation and its coordinating anions; more negative values denote stronger coordination. We therefore computed these energies for all complexes. For every anion coordinated, increasing the CN from one to three drives binding energy monotonically to its most negative value, whereas adding a fourth ligand causes a rebound (less negative binding energy). This universal minimum at the three-coordinate state reflects the balance between cation-anion attraction and inter-ligand crowding/charge-delocalization penalties, and holds for both Ca^{2+} and Pb^{2+}. Relative to the corresponding aqua complexes, all anion-coordinate species are markedly more stabilized, confirming that direct anion-cation pairing outcompetes hydration at matched CNs. Subsequently, we constrained anion coordination to three to differentiate among ligand families. For bulky or charge-delocalized anions (X$^-$: ClO$_4^-$, NO$_3^-$, OAc$^-$, BF$_4^-$, PF$_6^-$, MSA$^-$, OTf$^-$, and TFSI$^-$; Supplementary Figs. 7, 8), the anion-coordinate [CaX$_3$]$^-$ are consistently more stable (more negative binding energies) than [PbX$_3$]$^-$, indicating that Pb^{2+} does not outcompete Ca^{2+} for these ligands. In sharp contrast, for halide anions the preference reverses: [PbCl$_3$]$^-$, [PbBr$_3$]$^-$, and [PbI$_3$]$^-$ are more stable than [CaCl$_3$]$^-$, [CaBr$_3$]$^-$, and [CaI$_3$]$^-$, with Cl$^-$ giving the most negative binding energy and therefore the strongest coordination (Supplementary Fig. 6). Therefore, based on DFT-optimized structures, our binding-energy screening identifies Cl$^-$ as the optimal anion for Pb^{2+} coordination: the three-ligand (n = 3) complex attains the most negative binding energy, whereas the corresponding Ca^{2+}-Cl$^-$ complexes are less stabilized. In short, Cl$^-$ preferentially coordinates to Pb^{2+} and interacts comparatively weakly with Ca^{2+} (Supplementary Fig. 6b).

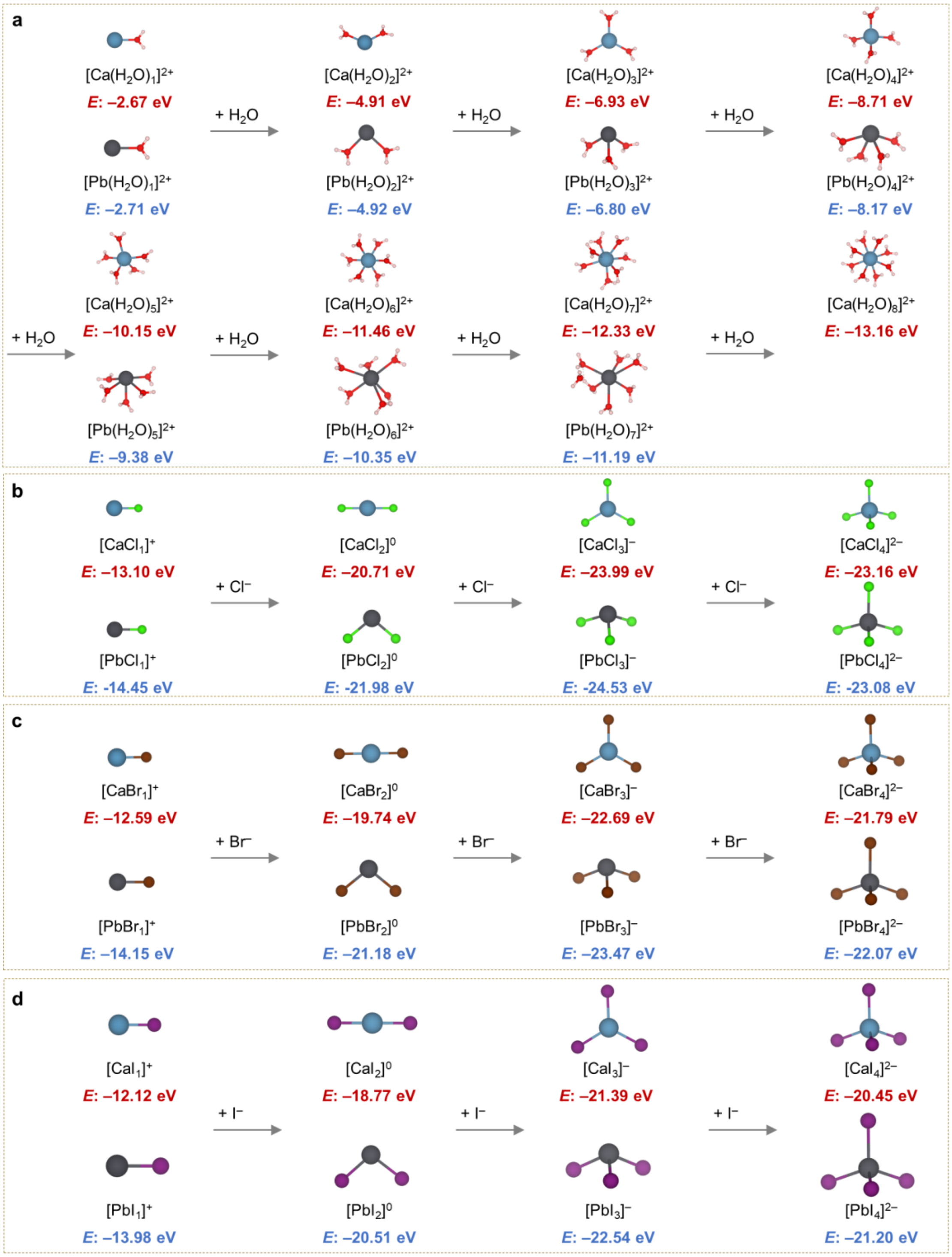

Supplementary Fig. 6 | DFT simulations of hydrated and halide-coordinate clusters. a–d, Representative optimized structures using Ca^{2+} and Pb^{2+} as coordination center, together with the corresponding binding energies (*E*) for stepwide coordination with H_2O (a), Cl^- (b), Br^- (c), and I^- (d).

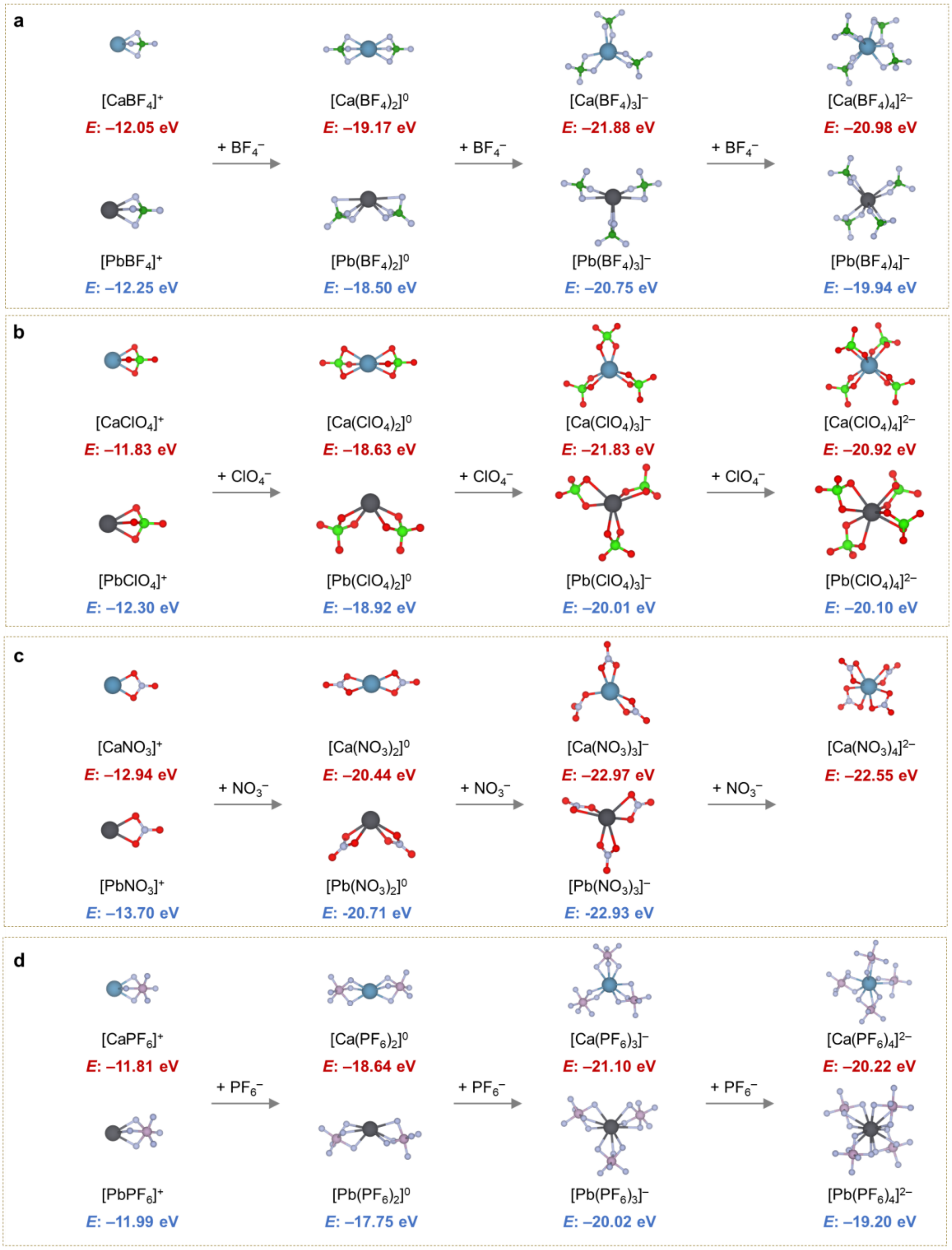

Supplementary Fig. 7 | DFT simulations of anion-coordinate clusters. a–d, Representative optimized structures using Ca^{2+} and Pb^{2+} as coordination center, together with the corresponding binding energies (*E*) for stepwide coordination with BF_4^- (a), ClO_4^- (b), NO_3^- (c), and PF_6^- (d).

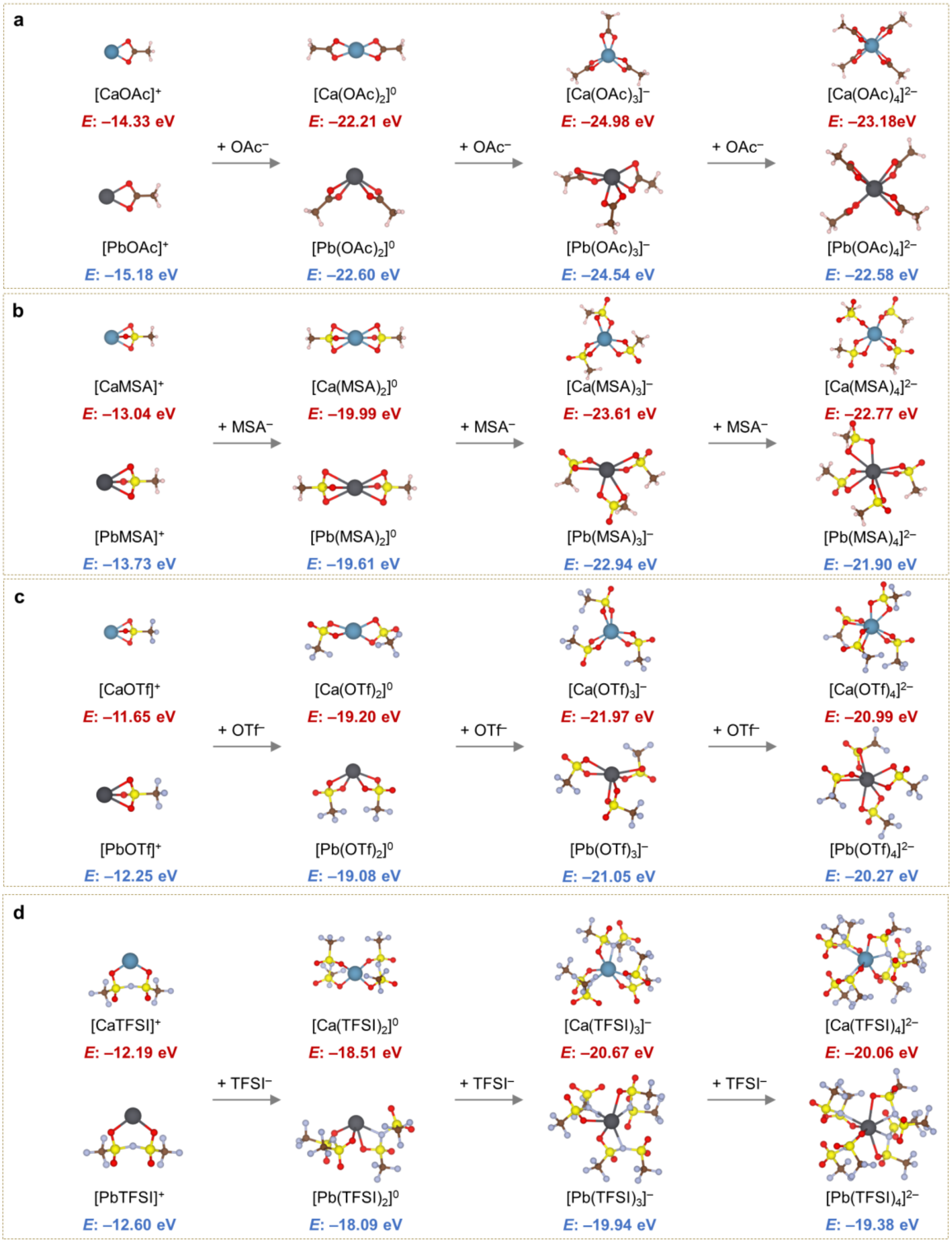

Supplementary Fig. 8 | DFT simulations of anion-coordinate clusters. a–d, Representative optimized structures using Ca^{2+} and Pb^{2+} as coordination center, together with the corresponding binding energies (*E*) for stepwide coordination with OAc^- (a), MSA^- (b), OTf^- (c), and $TFSI^-$ (d).

Supplementary Note 1.5. ELF analyses for anion-coordinate Ca^{2+} and Pb^{2+} structures (Supplementary Figs. 9–11)

DFT-optimized structures across the anion-coordinated series reveal a consistent divergence between Ca^{2+} and Pb^{2+} (Supplementary Figs. 6–8). Ca^{2+} complexes adopt near-symmetric arrangements at all CNs, in line with a dominantly electrostatic, hydration-favored cation. By contrast, Pb^{2+} complexes are asymmetric at low coordination: with two ligands the coordination set bends to one side, and with three ligands a clear trigonal-pyramidal structure emerges; crowding at $n = 4$ diminishes the asymmetry. To rationalize these DFT-optimized structures, we analyzed the ELF, an orbital-based descriptor constructed from the Pauli kinetic-energy density relative to a uniform-electron-gas reference, which reveals regions of like-spin electron localization. The ELF maps (isosurface = 0.5) rationalize these structures (Supplementary Figs. 9–11): in Pb^{2+} complexes a prominent monosynaptic basin appears on the side opposite the ligands—the stereochemically active $6s^2$ lone pair—which steers the coordination into hemidirected arrangements (bent for $n = 2$; trigonal-pyramidal for $n = 3$). Upon moving to $n = 4$, this basin shrinks and reorients under crowding, explaining the loss of strong asymmetry. In Ca^{2+} complexes, by contrast, no cation-adjacent basin is observed; ELF is dominated by anion-localized shells, consistent with ionic, weakly directional Ca^{2+}–anion interactions. Using the chloride-coordinate cation as a representative example, the Cl^- series makes the contrast explicit. For Ca^{2+}, the progression is $[CaCl]^+$ (colinear one-ligand arrangement) → linear $[CaCl_2]^0$ → trigonal-planar $[CaCl_3]^+$ → tetrahedral $[CaCl_4]^{2-}$, reflecting the symmetry-seeking coordination as ligation increases. For Pb^{2+}, the sequence is $[PbCl]^+$ (colinear) → bent $[PbCl_2]^0$ → trigonal-pyramidal $[PbCl_3]^-$ → near-tetrahedral $[PbCl_4]^{2-}$, the bend and pyramid being direct geometric signatures of the stereochemically active $6s^2$ lone pair revealed by ELF.

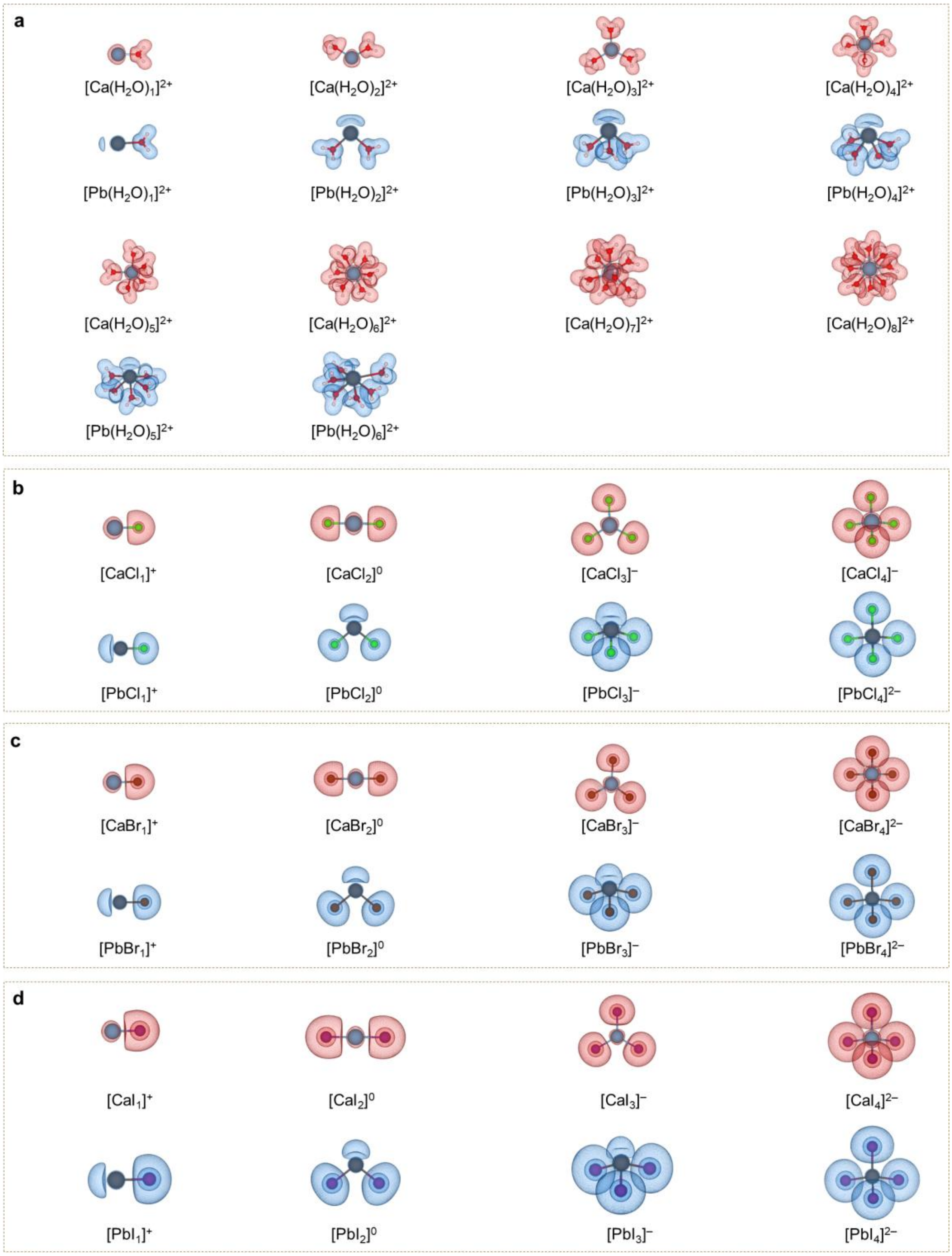

Supplementary Fig. 9 | ELF characterization of hydrated and halide-coordinate clusters. a–d, ELF isosurfaces (value = 0.5) of DFT-optimized Ca^{2+}- and Pb^{2+}-centered clusters showing stepwise coordination with H_2O (a), Cl^- (b), Br^- (c), and I^- (d).

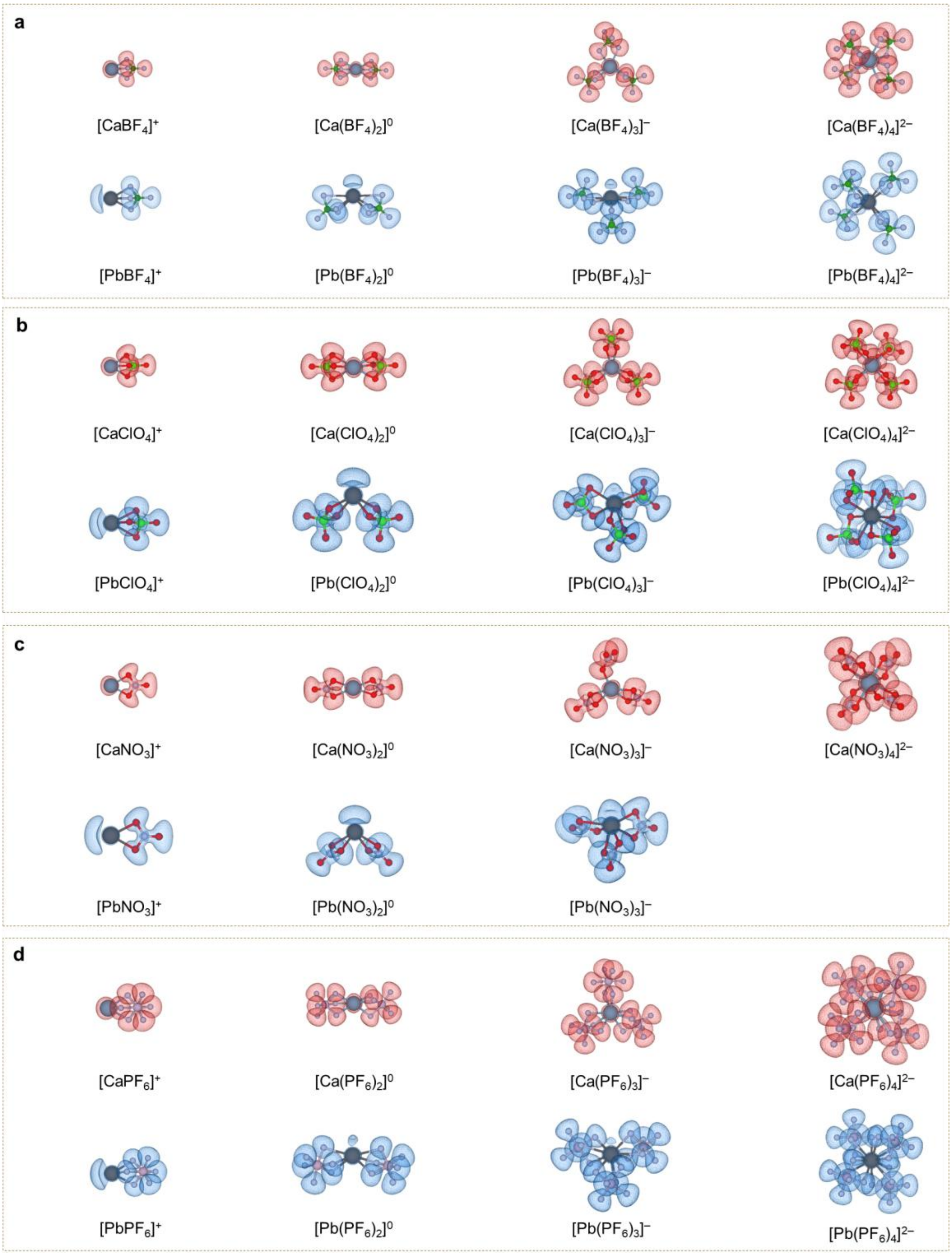

Supplementary Fig. 10 | ELF characterization of anion-coordinate clusters. a–d, ELF isosurfaces (value = 0.5) of DFT-optimized Ca^{2+}- and Pb^{2+}-centered clusters showing stepwise coordination with stepwise coordination of BF_4^- (a), ClO_4^- (b), NO_3^- (c), and PF_6^- (d).

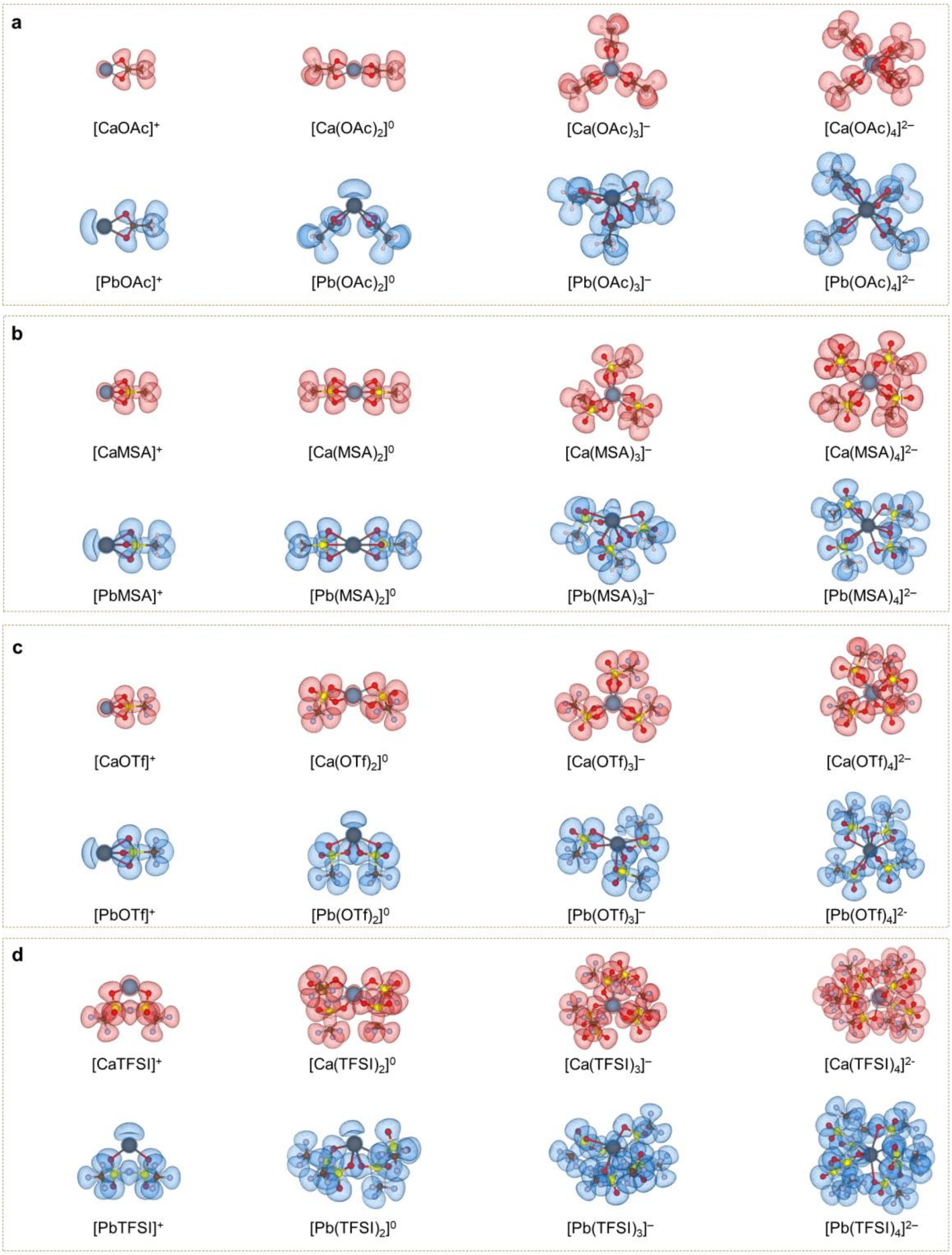

Supplementary Fig. 11 | ELF characterization of anion-coordinate clusters. a–d, ELF isosurfaces (value = 0.5) of DFT-optimized Ca^{2+}- and Pb^{2+}-centered clusters showing stepwise coordination with stepwise coordination of OAc$^-$ (a), MSA$^-$ (b), OTf$^-$ (c), and TFSI$^-$ (d).

Supplementary Note 1.6. IGMH analyses for anion-coordinate Ca^{2+} and Pb^{2+} structures (Supplementary Figs. 12–14)

ELF analysis identifies a stereochemically active $6s^2$ lone pair as the origin of asymmetry in Pb^{2+} complexes, whereas Ca^{2+} lacks any cation-adjacent basin and coordinates in a comparatively symmetric, holodirected manner. To translate this electronic picture into a spatially resolved measure of interactions, we use the IGMH analyses. In IGMH, $\delta g_{\mathrm{inter}}$ acts as a contact detector: after decomposing the total electron density into Hirshfeld fragments, $\delta g_{\mathrm{inter}}$ reports the deviation from the gradient expected for non-interacting fragments; regions with nonzero $\delta g_{\mathrm{inter}}$ define interfragment contacts and are rendered as $\delta g_{\mathrm{inter}}$ isosurfaces. The nature of each contact is read from the $sign(\lambda_2)\rho$ coloring on those surfaces (non-covalent interaction convention): deep blue (negative $sign(\lambda_2)\rho$ at non-negligible density) indicates shared-shell character with appreciable covalency; pale blue/teal (slightly negative at low density) corresponds to closed-shell, weakly attractive contacts (e.g., ionic, hydrogen/halogen bonds); green (≈ 0) denotes dispersion-dominated vdW contacts; red (positive) signifies steric repulsion. Crucially, the color encodes interaction type, not strength. Interaction strength should be inferred from the $\delta g_{\mathrm{inter}}$ amplitude (e.g., peak height or the size/compactness of the isosurface at a fixed isovalue). At comparable thresholds, a more negative $sign(\lambda_2)\rho$ at the $\delta g_{\mathrm{inter}}$ maximum indicates a more attractive character, whereas a more positive value indicates greater repulsion. To map how this electronic contrast translates into specific contacts, we produced IGMH maps across all anion-coordinate systems with $\delta g_{\mathrm{inter}}$ isosurfaces at 0.01 a.u., colored by $sign(\lambda_2)\rho$ (Supplementary Figs. 12–14). Two features stand out. Although total binding energy reflects the net stabilization of each complex, the IGMH maps resolve per-contact strength. From $n = 3$ to 4, the blue domains at individual cation-anion contacts dilute and partially shift toward green, i.e., the fourth ligand weakens each single ion-pair interaction. For example, $[PbCl_3]^-$ shows compact $\delta g_{\mathrm{inter}} = 0.01$ a.u. lobes with deep-blue $sign(\lambda_2)\rho$ sign at each Pb-Cl contact, whereas in $[PbCl_4]^{2-}$ the individual 0.01-isosurface lobes contract and the coloring shifts toward green, indicating weaker, more dispersion-like contacts (bottom row of Supplementary Fig12b). Analogous behavior appears across other anions and for Ca^{2+} (top row of Supplementary Fig12b). This local weakening rationalizes why the global energy minimum occurs at $n = 3$ in our binding-energy analysis (Supplementary Figs. 6–8). The IGMH maps also rationalize ligand-class selectivity at Pb^{2+}. The stereochemically active $6s^2$ lone pair imposes a hemidirected field that disfavors bulky, charge-delocalized anions (ClO_4^-, NO_3^-, OAc^-, BF_4^-, PF_6^-, MSA^-, OTf^-, and $TFSI^-$). At $n = 3$, these ligands frequently adopt open-cage arrangements, in which their $V_{\mathrm{s,min}}$ sites cannot fully align with Pb^{2+}. In the IGMH maps ($\delta g_{\mathrm{inter}}$ fixed at 0.01 a.u.), this manifests as compact deep-blue patches confined to the hemisphere opposite the lone pair, while the lone-pair hemisphere shows only fragmented green envelopes, i.e., dispersion-dominated contacts rather than continuous attractive lobes. For Ca^{2+}, which lacks a cation-adjacent lone-pair basin, the IGMH maps are radially uniform and essentially free of open-cage structures, showing broad green-to-blue shells that accommodate bulky ligands without a directional penalty. This

IGMH analysis for Ca^{2+} complexes corroborates the conclusion that, binding strength increases with the lowest ESP of the anion (Fig. 1g). More negative ESP of anions corresponds to more negative binding energies.

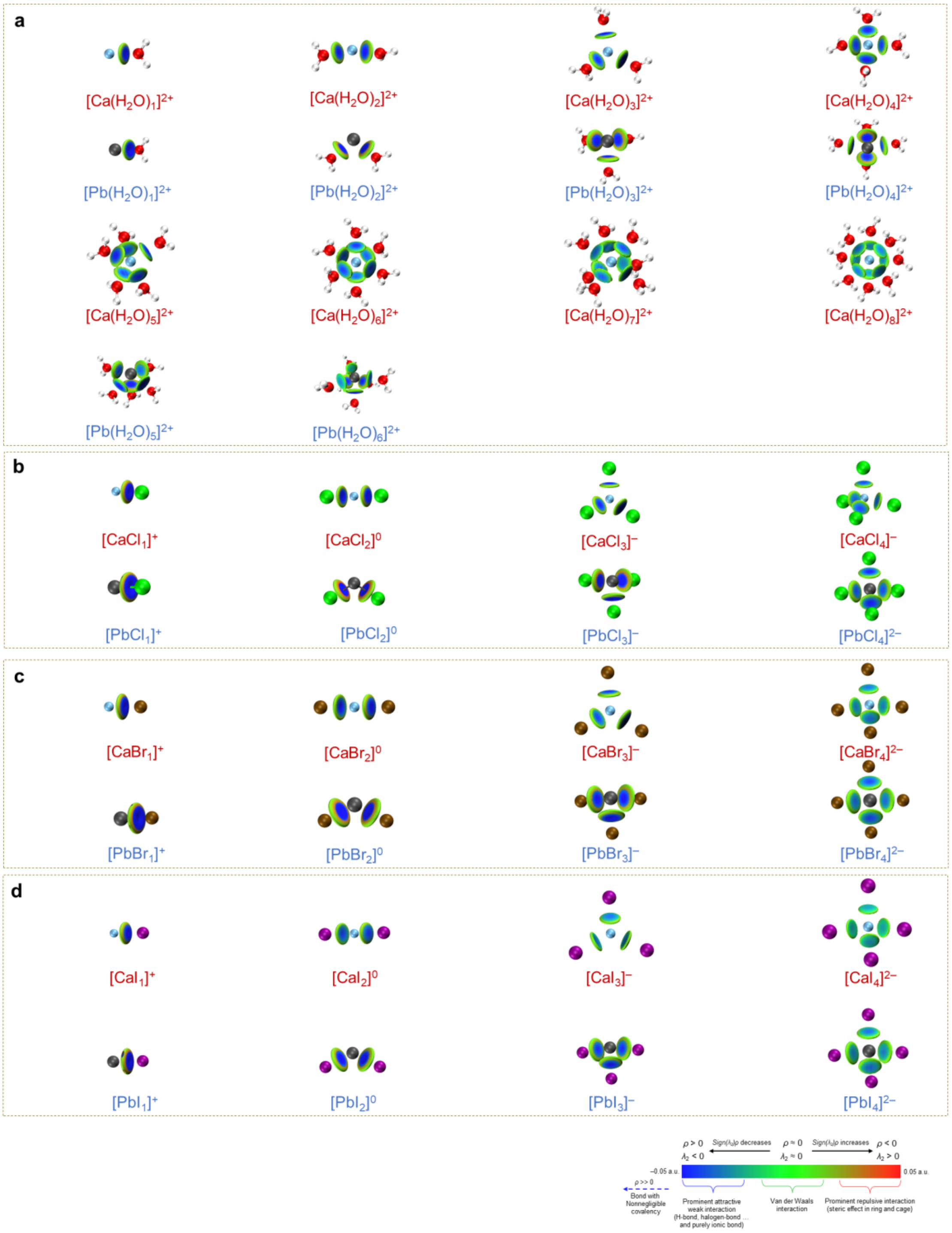

Supplementary Fig. 12 | IGMH analysis of hydrated and halide-coordinate clusters. a–d, *Sign*(λ_2)ρ colored isosurfaces of δg_{inter} = 0.01 a.u. corresponding to IGMH analyses of DFT-optimized Ca^{2+} and Pb^{2+}-centered clusters, showing stepwise coordination with H_2O (a), Cl^- (b), Br^- (c), and I^- (d).

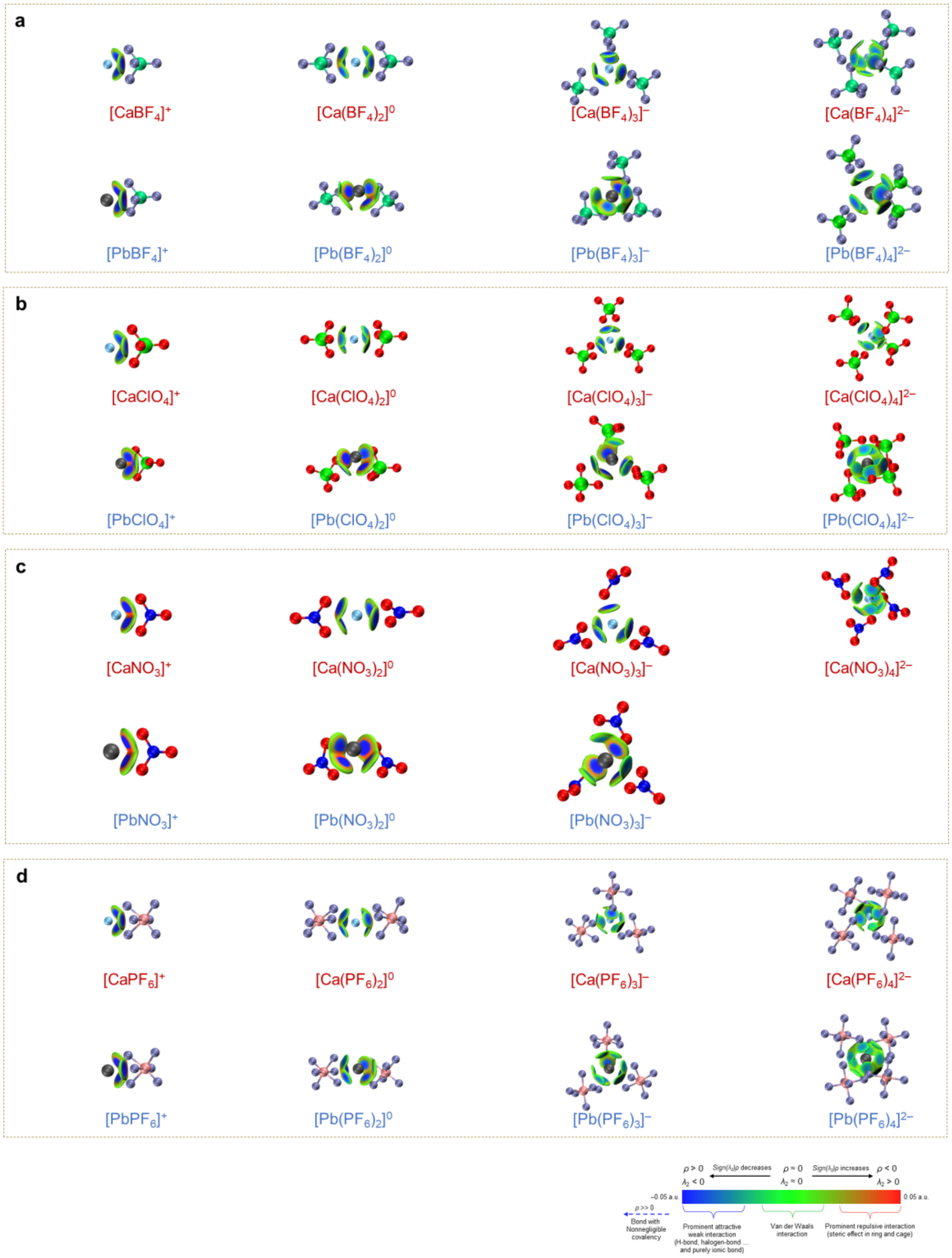

Supplementary Fig. 13 | IGMH analysis of anion-coordinate clusters. a–d, $Sign(\lambda_2)\rho$ colored isosurfaces ($\delta g_{\mathrm{inter}} = 0.01$ a.u.) corresponding to IGMH analyses of DFT-optimized Ca^{2+} and Pb^{2+}-centered clusters, showing stepwise coordination with BF_4^- (a), ClO_4^- (b), NO_3^- (c), and PF_6^- (d).

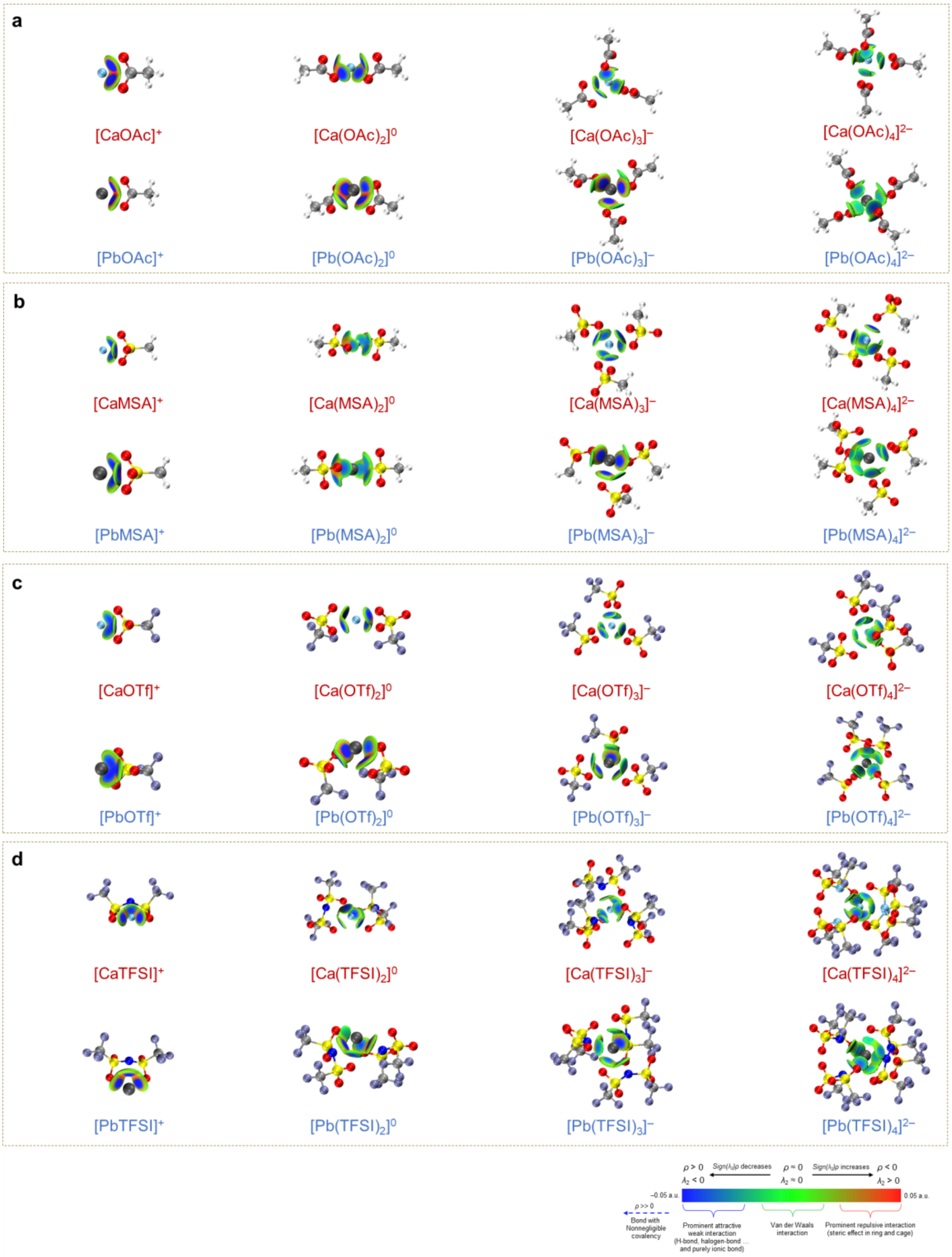

Supplementary Fig. 14 | IGMH analysis of anion-coordinate clusters. a–d, *Sign*(λ_2)ρ colored isosurfaces ($\delta g_{\text{inter}} = 0.01$ a.u.) corresponding to IGMH analyses of DFT-optimized Ca^{2+} and Pb^{2+}-centered clusters, showing stepwise coordination with OAc^- (a), MSA^- (b), OTf^- (c), and $TFSI^-$ (d).

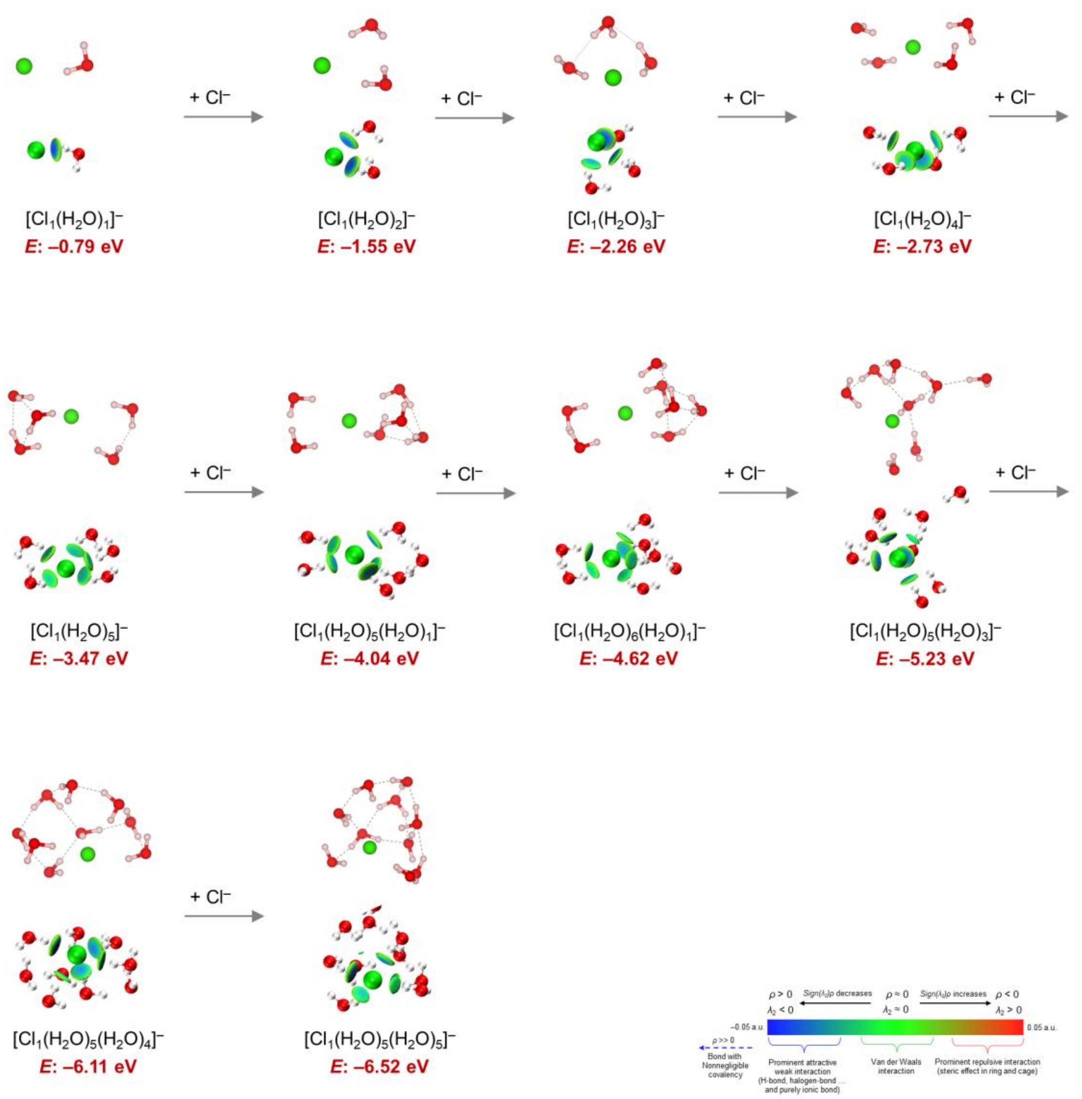

Supplementary Fig. 15 | DFT-optimized structures and IGMH analysis of the stepwise hydration of Cl⁻. *Sign*(λ_2)ρ-colored isosurfaces ($\delta g_{\mathrm{inter}} = 0.01$ a.u.) from IGMH analysis of DFT-optimized structures using Cl⁻ as the coordination center, shown together with the corresponding binding energies (E) for stepwide coordination with H_2O.

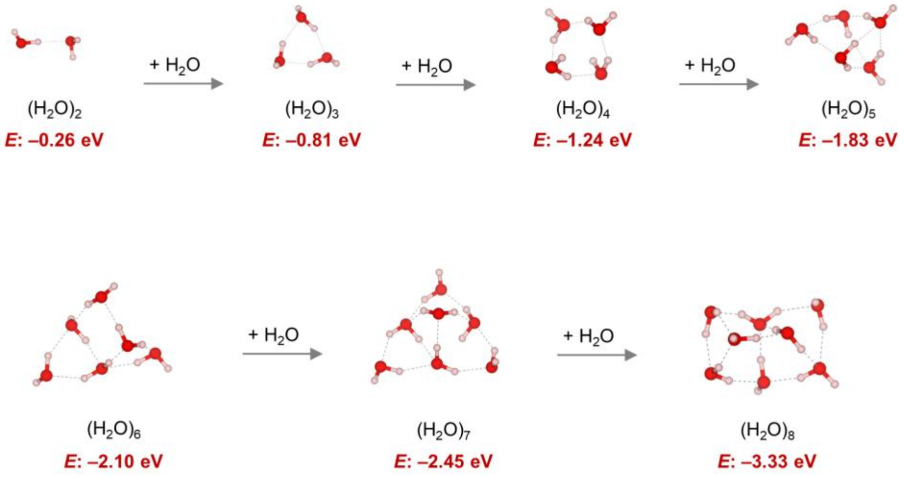

Supplementary Fig. 16 | DFT-optimized H_2O molecular clusters. Representative structures and corresponding binding energies (*E*) for stepwise hydration.

Supplementary Note 1.7. DFT-optimized structures and IGMH analyses for Cl^-–coordinate auxiliary cations (Supplementary Figs. 17, 18)

Subsequently, DFT optimizations across the auxiliary cation–Cl^- series (f Supplementary Figs. 17, 18) yield the expected coordination structures as the number of Cl^- increases from one to four: mono-coordinate (diatomic contact), linear $n = 2$, trigonal-planar $n = 3$, and tetrahedral $n = 4$. Comparison of binding energies at matched n shows a clear hierarchy. Except for monovalent cations, all auxiliary cations form chlorocomplexes that are more stabilized than the corresponding Ca^{2+}–Cl^- complexes (more negative binding energies). Moreover, their binding energies are also more negative than $[PbCl_n]^{n-2}$ coordination at the same n, indicating that they would theoretically outcompete Pb^{2+} for Cl^- coordination if used as the auxiliary cation. The IGMH analysis ($\delta g_{\mathrm{inter}}$ fixed at 0.01 a.u., colored by $sign(\lambda_2)\rho$) resolve cation–Cl^- contacts individually. Excluding monovalent ions, strongly coordinating auxiliaries (Be^{2+}, Mg^{2+}, Al^{3+} and TM ions) show compact $\delta g_{\mathrm{inter}}$ lobes at each contact with deep-blue coloring, evidencing stronger, directional cation-Cl^- attraction (Supplementary Figs. 17, 18). In contrast, Ca^{2+} presents radially uniform, broadened green-to-blue shells with only faint blue at the contact patches, consistent with weakly directional, largely ionic Ca-Cl interactions (top row of Supplementary Fig. 12b). This IGMH fingerprint matches the binding-energy ranking and supports Ca^{2+} as the auxiliary cation: it remains strongly hydrated yet chlorocomplexes only weakly, thereby avoiding Cl^- sequestration and preserving Cl^- coordination for Pb^{2+}/other higher-ESP HPE cations.

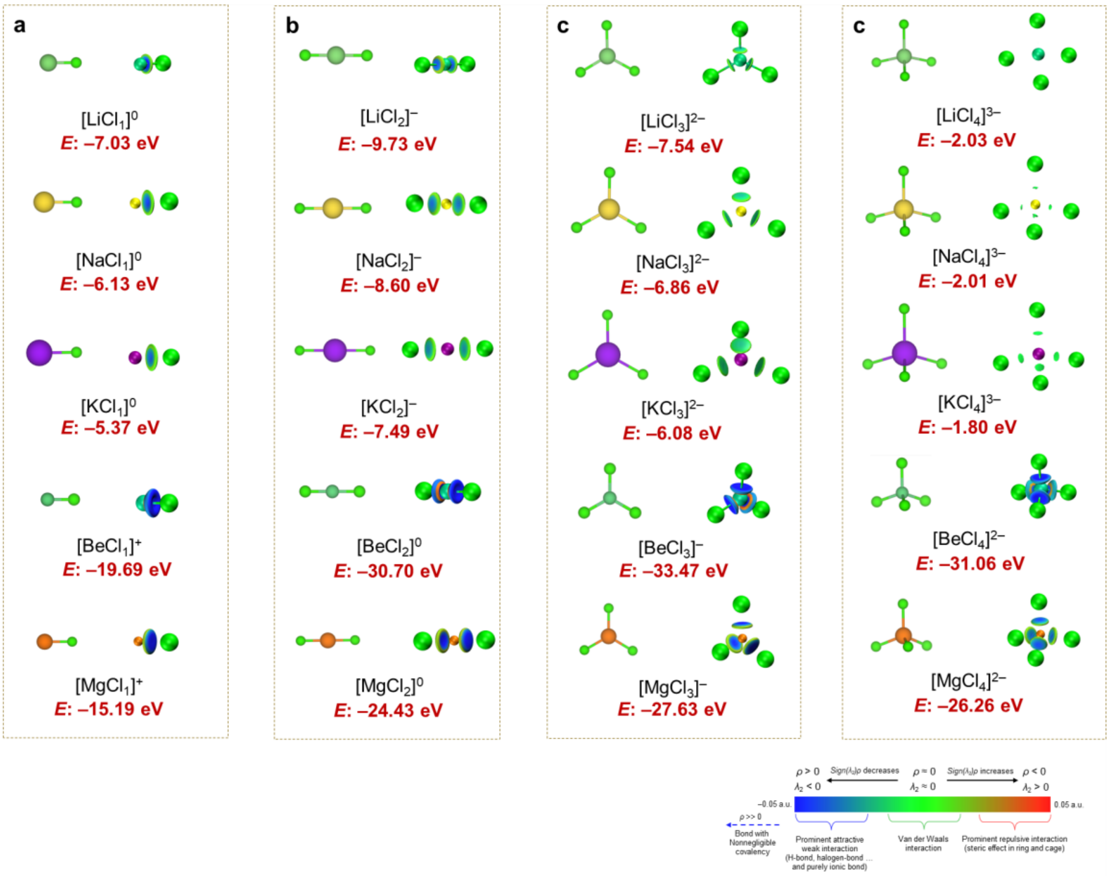

Supplementary Fig. 17 | DFT-optimized structures and IGMH analyses of stepwise Cl$^–$ coordination to cations. a–d, Optimized geometries with binding energies (*E*) and IGMH isosurfaces ($\delta g_{\mathrm{inter}} = 0.01$ a.u.) colored by $sign(\lambda_2)\rho$ for clusters centered on Li$^+$, Na$^+$, K$^+$, Be^{2+}, and Mg^{2+}, illustrating sequential coordination of one (a), two (b), three (c), and four (d) Cl$^–$ ligands.

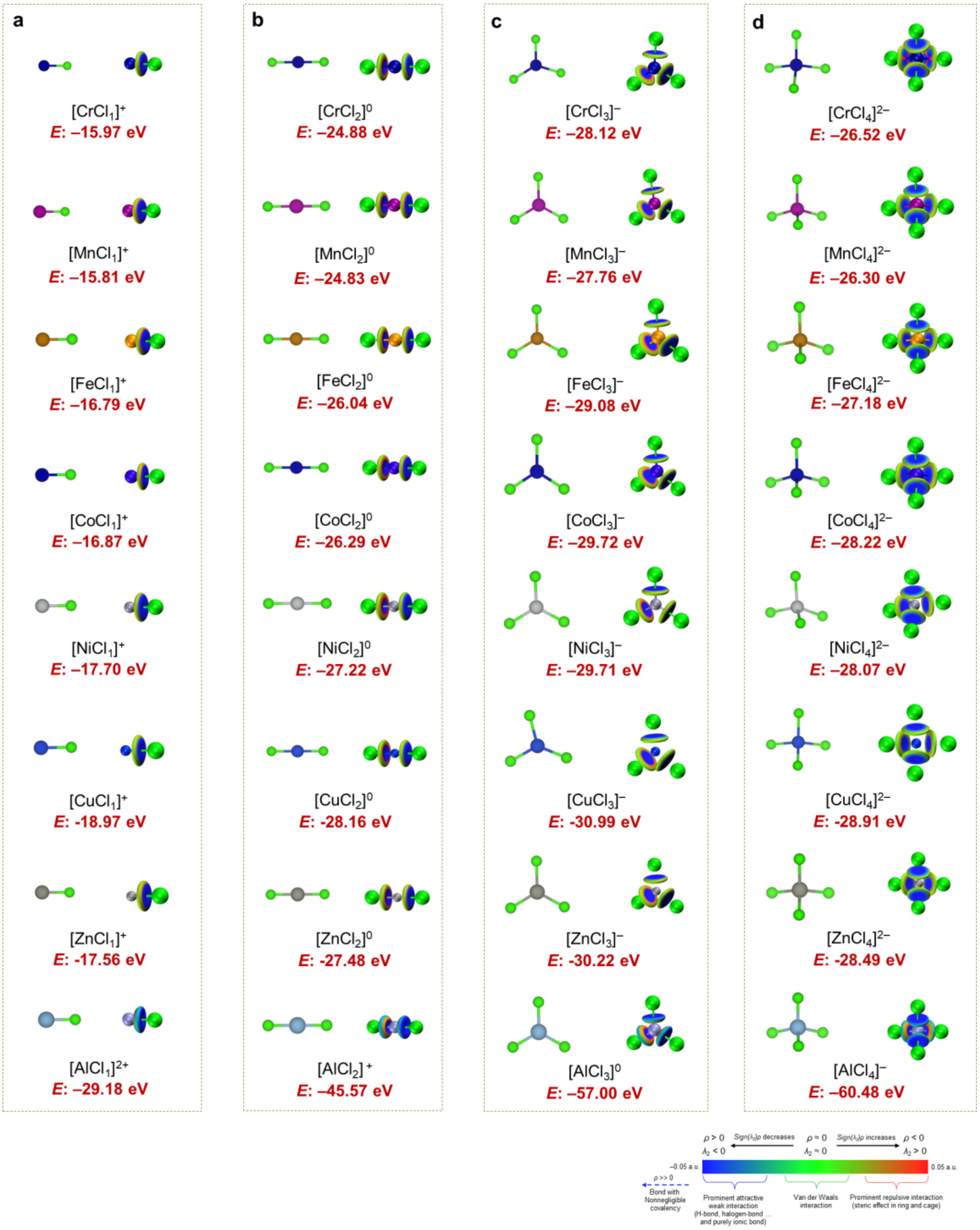

Supplementary Fig. 18 | DFT-optimized structures and IGMH analysis of stepwise Cl$^-$ coordination to cations. a–d, Optimized geometries with binding energies (*E*) and IGMH isosurfaces ($\delta g_{\mathrm{inter}} = 0.01$ a.u.) colored by $sign(\lambda_2)\rho$ for clusters centered on Cr^{2+}, Mn^{2+}, Fe^{2+}, Co^{2+}, Ni^{2+}, Cu^{2+}, Zn^{2+}, and Al^{3+}, illustrating sequential coordination of one (a), two (b), three (c), and four (d) Cl$^-$ ligands.

Supplementary Note 1.8. DFT-optimized structure, ELF, and IGMH analyses for Cl^-- and H_2O-coordinate HPE cations (Supplementary Figs. 19–23)

To further elucidate the intrinsic coordination preferences of the remaining HPE cations, we systematically analyzed the stepwise coordination of Cl^- and H_2O to Sn^{2+}, Sb^{3+}, Bi^{4+}, Se^{4+}, and Te^{4+} based on DFT-optimized structures, complemented by binding energy calculations, ELF maps, and IGMH analyses (Supplementary Figs. 19–23). The optimized structures and corresponding binding energies reveal a clear hierarchy in Cl^- vs. H_2O coordination. All examined HPE cations exhibit substantially stronger binding strengths to Cl^- than to H_2O, as reflected by more negative binding energies across all corresponding CNs. This indicates that Cl^- can more effectively outcompete H_2O molecules to occupy the primary coordination sphere, thereby suppressing undesired hydration-induced side reactions. It should be noted that the absolute magnitudes could be large in high-coordination chlorocomplexes and hydrated structures, for example –101.60 eV for $[SeCl_6]^{2-}$ and –90.33 eV for $[TeCl_6]^{2-}$ (Supplementary Figs. 22b, 23b), which warrants a brief methodological clarification. The binding energies reported here are computed using a classical formal-charge picture of ion-ion or ion-molecule interactions and do not explicitly include electronic polarization, charge transfer, or solvent screening. Consequently, absolute values for highly charged species such as Se^{4+} and Te^{4+} may exceed those realized in solution, where dielectric screening and electronic relaxation attenuate the effective interactions. This does not compromise the comparative analysis. Because all ions and ligands, including ion-ion and ion-H_2O cases, were computed with an identical protocol, the relative energy differences are internally consistent and suitable for qualitatively assessing intrinsic coordination preferences and rationalizing the experimental trends.

For Sn^{2+}, up to four Cl^- ligands were considered because higher-coordination geometries become loose and unstable, consistent with its lower charge density and a stereochemically active lone pair (Supplementary Fig. 19b). By contrast, Sb^{3+}, Bi^{3+}, Se^{4+}, and Te^{4+} retain structural stability up to six-coordination Cl^- complexes (Supplementary Figs. 20b, 21b, 22b, 23b). At low coordination ($n < 4$), all HPE–Cl chlorocomplexes adopt asymmetric geometries due to the directional influence of the ns^2 lone pair, which localizes on one side of the cation and drives distorted ligand arrangements. In this regime, the electrostatic field generated by a small CN of Cl^- ligands is insufficient to offset the lone-pair effect. As the CNs of Cl^- ligands increase ($n \geq 4$), particularly for the higher-valent HPE cations, cumulative electrostatic interactions become dominant and suppress the lone-pair-induced distortion, yielding more symmetric coordination stabilized by strong, quasi-isotropic cation–Cl^- interactions. This asymmetric coordination behavior is clearly reflected in the ELF maps (isosurfaces value = 0.5), which reveal pronounced, localized electron density lobes corresponding to the stereochemically active ns^2 lone pairs on the central cations (bottom rows of Supplementary Figs. 19b, 20b, 21b, 22b, 23b). In the case of H_2O coordination, the presence of these lone pairs leads to strongly distorted, asymmetric hydration geometries at low CNs ($n < 6$) for all HPE cations studied (Supplementary Figs. 19a, 20a, 21a, 22a, 23a). The lone pair occupies a well-defined spatial region opposite to the ligands, pushing coordinating H_2O molecules into asymmetric arrangements to minimize electronic repulsion and accommodate the uneven charge distribution. Interestingly, Bi^{3+}, Te^{4+}, and Se^{4+} adopt nearly symmetric octahedral geometries at $n = 6$ (Supplementary Figs. 21a, 22a, 23a), which can be attributed to their higher charge density and stronger, more isotropic electrostatic interactions. At higher hydration numbers, the cumulative ligand-cation electrostatic field becomes sufficiently strong to override the stereochemical influence of the lone pair, effectively "burying" the lone pair within the inner valence region. This leads to a more uniform spatial distribution of electron density and stabilizes a symmetric octahedral coordination geometry. The preferential Cl^- coordination is corroborated by both the binding energy trends and IGMH analyses. The $\delta g^{\mathrm{inter}}$ isosurfaces (0.01 a.u.) colored by $sign(\lambda_2)\rho$ reveal extensive deep-blue attractive regions between HPE cations and Cl^-, indicative of strong, localized electrostatic-ionic interactions (middle rows of Supplementary Figs. 19b, 20b, 21b, 22b, 23b). In comparison, while the binding energies of H_2O-coordinate complexes are generally less negative than those of their Cl^--coordinate counterparts, the corresponding IGMH maps also display pronounced deep-blue interaction regions between HPE cations and the O atoms of H_2O molecules (middle rows of Supplementary Figs. 19a, 20a, 21a, 22a, 23a), reflecting strong electrostatic attraction within the hydration shell. However, in hydrated complexes, the stereochemically active lone pairs introduce significant spatial asymmetry and steric hindrance, impeding the formation of compact, densely packed hydration shells. This stereoelectronic configuration and the strong attractive interaction between HPE cations and H_2O renders the hydrated HPE cations structurally less stable and more susceptible to hydrolysis and related side reactions. In sharp contrast, Cl^- coordination effectively saturates the coordination sphere, mitigating steric mismatches, stabilizing the complexes, and suppressing hydrolysis pathways.

Overall, Sn^{2+}, Sb^{3+}, Bi^{3+}, Se^{4+}, and Te^{4+}, together with previously analyzed Pb^{2+}, exhibit Cl^- binding strengths that not only exceed their respective hydration energies but also surpass those of Ca^{2+}, consistent with their high ESP and polarizability. As a result, in mixed aqueous systems containing HPE cations, Ca^{2+}, and Cl^-, the HPE cations preferentially coordinate with Cl^-, whereas Ca^{2+} remains predominantly hydrated. This selective coordination behavior underpins the dual-salt strategy: Ca^{2+} functions as a strongly hydrated auxiliary cation that suppresses water activity, while Cl^- acts as the auxiliary anion that selectively binds to HPE cations, displacing H_2O to stabilize their coordination environments and mitigate parasitic hydrolysis.

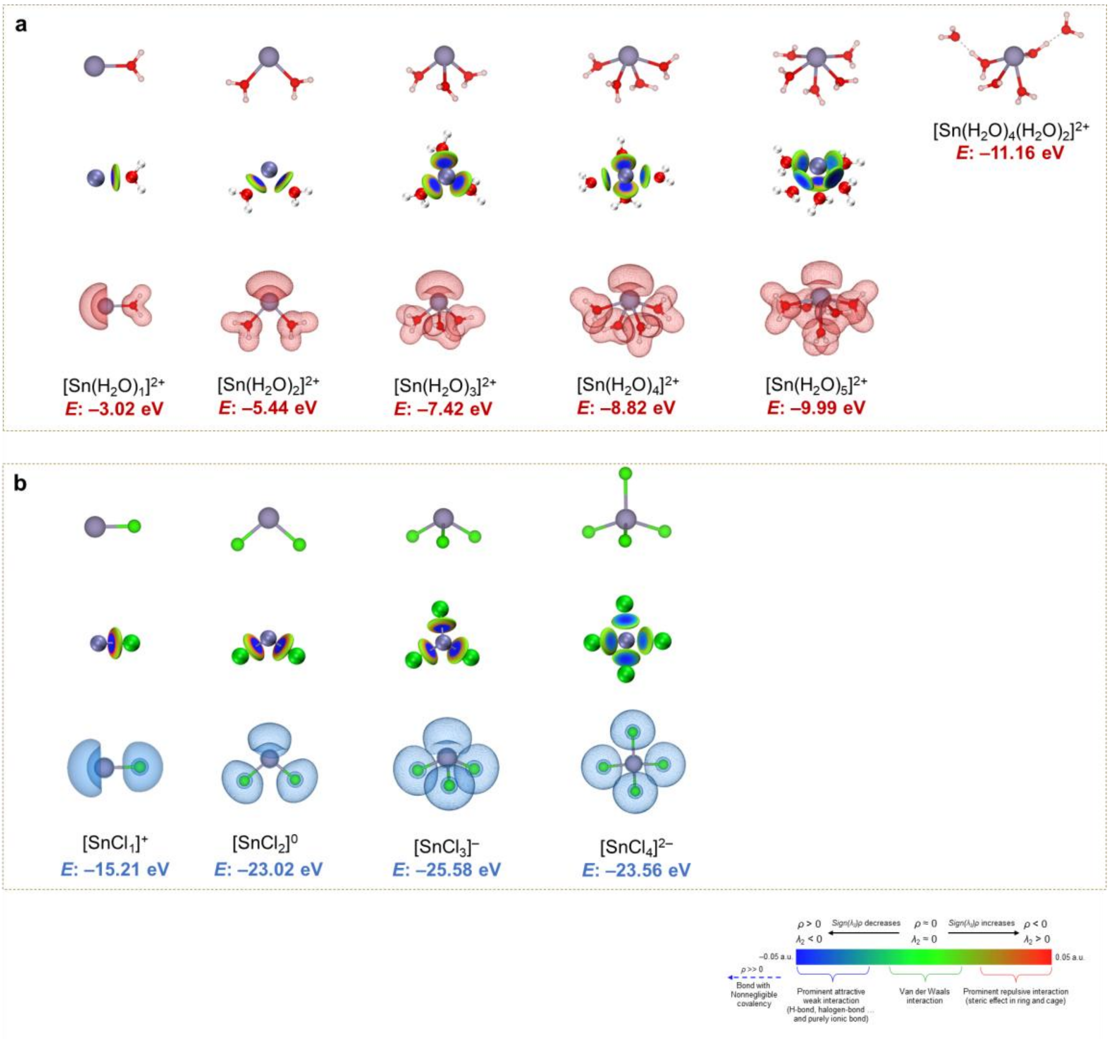

Supplementary Fig. 19 | DFT-optimized structures and electronic structure analyses of H_2O- and Cl^--coordinate Sn^{2+} complexes. **a**, **b**, Optimized structures, IGMH isosurfaces ($\delta g_{\text{inter}} = 0.01$ a.u.) colored by $sign(\lambda_2)\rho$, and ELF isosurfaces (value = 0.5) for Sn^{2+} clusters, illustrating stepwise coordination with H_2O (a) and Cl^- (b) ligands.

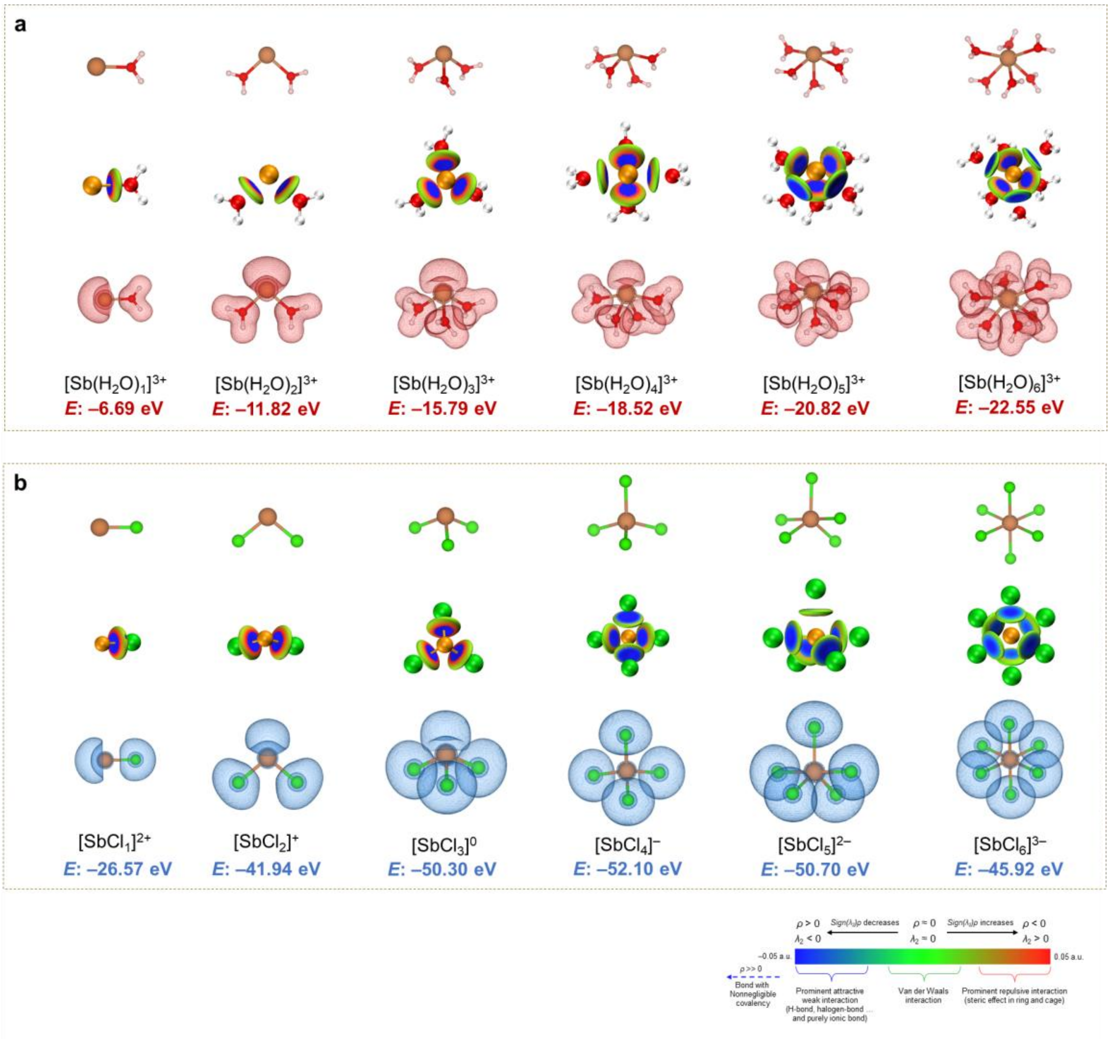

Supplementary Fig. 20 | DFT-optimized structures and electronic structure analyses of H_2O- and Cl^--coordinate Sb^{3+} complexes. **a**, **b**, Optimized structures, IGMH isosurfaces ($\delta g_{\text{inter}} = 0.01$ a.u.) colored by $sign(\lambda_2)\rho$, and ELF isosurfaces (value = 0.5) for Sb^{3+} clusters, illustrating stepwise coordination with H_2O (a) and Cl^- (b) ligands.

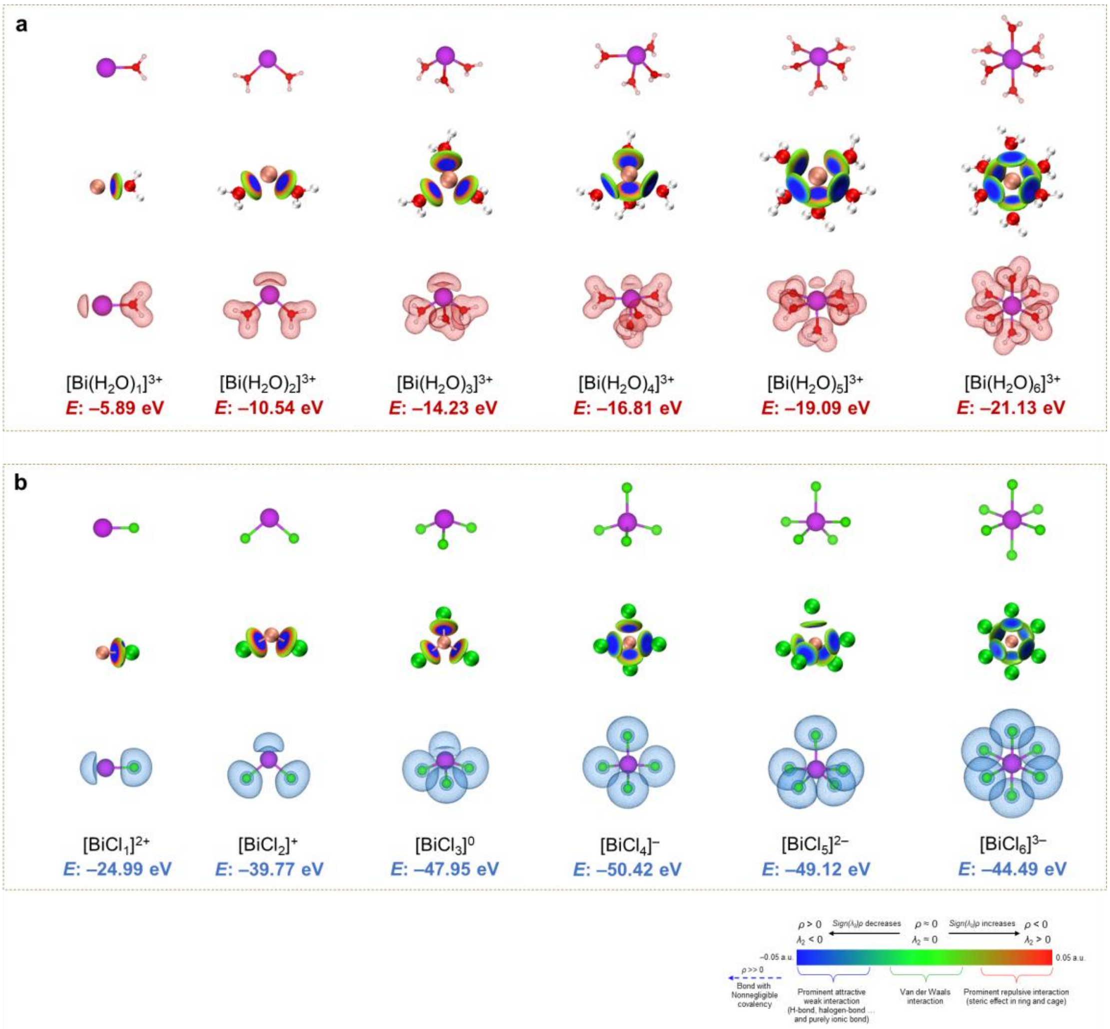

Supplementary Fig. 21 | DFT-optimized structures and electronic structure analyses of H_2O- and Cl^{-}-coordinate Bi^{3+} complexes. **a**, **b**, Optimized structures, IGMH isosurfaces ($\delta g_{\text{inter}} = 0.01$ a.u.) colored by $sign(\lambda_2)\rho$, and ELF isosurfaces (value = 0.5) for Bi^{3+} clusters, illustrating stepwise coordination with H_2O (a) and Cl^{-} (b) ligands.

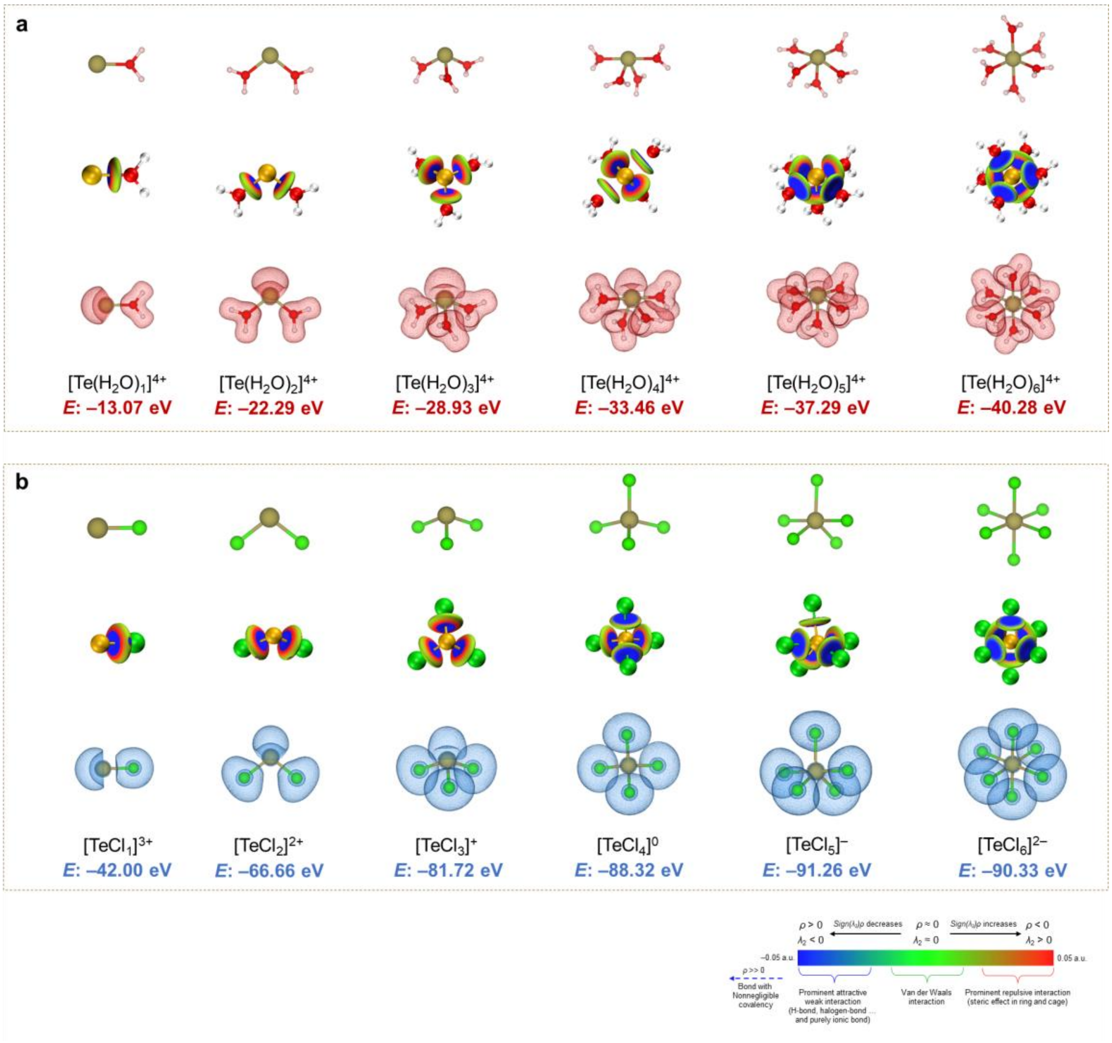

Supplementary Fig. 22 | DFT-optimized structures and electronic structure analyses of H_2O- and Cl^--coordinate Te^{4+} complexes. **a**, **b**, Optimized structures, IGMH isosurfaces ($\delta g_{\mathrm{inter}} = 0.01$ a.u.) colored by $sign(\lambda_2)\rho$, and ELF isosurfaces (value = 0.5) for Te^{4+} clusters, illustrating stepwise coordination with H_2O (a) and Cl^- (b) ligands.

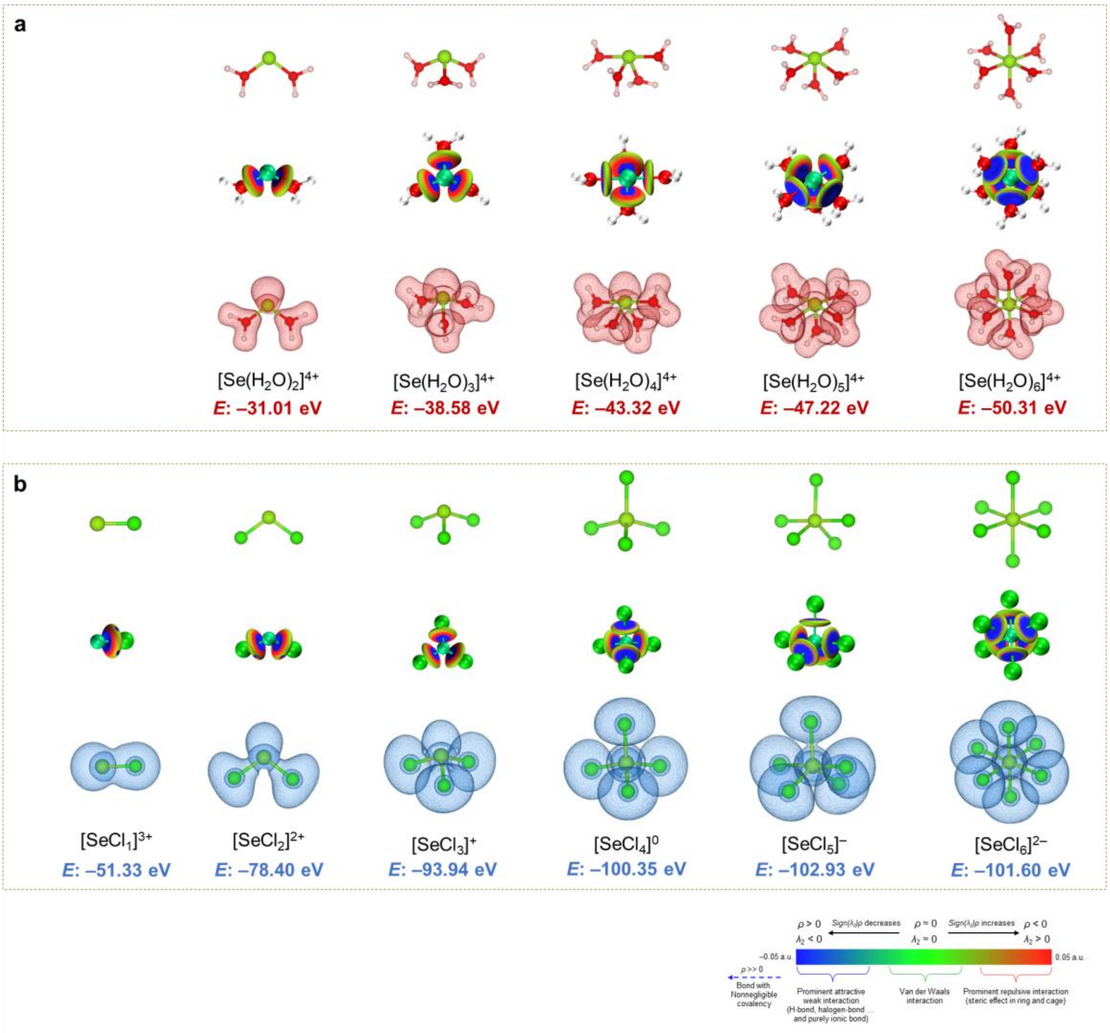

Supplementary Fig. 23 | DFT-optimized structures and electronic structure analyses of H_2O- and Cl^--coordinate Se^{4+} complexes. **a**, **b**, Optimized structures, IGMH isosurfaces ($\delta g_{\mathrm{inter}} = 0.01$ a.u.) colored by $sign(\lambda_2)\rho$, and ELF isosurfaces (value = 0.5) for Se^{4+} clusters, illustrating stepwise coordination with H_2O (a) and Cl^- (b) ligands.

Supplementary Note 2. First-principles exploration of Cl^--containing hydrated structures of auxiliary cations (Supplementary Figs. 24–34)

The AIMD simulations (Supplementary Figs. 2, 3) and subsequent DFT optimizations (Supplementary Fig. 4) have established the feasible hydration structures of the candidate auxiliary cations and identified Ca^{2+} as possessing the largest primary hydration number (up to eight H_2O molecules), and further drawing on the DFT and IGMH analyses in Supplementary Figs. 6b, 17, 18 that revealed Ca^{2+} to exhibit the weakest Cl^- affinity among multivalent cations (apart from the monovalents), we next turned to more realistic aqueous environments. Real aqueous media, however, contain abundant H_2O molecules and coexisting counter-ions, so inner-shell solvation is more diverse and Cl^- could directly enter the primary coordination shell. To bridge from idealized pairs to such realistic conditions, we systematically mapped Cl^--containing hydrated complexes across the full cation set (Li^+, Na^+, K^+, Be^{2+}, Mg^{2+}, Ca^{2+}, Cr^{2+}, Mn^{2+}, Fe^{2+}, Co^{2+}, Ni^{2+}, Cu^{2+}, Zn^{2+}, and Al^{3+}). Corresponding stoichiometries of chlorides were chosen to reflect charge-balanced coordination scenarios and experimentally plausible speciation. Monovalent cations (M^+: Li^+, Na^+, and K^+) were modeled with one Cl^-, i.e., $[MCl(H_2O)_n]^0$ (Supplementary Fig. 24a–c). Divalent cations from Be^{2+} to Zn^{2+} were modeled as mono- and dichloro aquo series, i.e., $[MCl(H_2O)_n]^+$ and $[MCl_2(H_2O)_n]^0$, with optimized cases reported for each cation (Supplementary Figs. 24D, 25–28, 29a). Trivalent Al^{3+} was modeled with one to three Cl^-, i.e., $[AlCl_1(H_2O)_n]^{2+}$, $[AlCl_2(H_2O)_n]^+$ and $[AlCl_3(H_2O)_n]^0$ (Supplementary Fig. 29b). For each stoichiometry, H_2O molecules were added stepwise and DFT geometry optimizations were performed until the highest stable hydration number was reached, further addition producing loose or non-convergent structures. Here, we employ two complementary measures: the total binding energy, which quantifies the overall stabilization upon bringing the cation, Cl^-, and a given number of H_2O molecules together, and IGMH maps, which provide contact-resolved insight. Compact, contiguous deep-blue lobes indicate strong localized attraction, whereas diffuse green-to-light-blue shells indicate weakly directional ionic environments. For each optimized structure, we report the total binding energy and the IGMH isosurfaces at $\delta g_{\text{inter}} = 0.01$ a.u. colored by $sign(\lambda_2)\rho$, viewed with focus on either the cation or Cl^- to resolve individual contacts (Supplementary Figs. 24–34).

For Li^+, Na^+, and K^+ (Supplementary Fig. 24a–c), binding energies of Cl^--containing hydrated complexes are the least negative among the cation series and increase only modestly upon progressive hydration, with diminishing stabilization per added H_2O. The corresponding IGMH maps show shallow, fragmented blue patches at the cation-Cl^- contacts and diffuse hydration shells, indicative of weakly anchored inner-sphere structures. As additional H_2O molecules are introduced, the competition between H_2O and Cl^- for the limited primary coordination sites further weakens individual interactions. Because monovalent cations exhibit relatively weak binding to both Cl^- and H_2O, the incremental hydration leads to expansion and loosening of the inner solvation shell, allowing either the Cl^- or some H_2O molecules to be expelled to the outer shell. This structural relaxation is clearly seen in representative configurations such as $[Li(H_2O)_4Cl]^0$, $[NaCl(H_2O)_3(H_2O)_1]^0$, $[NaCl(H_2O)_3(H_2O)_2]^0$, and $[KCl(H_2O)_5(H_2O)_1]^0$ where increasing hydration drives Cl^- or H_2O away from the inner shell and leads to more delocalized, solvent-separated structures (Supplementary Fig. 24a–c). For Be^{2+} and Mg^{2+} (Supplementary Figs. 24d, 25a), the total binding energies of Cl^--containing hydrated complexes increase sharply compared to the monovalent cations, reflecting the much stronger electrostatic interactions of the divalent centers. The IGMH maps display compact, intense deep-blue lobes at the cation–Cl^- contacts for Be^{2+} and slightly weaker, yet still well-defined, patches for Mg^{2+}. These signatures identify Cl^- as the dominant ligand within the inner coordination shell, establishing the primary structural motif. Stepwise addition of H_2O molecules yields progressively smaller energetic gains, indicating that hydration plays a secondary role that saturates once the Cl^--anchored complex is formed. Unlike the more labile solvation shells of the monovalents, both Be^{2+} and Mg^{2+} maintain tight, localized inner spheres upon hydration, with H_2O molecules arranging around the rigid cation-Cl^- core rather than displacing it. Notably, Be^{2+} accommodates at most four inner-shell ligands, reflecting its small ionic radius and exceptionally high charge density, which favor a compact tetrahedral environment. In contrast, Mg^{2+}, with a larger ionic radius and lower charge density, can sustain up to six coordination, allowing additional H_2O molecules to enter the primary shell without destabilizing the Mg^{2+}-Cl^- interaction. For Ca^{2+} (Supplementary Fig. 25b), the solvation behavior stands out as an intentional outlier among the divalent cations. The IGMH maps display radially uniform hydration shells with only faint, diffuse blue patches at the Ca^{2+}–Cl^- contacts, while extensive hydration dominates the coordination environment. High-coordination structures such as $[CaCl(H_2O)_6]^+$, $[CaCl_2(H_2O)_7]^+$, $[CaCl_2(H_2O)_5]^0$, and $[CaCl_2(H_2O)_6]^0$ exhibit substantial total binding energies, reflecting the strong overall stabilization of Ca^{2+} in water. However, localized interaction analysis reveals that the Ca^{2+}–Cl^- contacts are governed by green regions on the IGMH maps, corresponding to vdW-level interactions, rather than the intense deep-blue lobes characteristic of Be^{2+}-Cl^- or Mg^{2+}–Cl^- bonding. This indicates that hydration, rather than chloride coordination, provides the dominant stabilization in Ca^{2+} solvation structures. Consequently, Ca^{2+} combines a high hydration capacity with intrinsically weak Cl^- affinity, enabling it to depress water activity while leaving Cl^- free to coordinate with HPE cations. This unique balance underpins the rationale for selecting Ca^{2+} as the auxiliary cation in the SICE formulation.

Across the first-row divalent transition metal ions from Cr^{2+} to Zn^{2+} (Supplementary Figs. 26–28, 29a), the incorporation of Cl^- induces pronounced stabilization beyond that provided by hydration alone, as reflected in the substantially more negative binding energies of the resulting complexes. IGMH analysis consistently reveals compact and intense deep-blue domains at the cation–Cl^- contacts, in sharp contrast to the more fragmented and localized blue regions associated with cation–H_2O interactions. These deep-blue lobes persist with increasing hydration, underscoring the dominant role of Cl^- in inner-shell compaction and retention within the primary coordination structures. Zn^{2+} provides a representative example: the neutral $[ZnCl_2(H_2O)_2]^0$ complex is particularly stable, stabilized by strong Zn^{2+}–Cl^- interactions that define a rigid inner coordination core. Upon further hydration, additional H_2O molecules are expelled to the outer solvation shell rather than entering the primary shell, e.g., $[ZnCl_2(H_2O)_2(H_2O)_1]^0$ and $[ZnCl_2(H_2O)_2(H_2O)_2]^0$, underscoring the structural dominance of the chlorocomplex structure (Supplementary Fig. 29a). Similar trends are observed for other TM ions, such as $[MnCl_2(H_2O)_2(H_2O)_2]^0$ (Supplementary Fig. 26b), $[FeCl_2(H_2O)_2(H_2O)_2]^0$ (Supplementary Fig. 27a), and $[CuCl(H_2O)_4(H_2O)_1]^+$/$[CuCl_2(H_2O)_3(H_2O)_1]^0$ (Supplementary Fig. 28b), all of which retain persistent cation–Cl^- cores while accommodating additional H_2O molecules in the outer shell. Notably, this result resembles that of monovalent systems, but the cause is inverted: weak ion-ligand binding in monovalent solutions passively spills H_2O into the second shell (Supplementary Fig. 24a–c), whereas strong TM cation–Cl^- bonding actively excludes it from the inner solvation structure. In addition, this strong chloride binding stands in sharp contrast to the weak, vdW-level Ca^{2+}–Cl^- interactions, emphasizing that first-row TM ions are far less effective at releasing Cl^- in aqueous media. Finally, Cl^--containing hydrated Al^{3+} complexes provide a clear example of a chloride-dominated solvation structure (Supplementary Fig. 29b). At matched hydration numbers, the total binding strengths rank as $[AlCl_3(H_2O)_n]^0 > [AlCl_2(H_2O)_n]^+ > [AlCl_1(H_2O)_n]^{2+}$. IGMH maps display deep-blue Al^{3+}–Cl^- domains that remain pronounced whether one or three Cl^- ligands are present, and increasing the number of H_2O ligands does not appreciably weaken the Al^{3+}–Cl^- interaction. Concomitantly, the IGMH maps also show distinct deep-blue Al^{3+}–O (H_2O) patches across the series, indicating strong hydration interactions; this balance of strong Al-Cl and Al-O contacts underlie the persistence of six-coordination octahedral species, namely, $[AlCl_3(H_2O)_3]^0 > [AlCl_2(H_2O)_4]^+ > [AlCl_1(H_2O)_5]^{2+}$.

Using DFT-optimized structures, binding-energy evaluations, and IGMH analyses performed (Supplementary Figs. 24–29), we systematically enumerated all plausible Cl^--containing hydrated solvation structures spanning CNs from four (e.g., $[BeCl(H_2O)_3]^+$ and $[BeCl_2(H_2O)_2]^0$) to eight (e.g., $[CaCl(H_2O)_7]^+$ and $[CaCl_2(H_2O)_6]$), as summarized in Supplementary Figs. 30–34. For a direct comparison among these solvation structures, our analysis focuses exclusively on the cation–Cl^- interactions within each configuration. These contacts are visualized qualitatively by inter-fragment IGMH isosurfaces at $\delta g_{\text{inter}} = 0.01$ a.u., colored by $sign(\lambda_2)\rho$ (insets of Supplementary Figs. 30–34), while $sign(\lambda_2)\rho$ vs. δg_{inter} scatter plots provide quantitative isolation of the cation–Cl^- contribution, enabling direct comparison of interaction characteristics across distinct solvation environments. Arrows indicate the positions of characteristic peaks corresponding to attractive cation–Cl^- interactions; more negative $sign(\lambda_2)\rho$ values denote stronger attractive interactions. Guided by these descriptors, we sought auxiliary chlorides whose cations are strongly hydrated yet bind Cl^- only weakly, thereby maximizing Cl^- availability while lowering water activity. To that end, we enumerated and optimized the full set of Cl^--bearing solvation motifs, quantified their overall stability through binding energies, and resolved their local cation-Cl^- interactions using IGMH. As shown in Fig. 2a, the binding energy of each structure is plotted against the minimum $sign(\lambda_2)\rho$ value at which δg_{inter} value reaches its attractive maximum, isolating the cation–Cl^- contribution (Supplementary Figs. 30–34). Therefore, more negative *sign*(λ_2)ρ values at the δg_{inter} maximum correspond to stronger cation-Cl^- interactions, allowing us to disentangle bulk hydration stability from localized cation-anion affinity.

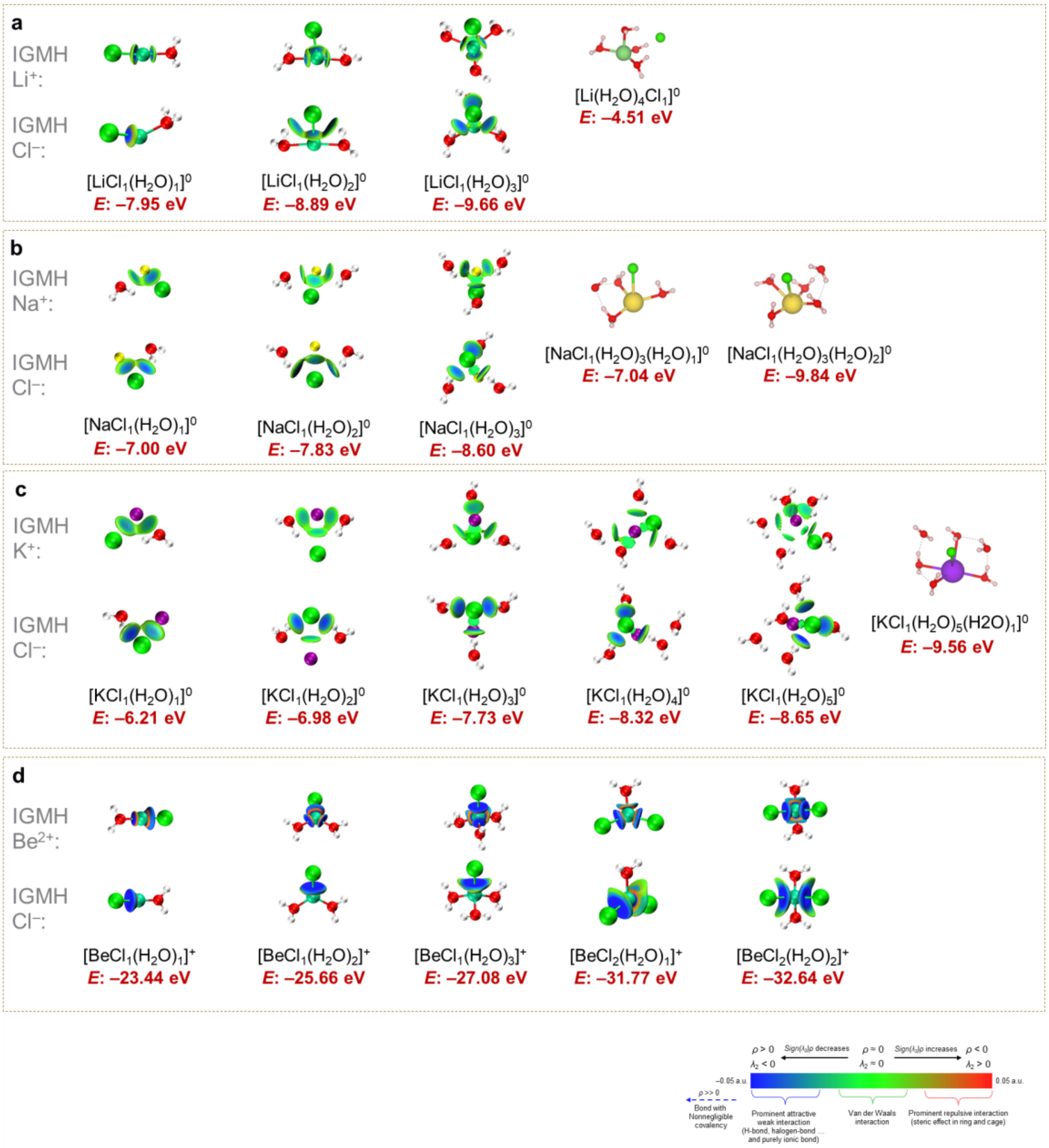

Supplementary Fig. 24 | DFT-optimized structures and IGMH analyses of Cl^--containing hydrated complexes. a–d, Optimized geometries of Li^+ (a), Na^+ (b), K^+ (c), and Be^{2+} (d) solvation complexes with corresponding binding energies (E), together with IGMH isosurfaces ($\delta g_{\text{inter}} = 0.01$ a.u.) colored by *sign*(λ_2)ρ and viewed with focus on either the cation or Cl^-, illustrating stepwise H_2O coordination.

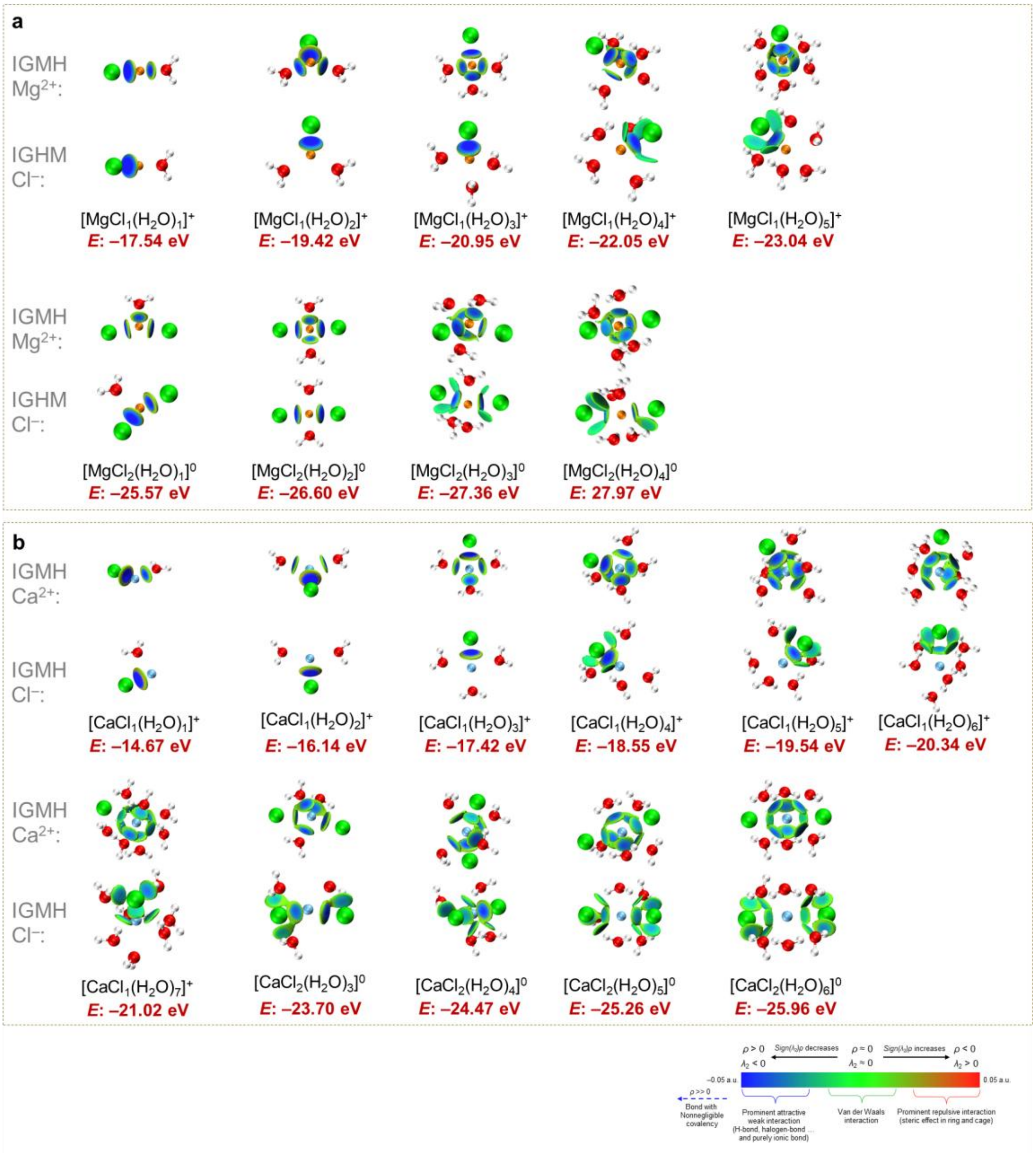

Supplementary Fig. 25 | DFT-optimized structures and IGMH analyses of Cl⁻-containing hydrated complexes. a, **b**, Optimized geometries of Mg^{2+} (a) and Ca^{2+} (b) solvation complexes with corresponding binding energies (E), together with IGMH isosurfaces ($\delta g_{\mathrm{inter}} = 0.01$ a.u.) colored by $sign(\lambda_2)\rho$ and viewed with focus on either the cation or Cl^-, illustrating stepwise H_2O coordination.

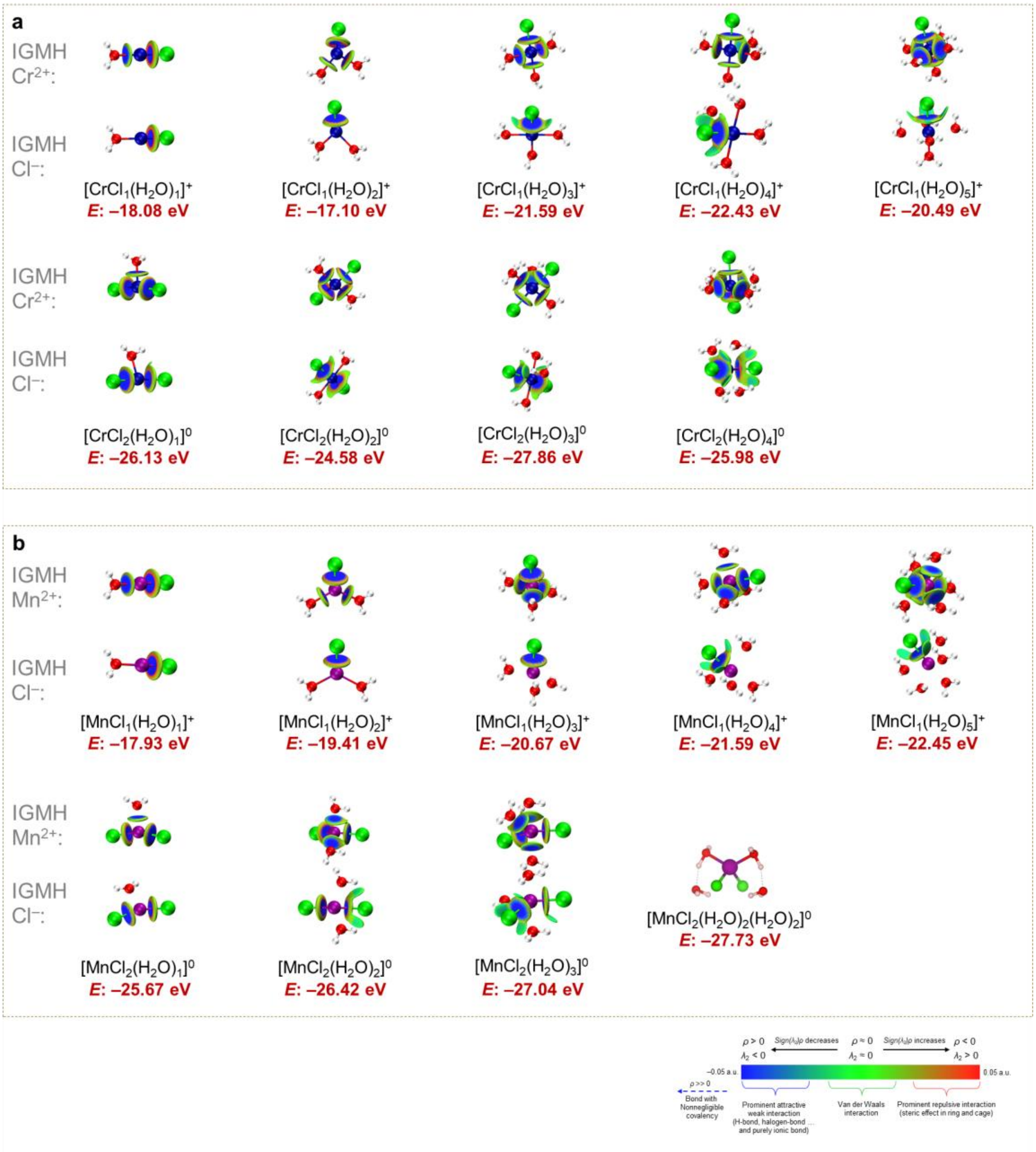

Supplementary Fig. 26 | DFT-optimized structures and IGMH analyses of Cl^{-}-containing hydrated complexes. a, **b**, Optimized geometries of Cr^{2+} (a) and Mn^{2+} (b) solvation complexes with corresponding binding energies (*E*), together with IGMH isosurfaces ($\delta g_{\text{inter}} = 0.01$ a.u.) colored by $sign(\lambda_2)\rho$ and viewed with focus on either the cation or Cl^{-}, illustrating stepwise H_2O coordination.

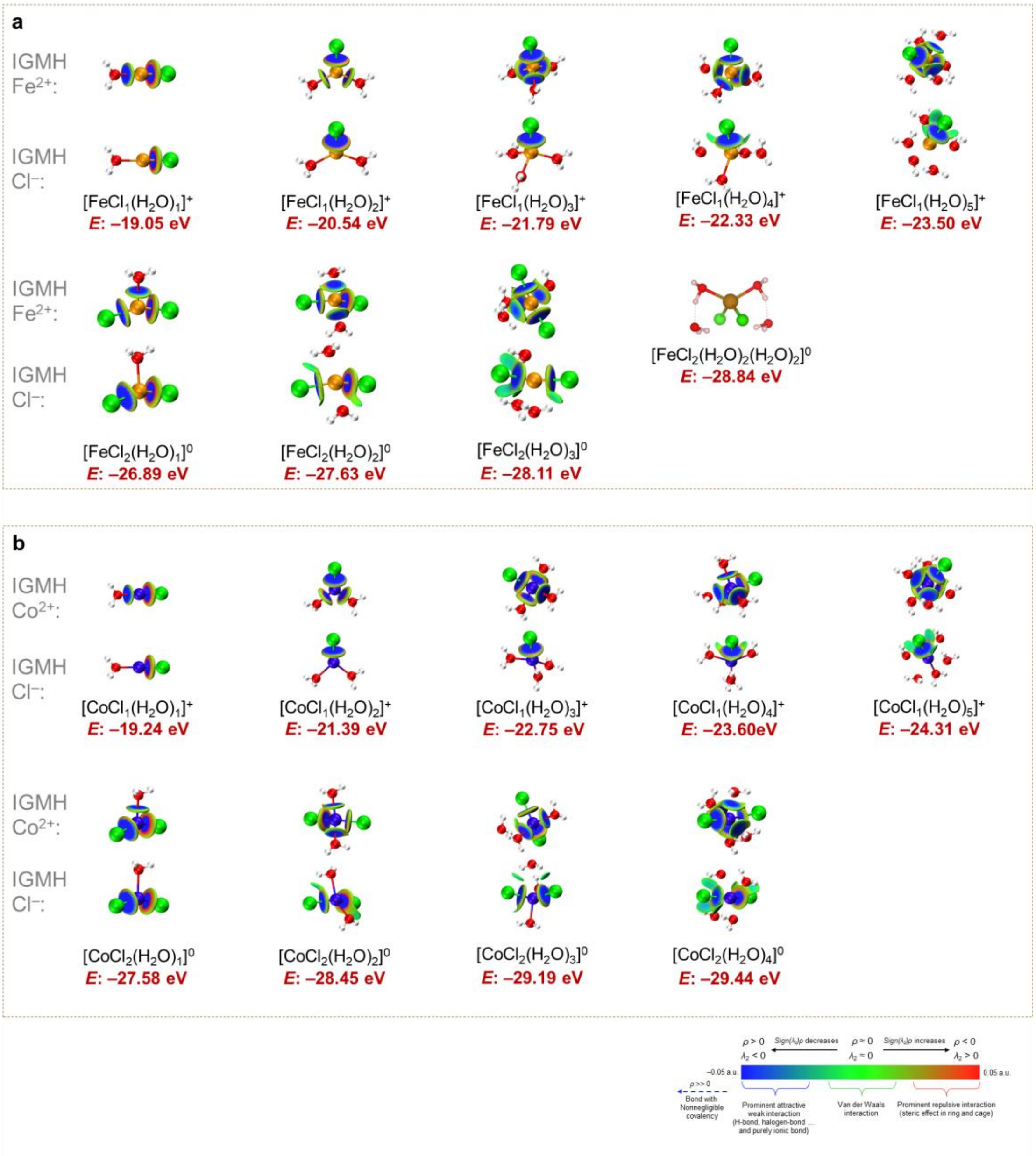

Supplementary Fig. 27 | DFT-optimized structures and IGMH analyses of Cl^--containing hydrated complexes. a, **b**, Optimized geometries of Fe^{2+} (a) and Co^{2+} (b) solvation complexes with corresponding binding energies (E), together with IGMH isosurfaces ($\delta g_{\mathrm{inter}} = 0.01$ a.u.) colored by $sign(\lambda_2)\rho$ and viewed with focus on either the cation or Cl^-, illustrating stepwise H_2O coordination.

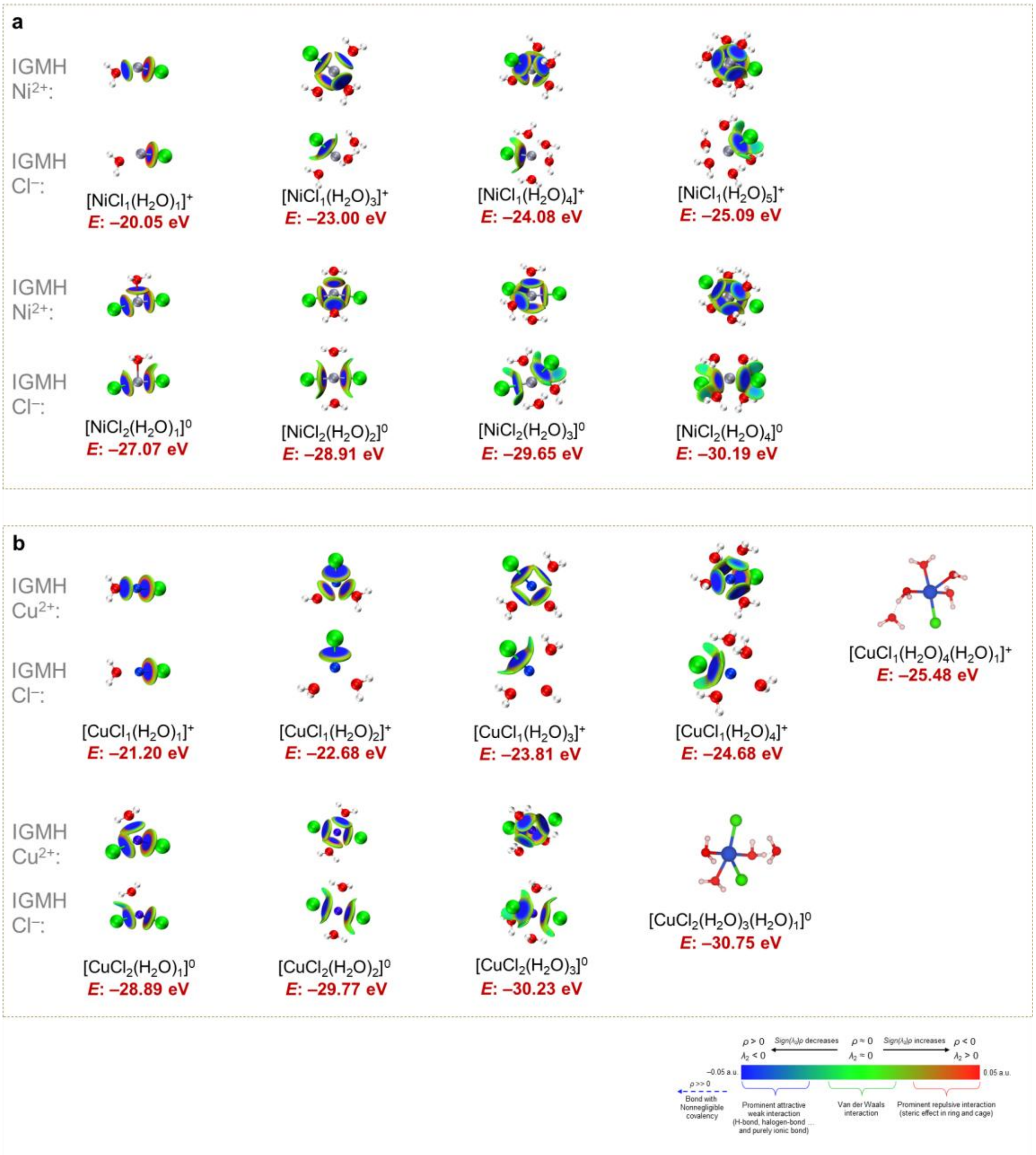

Supplementary Fig. 28 | DFT-optimized structures and IGMH analyses of Cl^--containing hydrated complexes. a, **b**, Optimized geometries of Ni^{2+} (a) and Cu^{2+} (b) solvation complexes with corresponding binding energies (*E*), together with IGMH isosurfaces ($\delta g_{\text{inter}} = 0.01$ a.u.) colored by $sign(\lambda_2)\rho$ and viewed with focus on either the cation or Cl^-, illustrating stepwise H_2O coordination.

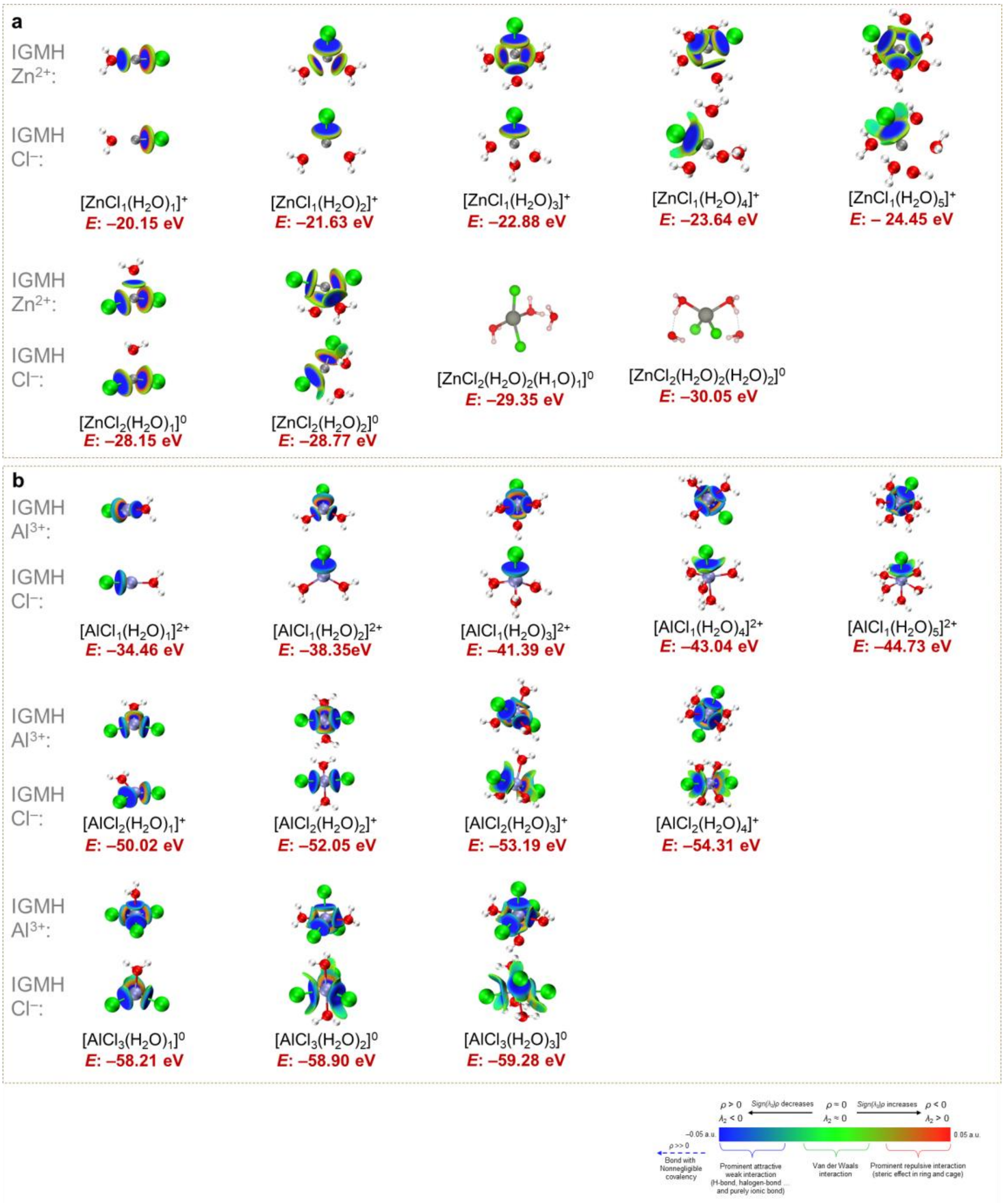

Supplementary Fig. 29 | DFT-optimized structures and IGMH analyses of Cl^--containing hydrated complexes. a, **b**, Optimized geometries of Zn^{2+} (a) and Al^{3+} (b) solvation complexes with corresponding binding energies (E), together with IGMH isosurfaces ($\delta g_{\mathrm{inter}} = 0.01$ a.u.) colored by $sign(\lambda_2)\rho$ and viewed with focus on either the cation or Cl^-, illustrating stepwise H_2O coordination.

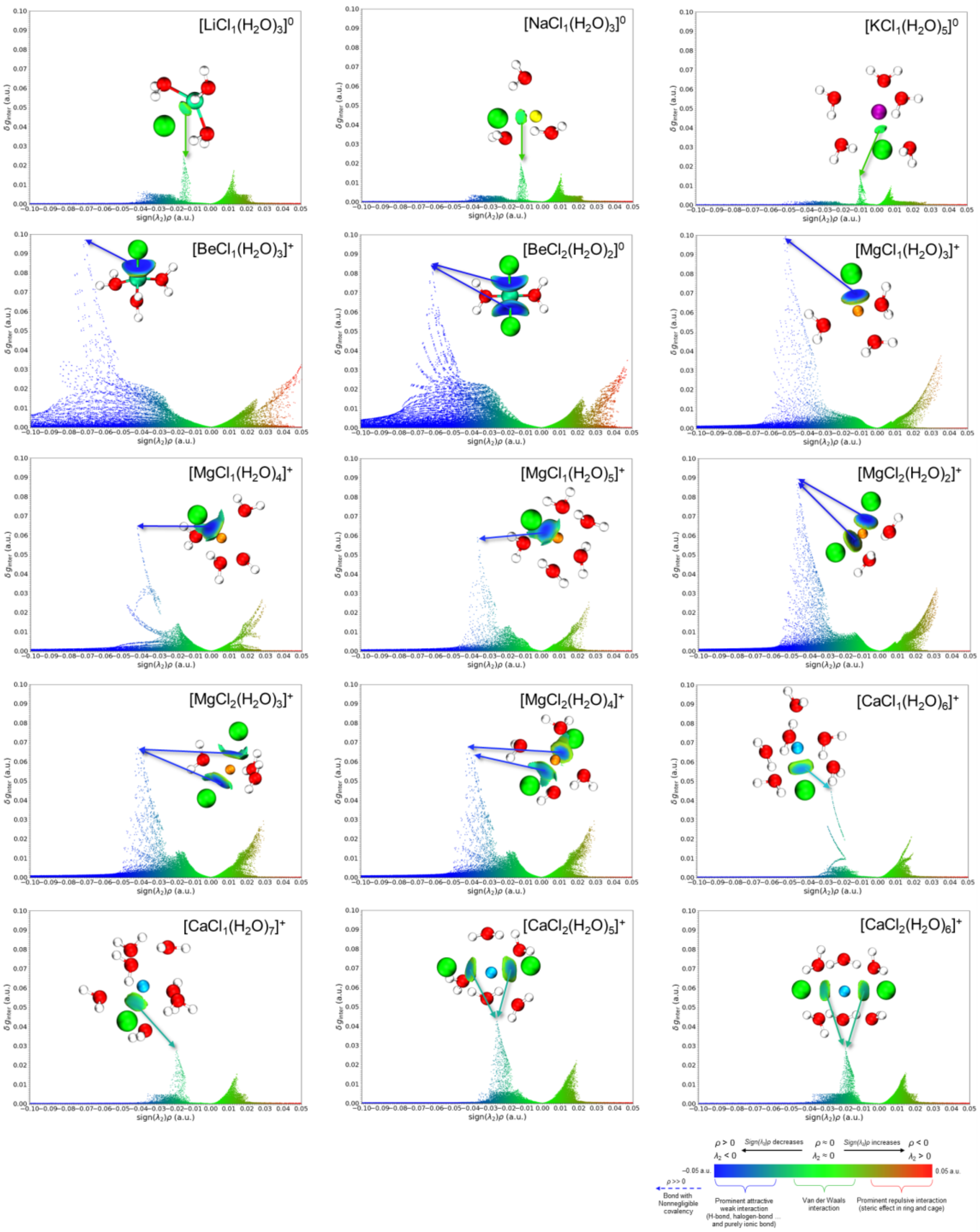

Supplementary Fig. 30 | IGMH analysis focusing exclusively on cation–Cl$^-$ interactions. Scatter plots of $\delta g_{\mathrm{inter}}$ vs. $sign(\lambda_2)\rho$ for cation–Cl$^-$ interactions in possible Cl$^-$-containing solvation structures. Insets: inter-fragment IGMH isosurfaces at $\delta g_{\mathrm{inter}}$ = 0.01 a.u., colored by $sign(\lambda_2)\rho$. This panel highlights the interactions of Li$^+$, Na$^+$, K$^+$, Be^{2+}, Mg^{2+} and Ca^{2+} with Cl$^-$, enabling identification and comparison of interaction nature and strength across different solvation environments.

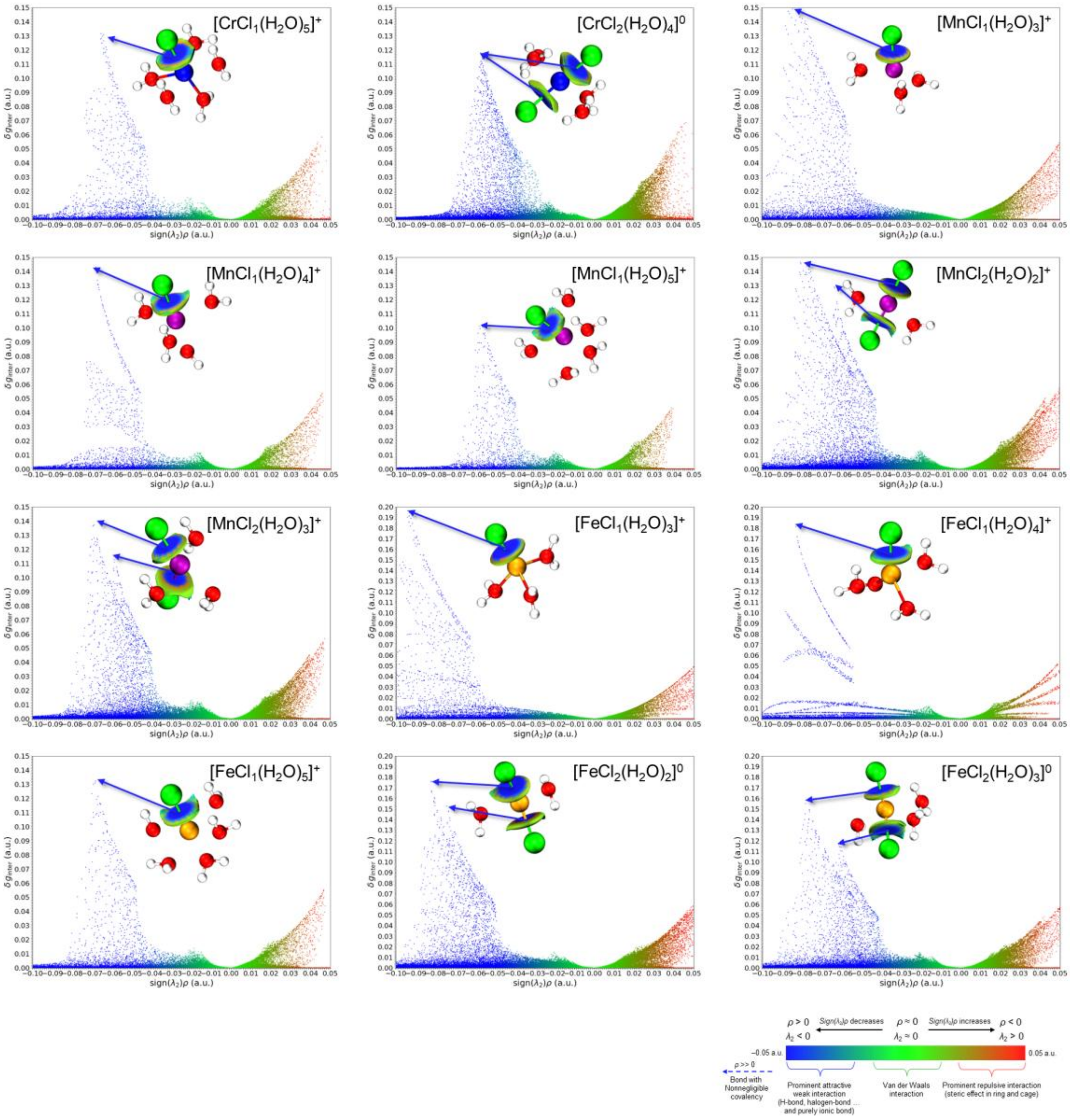

Supplementary Fig. 31 | IGMH analysis focusing exclusively on cation–Cl$^-$ interactions. Scatter plots of $\delta g_{\mathrm{inter}}$ vs. *sign*(λ_2)ρ for cation–Cl$^-$ interactions in possible Cl$^-$-containing solvation structures. Insets: inter-fragment IGMH isosurfaces at $\delta g_{\mathrm{inter}}$ = 0.01 a.u., colored by *sign*(λ_2)ρ. This panel highlights the interactions of Cr^{2+}, Mn^{2+}, and Fe^{2+} with Cl$^-$, enabling identification and comparison of interaction nature and strength across different solvation environments.

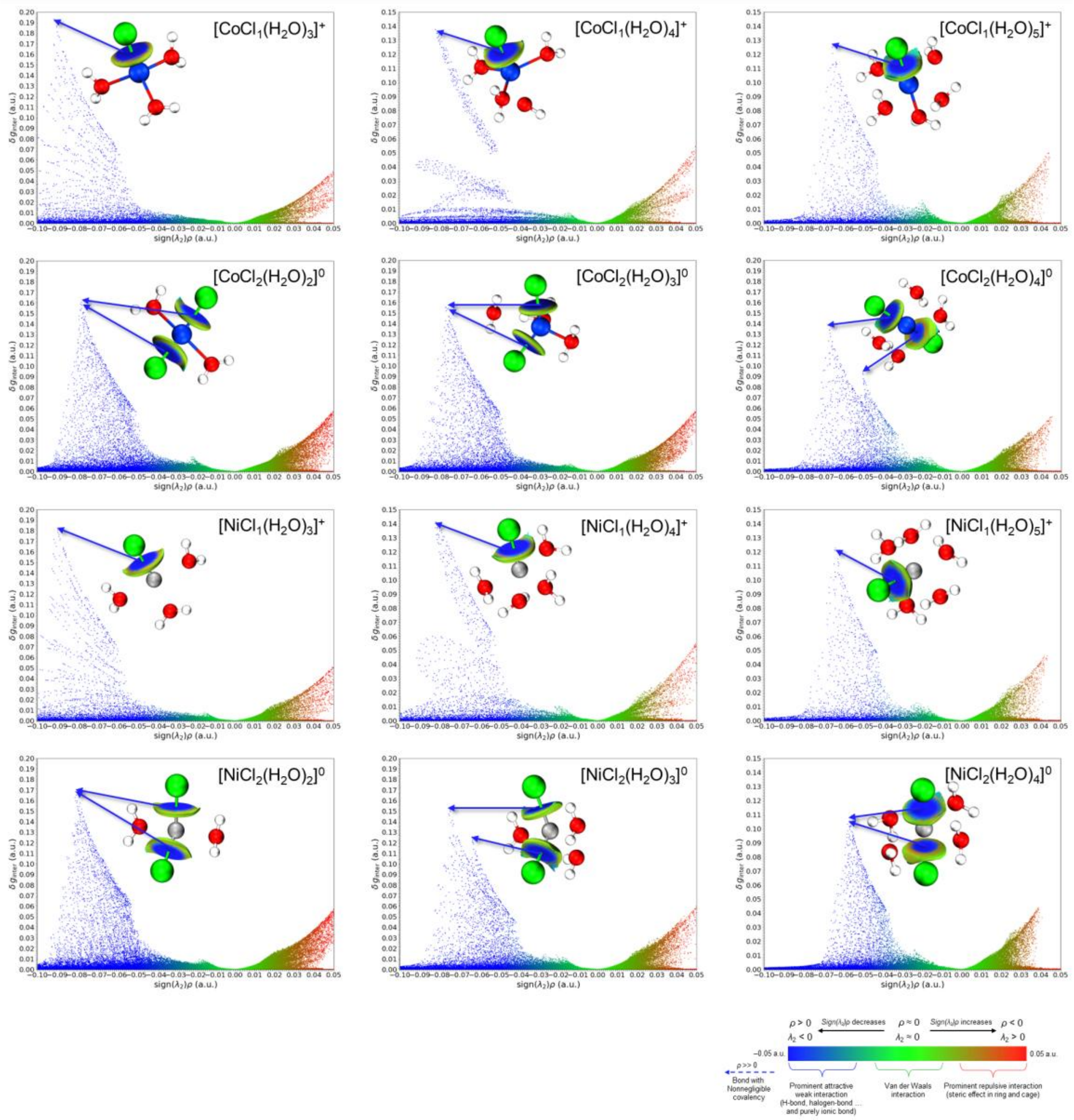

Supplementary Fig. 32 | IGMH analysis focusing exclusively on cation–Cl⁻ interactions. Scatter plots of δg_{inter} vs. $sign(\lambda_2)\rho$ for cation–Cl⁻ interactions in possible Cl⁻-containing solvation structures. Insets: inter-fragment IGMH isosurfaces at δg_{inter} = 0.01 a.u., colored by $sign(\lambda_2)\rho$. This panel highlights the interactions of Co^{2+} and Ni^{2+} with Cl⁻, enabling identification and comparison of interaction nature and strength across different solvation environments.

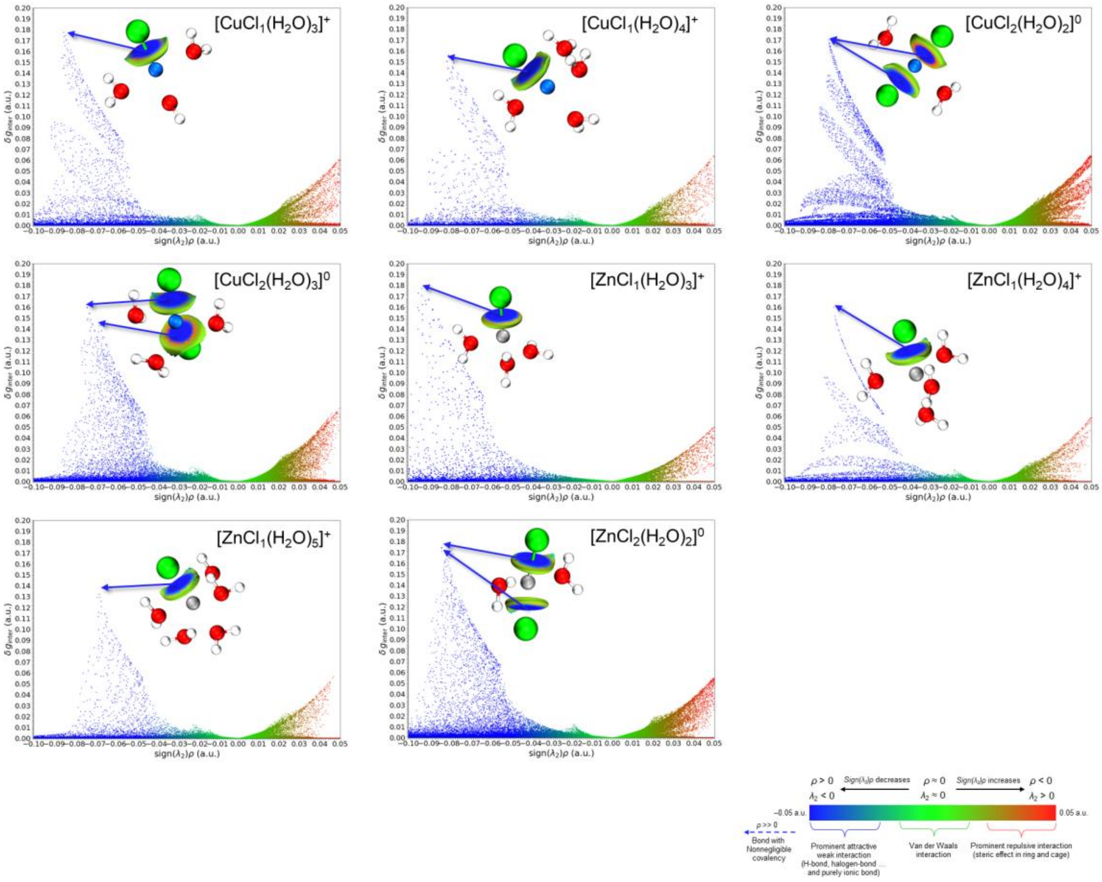

Supplementary Fig. 33 | IGMH analysis focusing exclusively on cation–Cl$^-$ interactions. Scatter plots of δg_{inter} vs. $sign(\lambda_2)\rho$ for cation–Cl$^-$ interactions in possible Cl$^-$-containing solvation structures. Insets: inter-fragment IGMH isosurfaces at δg_{inter} = 0.01 a.u., colored by $sign(\lambda_2)\rho$. This panel highlights the interactions of Cu^{2+} and Zn^{2+} with Cl$^-$, enabling identification and comparison of interaction nature and strength across different solvation environments.

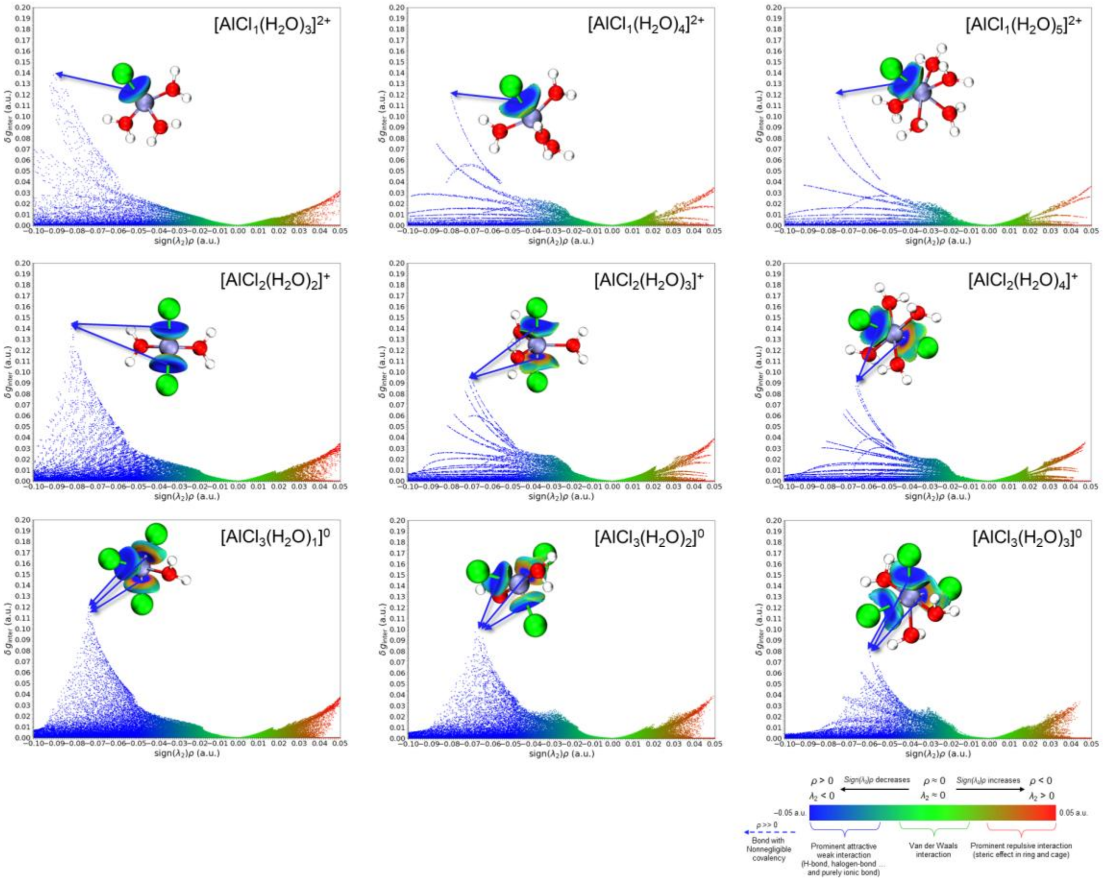

Supplementary Fig. 34 | IGMH analysis focusing exclusively on Al^{3+}–Cl^{-} interactions. Scatter plots of δg_{inter} vs. $sign(\lambda_2)\rho$ for Al^{3+}–Cl^{-} interactions in possible Cl^{-}-containing solvation structures. Insets: inter-fragment IGMH isosurfaces at $\delta g_{\text{inter}} = 0.01$ a.u., colored by $sign(\lambda_2)\rho$.

Supplementary Note 3. Pb L_3-edge X-ray absorption analysis of Pb^{2+} complex structures (Supplementary Fig. 35, and Supplementary Tables 1, 2)

The XANES spectra show a shift toward higher energy at the Pb L_3-edge compared to crystalline PbO (Supplementary Fig. 35a), reflecting a change in the Pb^{2+} chemical environment upon dissolution in the concentrated $CaCl_2$ solution. The EXAFS analysis of PbO reveals a typical Pb–O coordination at 2.31 ± 0.01 Å with four O ligands (Supplementary Fig. 35c, d, and Supplementary Table 1), consistent with the standard PbO crystal structure (Supplementary Fig. 35b). In contrast, the Fouriertransformed EXAFS spectrum of the 6 m $CaCl_2$ + 0.4 m $PbCl_2$ solution exhibits a dominant scattering peak at ~2.4 Å (uncorrected), assigned to Pb–Cl interactions (Fig. 2c and Supplementary Fig. 35e). Quantitative fitting yields a Pb–Cl bond length of 2.75 ± 0.02 Å with a CN of three, confirming the formation of $[PbCl_3]^-$ chlorocomplexes Supplementary Table 1). Notably, no discernible Pb–O contributions are observed, indicating that H_2O molecules are fully excluded from the primary solvation shell of Pb^{2+}. The robustness of the fitting is validated by a low R-factor (0.0196) and physically reasonable Debye–Waller factors. In contrast, alternative fitting models assuming two or four Cl^- ligands (Supplementary Table 2) produce substantially higher R-factors (>0.0210) and inconsistent structural parameters, further corroborating the three-coordination Pb–Cl^- environment. These findings are in full agreement with DFT calculations (Fig. 1c, i), which predict a trigonal pyramidal $[PbCl_3]^-$ structure stabilized by the stereochemically active lone pair on Pb^{2+}.

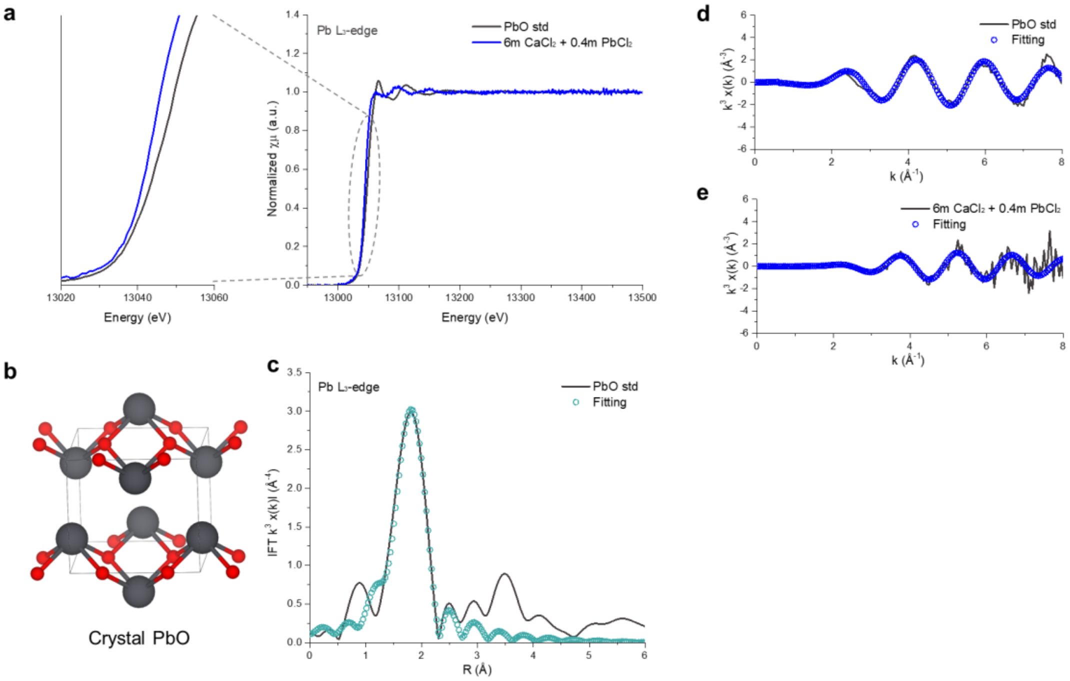

Supplementary Fig. 35 | Analysis of the Pb L_3-edge X-ray absorption spectra and the corresponding EXAFS fitting of 6 m $CaCl_2$ + 0.4 m $PbCl_2$ solutions. a, Normalized Pb L_3-edge XANES spectra and partially enlarged spectra. **b**, Crystal structure of PbO. **c**, The Fourier transform spectrum of the EXAFS (solid line) and fitting (open cycle) for PbO. **d**, **e**, EXAFS spectrum (solid line) and corresponding fitting (open cycle) for PbO (d) and 6 m $CaCl_2$ + 0.4 m $PbCl_2$ solutions (e).

Supplementary Table 1. Summary of the best fitting parameters for Pb structure.

EXAFS spectra	Paths	R (Å)	CN	ΔE_0 (eV)	σ^2 (Å^2)	R factor
PbO std	Pb–O	2.31±0.01	4*	1.5±1.1	0.0082±0.0018	0.0168
6 m CaCl$_2$ + 0.4 m PbCl$_2$	Pb–Cl	2.75±0.02	3*	–5.7±1.2	0.01430±0.0013	0.0196

Supplementary Table 2. The attempted but inappropriate fits (red and bold parameters) for Pb structure.

EXAFS spectra	Paths	R (Å)	CN	ΔE_0 (eV)	σ^2 (Å^2)	R factor
6 m CaCl$_2$ + 0.4 m PbCl$_2$	Pb–Cl	2.75±0.03	2*	–5.8±2.3	0.0077±0.0021	**0.0560**
6 m CaCl$_2$ + 0.4 m PbCl$_2$	Pb–Cl	2.76±0.02	4*	–5.7±1.3	0.0196±0.0014	**0.0210**

Supplementary Note 4. Probing ion-specific solvation in aqueous chloride solutions (Supplementary Figs. 36–38)

Supplementary Note 4.1. Raman spectral analysis of the disrupted hydrogen-bond network (Supplementary Figs. 36, 37)

The Raman spectra and corresponding deconvolution analyses (Supplementary Figs. 36, 37) provide detailed insights into the evolution of hydrogen-bond networks in aqueous solutions of NaCl, KCl, MgCl$_2$, CaCl$_2$, MnCl$_2$, and ZnCl$_2$ across varying concentrations. In pure water (Supplementary Fig. 37a), the hydrogen-bond network is characterized by a broad O–H stretching band of H$_2$O. Five localized hydrogen-bonds for H_2O molecules were identified by proton donor (D) and proton acceptor (A): DAA (~3040 cm^{-1}, strong hydrogen-bond), DDAA (~3220 cm^{-1}, strong hydrogen-bond), DA (~3430 cm^{-1}, medium hydrogen-bond), DDA (~3570 cm^{-1}, weak hydrogen-bond), and free-OH (~3636 cm^{-1}, non- hydrogen-bond), as shown in Supplementary Fig. 37b)[3]. Upon the introduction of chloride salts, a general trend is observed wherein the peak area corresponding to strong hydrogen-bonds (DAA and DDAA) continuously decreases (Supplementary Fig. 37c–h). This shift indicates a gradual disruption of the extensive hydrogen-bond network, leading to more localized and weaker hydrogen-bond interactions with increasing chloride concentrations (Fig. 2d). Furthermore, the Raman spectral deconvolution results of hydrogen-bond network for different aqueous chloride solutions agree well with the theoretical insights obtained from the previous first-principles exploration of Cl^--containing hydrated complexes of auxiliary cations (Fig. 2a, and Supplementary Figs. 2–4, 24–34). Specifically, the extent to which different cations perturb the hydrogen-bond network of among H_2O molecules reflects a balance between their hydration strength, CN, and affinity for Cl^-. For example, monovalent Na^+ and K^+ induce moderate disruption of the hydrogen-bond network, which progressively intensifies with increasing concentration (Supplementary Fig. 37c, d). This behavior arises from their weakly bound hydration shells: while they electrostatically perturb nearby H_2O molecules, their low charge density and relatively labile hydration result in only moderate destabilization of the extended hydrogen-bond network (Supplementary Fig. 4). Moreover, their relatively weak interaction with Cl^- reduces the tendency to form strong ion pairs, allowing them to more readily disrupt hydrogen bonding between H_2O molecules (Supplementary Fig. 24b, c, and Supplementary Fig. 30). As a result, Na^+ and K^+ lead to an overall moderate level of hydrogen-bond network disruption. In contrast, Mg^{2+} induces stronger disruption of the hydrogen-bond network than monovalent cations at low $MgCl_2$ concentrations (<4 m). This behavior arises from its compact, strongly bound hydration shell (Supplementary Fig. 4), where intense electrostatic interactions between Mg^{2+} and first-shell H_2O molecules stabilize the hydration structure. At higher concentrations, the disruption continues to increase but the trend gradually weakens (Supplementary Fig. 37e), as increasing $MgCl_2$ concentration promotes Cl^- participation in the solvation structure of Mg^{2+}. This shift, driven by the inherently strong Mg^{2+}–Cl^- affinity (Supplementary Figs. 25a, 30), mitigates its ability to disrupt the strong hydrogen-bond network. Ca^{2+}, however, produces the most pronounced disruption of strong hydrogen-bond network (Supplementary Fig. 37f). This effect originates from its combination of strong hydration with a high CNs (often 7~8 in water; Supplementary Fig. 4) together with weak Ca–Cl^- association (Supplementary Figs. 25b, 30). Consequently, H_2O rather than Cl^- remains the dominant ligand around Ca^{2+}, pulling a large fraction of H_2O out of the bulk network into primary hydration shells at high $CaCl_2$ concentration. An idealized upper-bound estimate illustrates the magnitude: in 6 m $CaCl_2$ solution, if each of the 6 m of Ca^{2+} coordinates 8 H_2O molecules, about 48 m of H_2O molecules are sequestered in first shells, leaving only about 7.56 m of "free" H_2O molecules out of 55.56 m total. Even under a more conservative hydration number of 7, about 42 m are bound and about 12.6 m remain free, still indicating substantial suppression of bulk water activity.

In comparison, Mn^{2+} shows relatively weak hydrogen-bond disruption (Supplementary Fig. 37g), despite its strong hydration nature (Supplementary Fig. 4). This behavior can be attributed to its pronounced tendency to coordinate with Cl^- (Supplementary Figs. 26b, 31). The formation of Cl^--containing solvation structures reduces the number of bound H_2O molecules and weakens its ability to perturb the hydrogen-bond network (f Supplementary Fig. 37g). Zn^{2+}, with an even stronger tendency to coordinate with Cl^- (Supplementary Figs. 29a, 33), shows the weakest hydrogen-bond disruption even at high $ZnCl_2$ concentrations (Supplementary Fig. 37h). Extensive Cl^- coordination replaces H_2O molecules in the first solvation shell and effectively shields the bulk hydrogen-bond network from direct cation-induced perturbation. Thus, hydrogen-bond deconvolution analyses unequivocally identify Ca^{2+} as producing the greatest reduction in bulk water activity through its highly hydrated solvation structure.

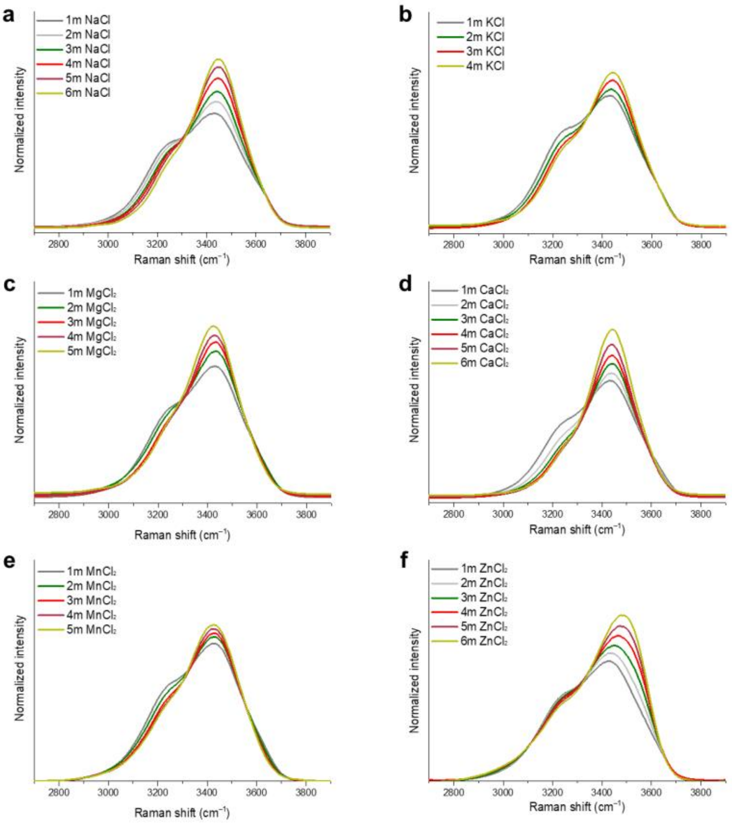

Supplementary Fig. 36 | Raw Raman spectra of aqueous chlorides solutions. a–f, Raman spectra of NaCl (a), KCl (b), $MgCl_2$ (c), $CaCl_2$ (d), $MnCl_2$ (e), and $ZnCl_2$ (f) aqueous solutions recorded at increasing chloride concentrations.

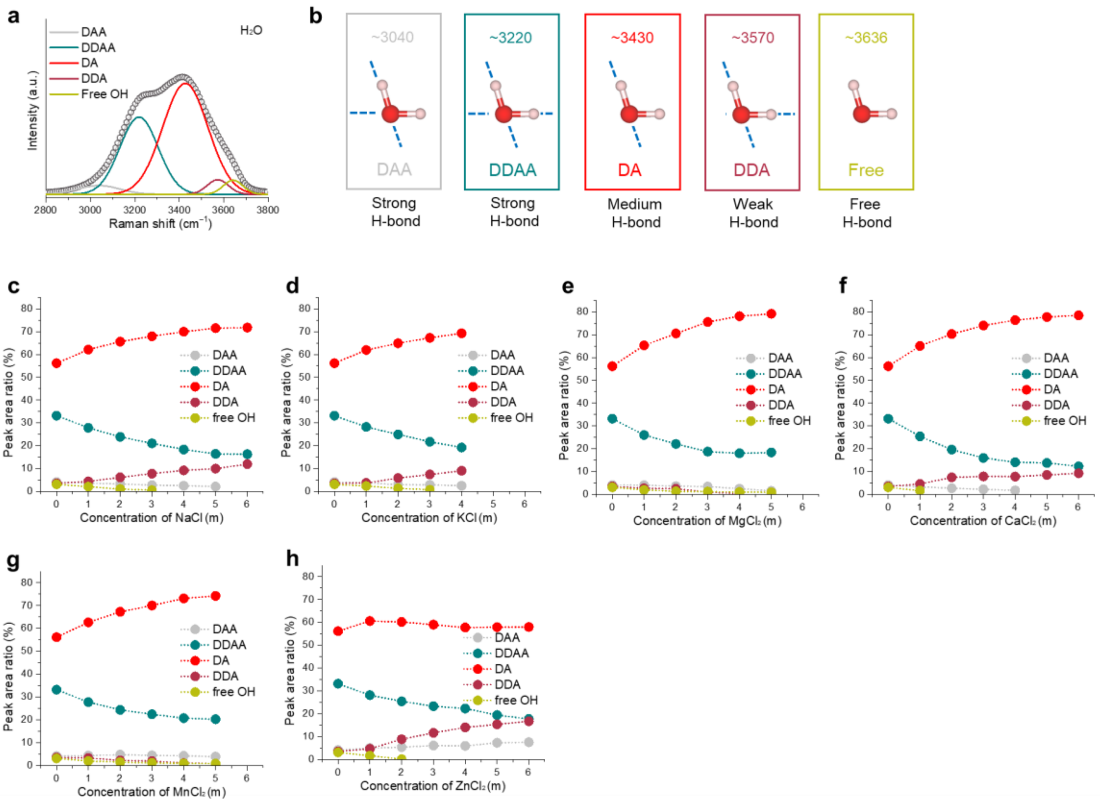

Supplementary Fig. 37 | Disruption of localized hydrogen-bond networks in water by introducing chlorides. a, **b**, Raman spectra of pure water (a) and corresponding H-bond types (b). **c–h**, Peak area ratio of different localized H-bond types in NaCl (c), KCl (d), $MgCl_2$ (e), $CaCl_2$ (f), $MnCl_2$ (g), and $ZnCl_2$ (h) solutions with increasing chloride concentrations.

Supplementary Note 4.2. ^{17}O NMR spectroscopic analysis of hydrated cation–water interactions (Supplementary Fig. 38)

We further employed ^{17}O NMR spectroscopy to quantitatively probe cation–H_2O interactions and the corresponding hydration strength in chloride solutions (Fig. 2e and Supplementary Fig. 38). Low-field chemical shifts of the ^{17}O resonance indicate reduced electron density on the O atoms of H_2O molecules, arising from stronger cation–H_2O interactions that produce a deshielding effect, and vice versa. Thus, progressive low-field shifts with increasing salt concentration reflect the growing fraction of H_2O molecules involved in cation hydration (Fig. 2e), which enhances the overall deshielding effect across all chloride solutions. Notably, the extent of ^{17}O deshielding varies systematically with cation identity. Ca^{2+} exhibits the strongest deshielding effect (Supplementary Fig. 38d), consistent with its stable high hydration numbers (7–8) that impose significant restrictions on the mobility and reorientation of water molecules within the primary hydration shell (Supplementary Figs. 4, 30). In comparison, Mg^{2+}, despite its stronger individual cation–H_2O binding, shows a more moderate deshielding effect due to its lower CN relative to Ca^{2+} (Supplementary Fig. 38c), exemplified by the six-coordination structure in Supplementary Figs. 4, 30. Zn^{2+} follows closely (Supplementary Fig. 38e), reflecting the coexistence of strong Cl^{-} coordination with non-negligible water binding, through species such as $[ZnCl(H_2O)_5]^{+}$ and $[ZnCl_2(H_2O)_2]$ (Supplementary Figs. 4, 33). In contrast, Na^{+} and K^{+}, with their weakly bound hydration structures (e.g., $[Na(H_2O)_6]^{+}$ and $[K(H_2O)_7]^{+}$; Supplementary Fig. 4), display the smallest deshielding effects (Supplementary Fig. 38a, b), consistent with their weak cation–H_2O interaction strength. In addition, it should be noted that ^{17}O NMR signals for $MnCl_2$ solutions could not be detected, likely due to paramagnetic relaxation effects associated with Mn^{2+}, which broaden and quench the resonance.

In sum, our comprehensive analysis reveals a clear positive correlation between theoretical insights from first-principles-based exploration of solvation structures, Raman signatures of hydrogen-bond network deconstruction, ^{17}O NMR analyses of ion-specific hydration strength, and the macroscopic solubility behavior of $PbCl_2$ in different chloride solutions. TM ions such as Zn^{2+} exhibit the strongest Cl^{-} coordination, which restricts their interaction with H_2O molecules and limits the availability of free Cl^{-} for Pb^{2+} complexation, resulting in the persistent insolubility of $PbCl_2$ in $ZnCl_2$ solutions. Mn^{2+} behaves similarly but with slightly weaker Cl^{-} affinity, leading to marginally enhanced $PbCl_2$ dissolution relative to Zn^{2+}. Mg^{2+} shows weaker Cl^{-} coordination than Mn^{2+} and Zn^{2+}, thereby increasing the amount of free Cl^{-} available for Pb^{2+} complexation and enabling slight $PbCl_2$ dissolution. In contrast, Ca^{2+} combines the strongest hydration with weak Cl^{-} coordination, simultaneously lowering bulk water activity and liberating a larger fraction of Cl^{-} for Pb^{2+} coordination, resulting in the most effective $PbCl_2$ dissolution through the formation of soluble $[PbCl_3]^{-}$ species. NaCl and KCl solutions, despite their weak Cl^{-} coordination, supply only stoichiometric amounts of Cl^{-}, making them less effective than $MgCl_2$ and $CaCl_2$ in promoting $PbCl_2$ dissolution. This consistent trend across theory, spectroscopy, and macroscopic behavior underscores the central role of cation-dependent hydration–chloride coordination interplay in determining Cl^- availability for Pb^{2+} complexation.

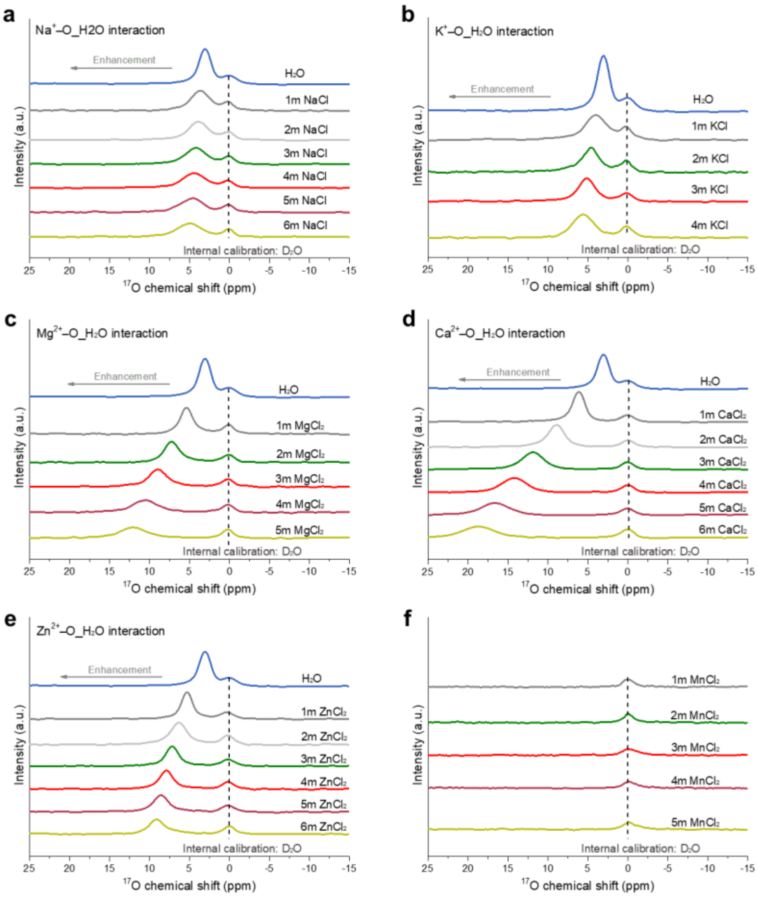

Supplementary Fig. 38 | Evaluation of attractive cation–H_2O interactions in chloride solutions. a–f, ^{17}O NMR spectra of NaCl (a), KCl (b), $MgCl_2$ (c), $CaCl_2$ (d), $ZnCl_2$ (e), and $MnCl_2$ (f) aqueous solutions at increasing chloride concentrations.

Supplementary Note 5. Ca K-edge X-ray absorption analysis of Ca^{2+} solvation structures (Supplementary Fig. 39, and Supplementary Tables 3, 4)

In the XANES spectra (Supplementary Fig. 39a), the Ca K-edge exhibits a progressive shift toward higher energy from the 1 m $CaCl_2$ solution to 6 m $CaCl_2$ and further to the 6 m $CaCl_2$ + 0.4 m $PbCl_2$ solution, approaching that of crystalline $CaCl_2·2H_2O$. This trend reflects a gradual decrease in electron density around Ca^{2+}, likely arising from stepwise dehydration and partial substitution of coordinated H_2O molecules by Cl^- anions, which alters the local electronic environment of Ca^{2+}. EXAFS fitting of $CaCl_2·2H_2O$ reveals a well-defined lattice with distinct Ca–O (2.35 Å) and Ca–Cl (2.74 Å) coordination shells, in excellent agreement with the crystal structure (Supplementary Fig. 39b–d, and Supplementary Table 3). In the dilute 1 m $CaCl_2$ solution (top panel of Fig. 2f, Supplementary Fig. 39e and Supplementary Table 3), Ca^{2+} is primarily surrounded by eight H_2O molecules at an average Ca–O distance of 2.35 ± 0.03 Å, consistent with the DFT-predicted $[Ca(H_2O)_8]^{2+}$ configuration (Supplementary Fig. 3) and confirming its strong hydration and high coordination capability. Upon increasing the concentration to 6 m $CaCl_2$ (middle panel of Fig. 2f, Supplementary Fig. 39f, and Supplementary Table 3), the coordination environment evolves to seven H_2O and one Cl^- ligand, with Ca–O and Ca–Cl distances of 2.37 ± 0.01 Å and 2.68 ± 0.02 Å, respectively. This structural change indicates the formation of a $[CaCl(H_2O)_7]^+$ complex, as visualized in Supplementary Fig. 30, where Ca^{2+}–Cl^- interactions remain weak and weakly directional. Notably, the addition of 0.4 m $PbCl_2$ to the 6 m $CaCl_2$ solution does not affect the local environment of Ca^{2+} (bottom panel of Fig. 2f, Supplementary Fig. 39g, and Supplementary Table 3), which retains the $[CaCl(H_2O)_7]^+$ coordination structure. The fitting reliability is supported by the low R-factors (<0.02) obtained for all best-fit models (Supplementary Table 3). By contrast, alternative fits assuming undercoordinated or overcoordinated Ca–O paths (Supplementary Table 4) yield significantly higher R-factors (>0.021) and unphysical Debye–Waller factors, reinforcing the robustness of the identified solvation structures. Overall, the EXAFS results demonstrate that Ca^{2+} maintains a high CN across concentration ranges, with only minor Cl^- participation and minimal structural perturbation upon Pb^{2+} incorporation.

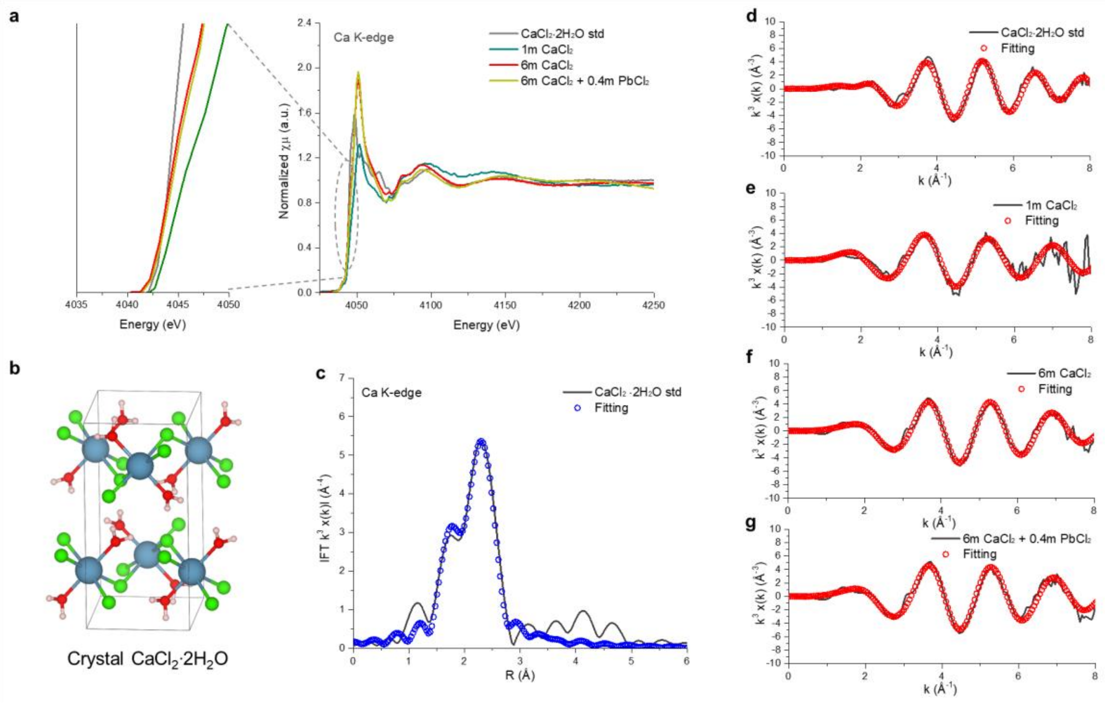

Supplementary Fig. 39 | Analysis of the Ca K-edge X-ray absorption spectra and the corresponding EXAFS fitting of different $CaCl_2$ solutions. a, Normalized Ca K-edge XANES spectra and partially enlarged spectra. **b**, Crystal structure of $CaCl_2·2H_2O$. **c**, The Fourier transform spectrum of the EXAFS (solid line) and fitting (open cycle) for $CaCl_2·2H_2O$. **d–g**, EXAFS spectrum (solid line) and corresponding fitting (open cycle) for $CaCl_2·2H_2O$ (d), 1 m $CaCl_2$ (e), 6 m $CaCl_2$ (f), and 6 m $CaCl_2$ + 0.4 m $PbCl_2$ (g) solutions.

Supplementary Table 3. Summary of the best fitting parameters for Ca structure.

EXAFS spectra	Paths	R (Å)	CN	ΔE_0 (eV)	σ^2 (Å^2)	R factor
$CaCl_2 \cdot 2H_2O$ std	Ca–O	2.35±0.03	2*	2±1.2	0.0033±0.0046	0.016
	Ca–Cl	2.74±0.02	4*		0.0070±0.0027	
1 m $CaCl_2$	Ca–O	2.35±0.03	8*	1.2±2.5	0.0012±0.0018	0.020
6 m $CaCl_2$	Ca–O	2.37±0.01	7*	1.3±0.7	0.0099±0.0009	0.009
	Ca–Cl	2.68±0.02	1*		0.0040±0.0025	
6 m $CaCl_2$ + 0.4 m $PbCl_2$	Ca–O	2.37±0.01	7*	1.3±0.9	0.0083±0.0011	0.019
	Ca–Cl	2.69±0.03	1*		0.0044±0.0037	

Supplementary Table 4. The attempted but inappropriate fits (red and bold parameters) for Ca structure.

EXAFS spectra	Paths	R (Å)	CN	ΔE_0 (eV)	σ^2 (Å^2)	R factor
6 m $CaCl_2$ + 0.4 m $PbCl_2$	Ca–O	2.37±0.01	6*	1.3±0.9	0.0054±0.0012	**0.0220**
	Ca–Cl	2.70±0.02	1*		**0.0015±0.0028**	
6 m $CaCl_2$ + 0.4 m $PbCl_2$	Ca–O	2.37±0.02	7*	0.7±1.2	0.0099±0.0015	**0.0210**
	Ca–Cl	2.67±0.03	2*		**0.0127±0.0053**	
6 m $CaCl_2$ + 0.4 m $PbCl_2$	Ca–O	2.38±0.02	8*	1.5±1.2	0.0111±0.0013	**0.0214**
	Ca–Cl	2.67±0.04	1*		0.0075±0.0063	

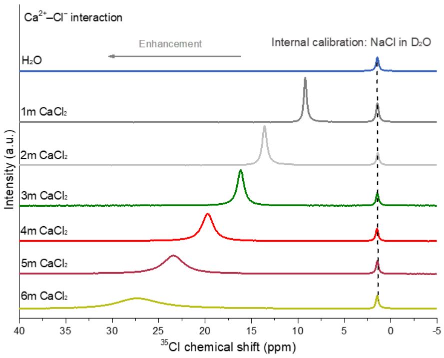

Supplementary Fig. 40 | Evaluation of attractive Ca–Cl⁻ interactions in chloride solutions. ^{35}Cl NMR spectra of $CaCl_2$ aqueous solutions at increasing $CaCl_2$ concentrations

Supplementary Note 6. Evolution of speciation and chlorocomplex stability of Pb–, Sn–, Sb–, Bi–, Te–, and Se–chlorides in $CaCl_2$-based SICEs (Supplementary Figs. 41–49)

Supplementary Note 6.1. From water-insoluble $PbCl_2$ to soluble $[PbCl_3]^-$ (Supplementary Fig. 41)

The intrinsically low solubility of $PbCl_2$ in water originates from its high lattice energy, which is insufficiently compensated by the hydration enthalpies of Pb^{2+} and Cl^-. Consequently, the dissolution of $PbCl_2$ is thermodynamically disfavored under ambient aqueous conditions. To overcome this limitation, we introduced high chloride activities to promote dissolution through Pb–Cl complexation. The stepwise equilibria and stability constants for Pb–Cl species are as follows[4]:

$$Pb^{2+} + Cl^- \leftrightarrow [PbCl]^+ \qquad \log K_1 = 1.10 \tag{1}$$

$$[PbCl]^+ + Cl^- \leftrightarrow PbCl_2 \qquad \log K_2 = 1.16 \tag{2}$$

$$PbCl_2 + Cl^- \leftrightarrow [PbCl_3]^- \qquad \log K_3 = -0.40 \tag{3}$$

$$[PbCl_3]^- + Cl^- \leftrightarrow [PbCl_4]^{2-} \qquad \log K_4 = -1.05 \tag{4}$$

The relatively large K_1 and K_2 values indicate facile formation of $PbCl^+$ and $PbCl_2$, but the high lattice energy of solid $PbCl_2$ fundamentally limits dissolution at low chloride activity. In contrast, elevated Cl^- concentrations can shift the equilibria toward higher-order chloroplumbate species. In 6 m $CaCl_2$ solution, the abundant Cl^- drives the formation of soluble $[PbCl_3]^-$ complexes, enabling $PbCl_2$ dissolution to concentrations up to 0.4 m (Fig. 2b, c), whereas $PbCl_2$ remains largely insoluble in pure water (Supplementary Fig. 41). Further conversion to $[PbCl_4]^{2-}$ is limited by the much lower stability constant K_4, making $[PbCl_3]^-$ the dominant dissolved species under these conditions (Fig. 2c). First-principles calculations provide a molecular-level rationale for this thermodynamic preference. The total Pb–Cl binding energy for $[PbCl_3]^-$ is –

24.53 eV, whereas $[PbCl_4]^{2-}$ is less stable at –23.08 eV (bottom row of Supplementary Fig. 6b). Although the total energy difference is modest (1.45 eV), the average Pb–Cl bond strength is clearly higher in $[PbCl_3]^-$, as discussed in Supplementary Note 1.4. IGMH analysis, based on the negative $sign(\lambda_2)\rho$ value at the peak δg_{inter} maximum, further reveals that the Pb–Cl interactions in $[PbCl_3]^-$ fall within the regime of strong halogen-bond-like contacts, indicative of strong yet largely ionic interactions characteristic of stable chlorocomplexes (bottom panel of Fig. 2g). Taken together, both thermodynamic equilibria and first-principles interaction analyses demonstrate that concentrated $CaCl_2$ media promote $PbCl_2$ dissolution through the stabilization of soluble $[PbCl_3]^-$.

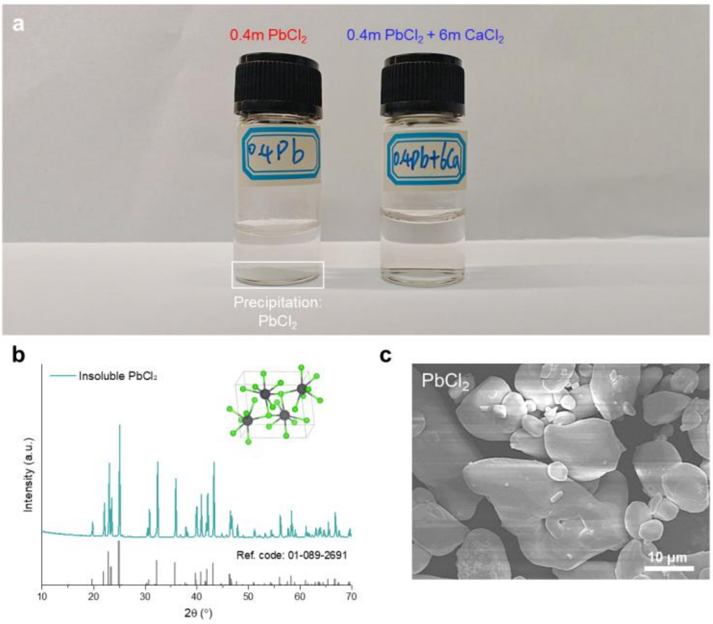

Supplementary Fig. 41 | Salting-in solubility of Pb^{2+} in 6 m $CaCl_2$-based SICE via $[PbCl_3]^-$ coordination. a, Optical image of 0.4 m $PbCl_2$ solution before and after addition of 6 m $CaCl_2$. **b**, XRD pattern of crystalline $PbCl_2$ precipitate in 0.4 m $PbCl_2$ solution; inset illustrates its crystal structure. **c**, SEM image of insoluble $PbCl_2$.

Supplementary Note 6.2. From hydrolysis-prone $SnCl_2$ to soluble $[SnCl_3]^-$ (Supplementary Figs. 42, 47a)

Aqueous $SnCl_2$ solutions are intrinsically unstable under ambient conditions because Sn^{2+} is readily oxidized by dissolved oxygen to Sn^{4+} (ref. 5), leading to hydrolysis and precipitation of SnO_2 according to $2Sn^{2+} + O_2 \rightarrow 2SnO_2$, as shown in Supplementary Fig. 47. Strong acids such as H_2SO_4 can alleviate the oxidative hydrolysis of Sn^{2+} in aqueous solutions; however, they simultaneously induce severe corrosion of Sn metal[6]. This issue was effectively addressed in our $CaCl_2$-based SICE by promoting the formation of soluble chlorocomplexes. As shown in Fig. 2i, Raman spectroscopy clearly identifies the chorocomplex as $[SnCl_3]^-$, characterized by two distinct Sn–Cl vibrational modes centered at ~260 cm^{-1} and ~220 cm^{-1}; notably, no signal corresponding to $[SnCl_4]^{2-}$ (~332 cm^{-1}) or $[Sn_2Cl_5]^-$ (~298 cm^{-1}) was detected[7,8], even at high $SnCl_2$ concentration up to 6 m in the 6 m $CaCl_2$ solution. This observation confirms that Sn^{2+} predominantly exists as $[SnCl_3]^-$ species across the tested concentration range, indicating a strong stabilization effect through Cl^- coordination. This behavior closely parallels that of Pb^{2+}. The three-coordination $[SnCl_3]^-$ complex is thermodynamically more stable than the four-coordination $[SnCl_4]^{2-}$, as reflected by its higher average Sn–Cl bond strength; structurally, $[SnCl_3]^-$ adopts a trigonal pyramidal geometry rather than an ideal planar arrangement, owing to the stereochemically active lone pair on the Sn^{2+} center (Supplementary Fig. 19b), which induces asymmetry and stabilizes the coordination environment. Similarly, IGMH analysis, based on the negative $sign(\lambda_2)\rho$ value at the peak δg_{inter} maximum, also reveals that the Sn–Cl interactions in $[SnCl_3]^-$ fall within the regime of strong halogen-bond-like contacts (Supplementary Fig. 47a). This structural and electronic stabilization explains the thermodynamic preference for the three-coordination complex. As a result, even under highly concentrated conditions (up to 6 m $SnCl_2$ in 6 m $CaCl_2$), Sn^{2+} remains predominantly as soluble $[SnCl_3]^-$ complexes (Fig. 2j), effectively suppressing hydrolysis and precipitation. This is evidenced by the clear appearance of the solutions (Supplementary Fig. 42a), in sharp contrast to the turbid suspensions observed in $CaCl_2$-free aqueous media.

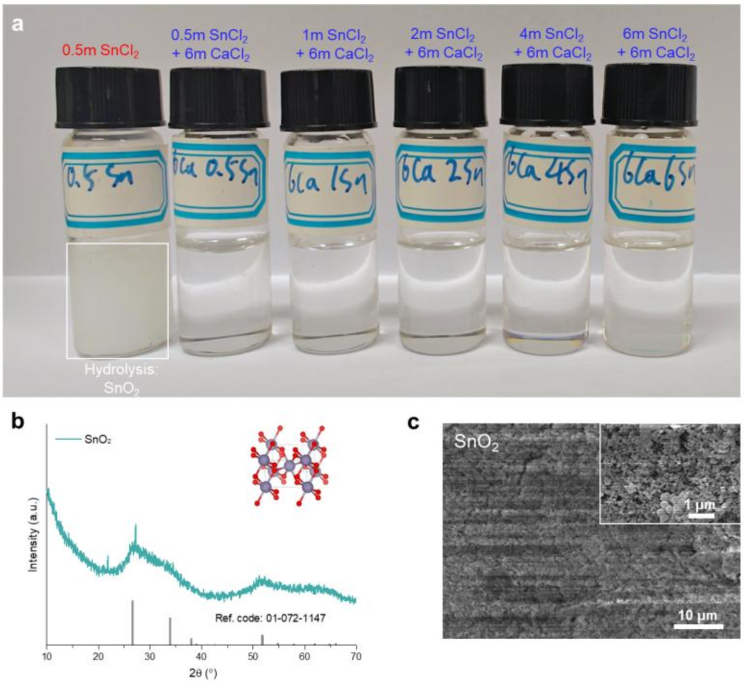

Supplementary Fig. 42 | Salting-in stabilization of Sn^{2+} in 6 m $CaCl_2$-based SICE via $[SnCl_3]^-$ coordination. a, Photograph showing hydrolysis and precipitation in 0.5 m $SnCl_4$ solution vs. clear and stable 6 m $CaCl_2$ solutions with increasing $SnCl_2$ concentrations. **b**, XRD pattern of hydrolysis product identified as crystalline SnO_2 in 0.5 m $SnCl_2$ solution; inset shows SnO_2 crystal structure. **c**, SEM image of hydrolyzed SnO_2 product.

Supplementary Note 6.3. From hydrolysis-prone $SbCl_3$ to soluble $[SbCl_4]^-$ (Supplementary Figs. 43, 47b)

Sb^{3+} is highly susceptible to hydrolysis in water due to their high charge density and strong Lewis acidity, which confer a strong affinity for H_2O molecules according to Hard–Soft Acid–Base theory[9]. As a result, $SbCl_3$ readily undergoes hydrolysis under ambient aqueous conditions, leading to the formation of insoluble $Sb_4O_5Cl_2$ precipitates (Supplementary Fig. 43). The introduction of 6 m $CaCl_2$ effectively suppresses this hydrolysis by promoting strong Cl^- coordination, thereby stabilizing Sb^{3+} in soluble chlorocomplex forms. Under these conditions, $SbCl_3$ can be fully dissolved at concentrations up to 4 m without visible precipitation (Supplementary Fig. 43a), in sharp contrast to its behavior in water. Raman spectroscopy reveals broad vibrational bands centered at 300–330 cm^{-1} and near 250 cm^{-1} (Fig. 2j), characteristic of Sb–Cl stretching modes in $[SbCl_4]^-$ complexes; meanwhile, signals at ~325 cm^{-1} and ~260 cm^{-1} suggest the possible coexistence of $[SbCl_6]^{3-}$ species[10]. These Raman profiles, together with literature-reported assignments, indicate that $[SbCl_4]^-$ is the dominant chlorocomplex in the concentrated chloride medium, with a potentially minor contribution from $[SbCl_6]^{3-}$. First-principles calculations support this experimental observation. The optimized $[SbCl_4]^-$ complex adopts a tetrahedral geometry with a total Sb–Cl binding energy of –50.10 eV, whereas $[SbCl_6]^{3-}$ forms an octahedral structure with a total binding energy of –45.92 eV (Supplementary Fig. 20b). Although both species exhibit large overall binding energies—indicating that both chlorocomplexes are thermodynamically stable—the average Sb–Cl bond strength is significantly higher in $[SbCl_4]^-$ than in $[SbCl_6]^{3-}$. Further IGMH analysis, based on the negative $sign(\lambda_2)\rho$ value at the peak $\delta g_{\mathrm{inter}}$ maximum, reveals that the Sb–Cl interactions in the four-coordination $[SbCl_4]^-$ complex exhibit binding strengths comparable to those in the three-coordinate $[SnCl_3]^-$ complex, likewise falling within the regime of strong halogen-bond-like contacts and underscoring the structural stability of $[SbCl_4]^-$ (Supplementary Fig. 47a, b). These thermodynamic and spectroscopic results demonstrate that concentrated $CaCl_2$ environments stabilize Sb^{3+} predominantly as $[SbCl_4]^-$, thereby effectively suppressing hydrolysis and enabling the high solubility of $SbCl_3$ in aqueous media (Supplementary Fig. 43a).

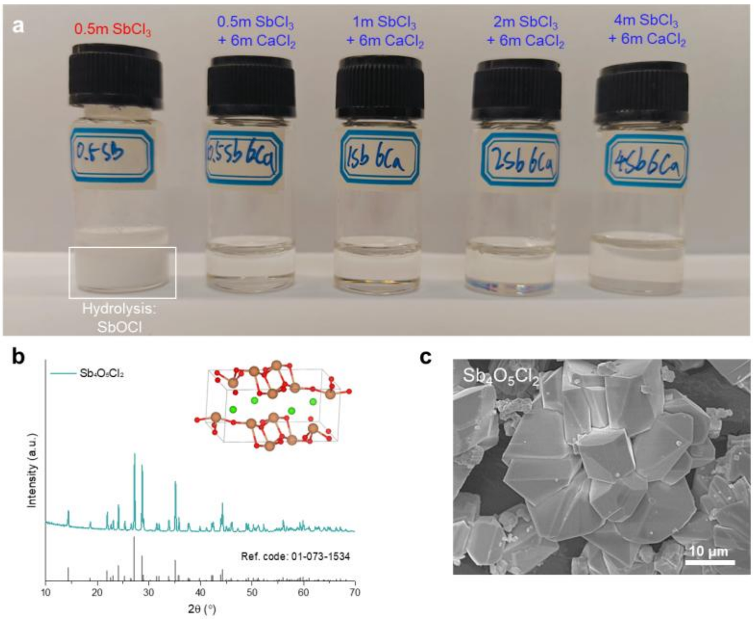

Supplementary Fig. 43 | Salting-in stabilization of Sb^{3+} in 6 m $CaCl_2$-based SICE via $[SbCl_4]^-$ coordination. a, Photograph showing hydrolysis and precipitation in 0.5 m $SbCl_3$ solution vs. clear and stable 6 m $CaCl_2$ solutions with increasing $SbCl_3$ concentrations. **b**, XRD pattern of hydrolysis product identified as crystalline $Sb_4O_5Cl_2$ in 0.5 m $SbCl_3$ solution; inset shows $Sb_4O_5Cl_2$ crystal structure. **c**, SEM image of hydrolyzed $Sb_4O_5Cl_2$ product.

Supplementary Note 6.4. From hydrolysis-prone $BiCl_3$ to soluble $[BiCl_6]^{3-}$ (Supplementary Figs. 44, 47c)

Similar to Sb^{3+}, Bi^{3+} is highly susceptible to hydrolysis in aqueous environments due to their high charge density and strong affinity for H_2O molecules, readily leading to the formation of insoluble BiOCl precipitates (Supplementary Fig. 44). The presence of 6 m $CaCl_2$ effectively suppresses this hydrolysis by stabilizing Bi^{3+} through chlorocomplex formation. As shown in Supplementary Fig. 44a, $BiCl_3$ concentrations up to 2.5 m can be fully dissolved without visible precipitation. Raman spectroscopy confirms that Bi^{3+} predominantly exists as soluble $[BiCl_6]^{3-}$ complexes across the tested $BiCl_3$ concentration range (Fig. 2k). Characteristic Bi–Cl vibrational bands at ~260 cm^{-1} and ~215 cm^{-1} match well with literature-reported signatures of $[BiCl_6]^{3-}$ species[11], and their intensities increase systematically with increasing $BiCl_3$ concentration, indicating the progressive formation and stabilization of $[BiCl_6]^{3-}$ under concentrated chloride conditions. This experimental evidence is consistent with our first-principles calculations, which show that $[BiCl_6]^{3-}$ adopts a stable octahedral coordination geometry with a total Bi–Cl binding energy of –44.49 eV (Supplementary Fig. 21b). Notably, while Sb^{3+} favors a four-coordination $[SbCl_4]^-$ complex in 6 m $CaCl_2$, Bi^{3+} predominantly forms the six-coordination $[BiCl_6]^{3-}$ complex. IGMH analysis, based on the negative $sign(\lambda_2)\rho$ value at the peak δg_{inter} maximum, reveals that the Bi–Cl interactions in $[BiCl_6]^{3-}$ fall within the regime of stable halogen-bond-like contacts, albeit weaker than those in [$SbCl_4$]$^{-}$ due to the higher CN (Supplementary Fig. 47b, c). These interactions are predominantly ionic in nature, consistent with the stabilization mechanism of chlorocomplexes, and the formation of this stable six-coordination chlorocomplex effectively suppresses Bi^{3+} hydrolysis and enables the high solubility of $BiCl_3$ in aqueous media.

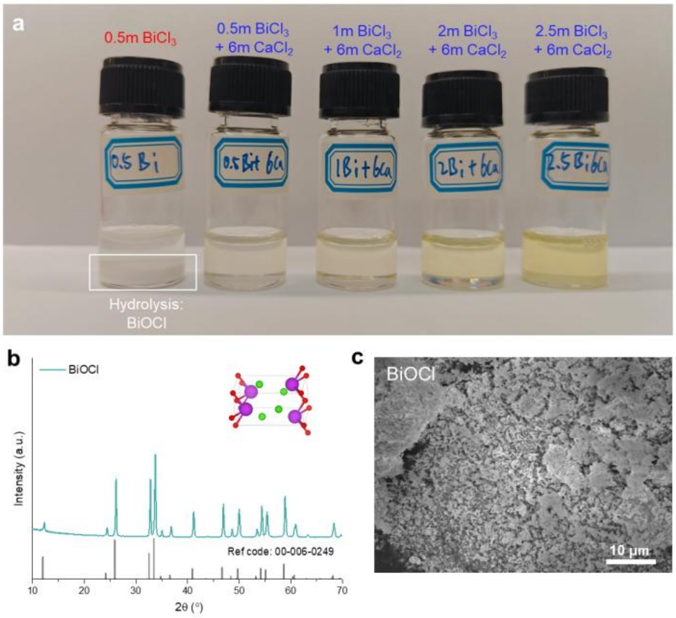

Supplementary Fig. 44 | Salting-in stabilization of Bi^{3+} in 6 m $CaCl_2$-based SICE via [$BiCl_6$]$^{3-}$ coordination. a, Photograph showing hydrolysis and precipitation in 0.5 m $BiCl_3$ solution vs. clear and stable 6 m $CaCl_2$ solutions with increasing $BiCl_3$ concentrations. **b**, XRD pattern of hydrolysis product identified as crystalline BiOCl in 0.5 m $BiCl_3$ solution; inset shows BiOCl crystal structure. **c**, SEM image of hydrolyzed BiOCl product.

Supplementary Note 6.5. From hydrolysis-prone $TeCl_4$ to soluble [$TeCl_6$]$^{2-}$ (Supplementary Figs. 45, 47d)

$TeCl_4$ exhibits pronounced hydrolysis behavior in aqueous environments due to the high charge density and strong Lewis acidity of Te^{4+}, which readily reacts with H_2O molecules to form insoluble TeO_2 precipitates according to the reaction of $Te^{4+} + 2H_2O \rightarrow TeO_2 + 4H^{+}$, (Supplementary Fig. 45). This issue is effectively overcome in 6 m $CaCl_2$ solution, where the highly concentrated chloride environment promotes the formation of stable chlorocomplexes, thereby suppressing the hydrolysis of Te^{4+} up to 3 m $TeCl_4$ (Supplementary Fig. 45a). Raman spectroscopy confirms that Te^{4+} predominantly forms [$TeCl_6$]$^{2-}$ chlorocomplexes in the 6 m $CaCl_2$ solution (Fig. 2l). The characteristic Te–Cl vibrational bands at ~290 cm^{-1} and ~250 cm^{-1} are consistent with previously reported spectral features of [$TeCl_6$]$^{2-}$ species[12]. The progressive enhancement of these bands with increasing $TeCl_4$ concentration provides clear evidence for the stabilization of [$TeCl_6$]$^{2-}$ under concentrated chloride conditions. DFT calculations further corroborate this assignment, showing that the optimized $[TeCl_6]^{2-}$ structure adopts an octahedral geometry with a total binding energy of –90.33 eV (Supplementary Fig. 22b). Notably, the total binding energy of $[TeCl_6]^{2-}$ is significantly higher than that of $[SnCl_3]^-$ (–23.56 eV, Supplementary Fig. 19b), whereas the individual Te–Cl bond strength is comparable to the Sn–Cl bond strength in $[SnCl_3]^-$. This is evidenced by IGMH analysis, where the negative $sign(\lambda_2)\rho$ values at the peak $\delta g_{\mathrm{inter}}$ maxima are similar for both species, indicating the presence of strong halogen-bond-like contacts (Supplementary Fig. 47a, d). These experimental and theoretical findings collectively establish that $[TeCl_6]^{2-}$ as the predominant chlorocomplex stabilized in the 6 m $CaCl_2$ medium.

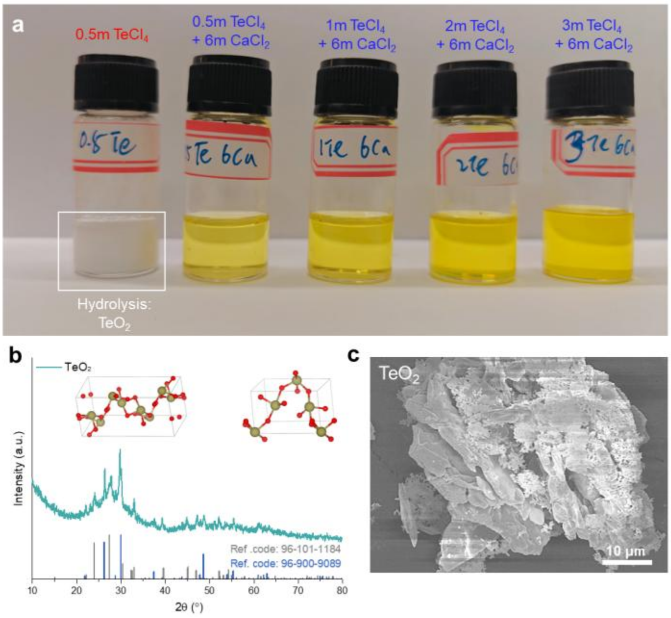

Supplementary Fig. 45 | Salting-in stabilization of Te^{4+} in 6 m $CaCl_2$-based SICE via $[TeCl_6]^{2-}$ coordination. a, Photograph showing hydrolysis and precipitation in 0.5 m $TeCl_4$ solution vs. clear and stable 6 m $CaCl_2$ solutions with increasing $TeCl_4$ concentrations. **b**, XRD pattern of hydrolysis product identified as two different crystalline TeO_2 in 0.5 m $TeCl_4$ solution; insets show corresponding two TeO_2 crystal structures. **c**, SEM image of hydrolyzed TeO_2 product.

Supplementary Note 6.6. From hydrolysis-full Se^{4+} to hydrolysis-partial Se^{4+} (Supplementary Figs. 46, 48, 49)

Unlike the other HPE cations (Pb^{2+}, Sn^{2+}, Sb^{3+}, Bi^{3+}, and Te^{4+}), Se^{4+} exhibits a fundamentally different behavior in aqueous media. When 1 m $SeCl_4$ is dissolved in water, rapid hydrolysis occurs, producing a nearly colorless solution; in contrast, dissolving 1 m $SeCl_4$ in 6 m $CaCl_2$ results in a clear yellow solution (Supplementary Fig. 46). Raman spectroscopy provides direct insight into the chemical nature of these two solutions. In pure aqueous $SeCl_4$ solution, prominent vibrational features characteristic of H_2SeO_3 are observed, including Se=O stretching modes at ~895 cm^{-1}

and Se–OH vibrations near 690 cm^{-1} (Ref. 13), confirming the complete hydrolysis of Se^{4+} into H_2SeO_3 (Fig. 2m). In contrast, upon introducing 6 m $CaCl_2$, the Raman spectrum exhibits new two peaks near 350–250 cm^{-1}, attributable to Cl–Se–Cl and O=Se–Cl stretching modes associated with $SeOCl_2$ species[14]. This behavior contrasts sharply with our previous simulations of Se^{4+} coordinated exclusively by Cl^{-}, which predicted soluble chlorocomplexes (Supplementary Fig. 23b). The partial hydrolysis observed under high Cl^{-} concentrations can be attributed to the competitive coordination of Cl^{-} with Se^{4+}, which stabilizes Se^{4+} against direct attack by H_2O molecules. Nevertheless, due to the intrinsic high reactivity of Se^{4+} toward nucleophilic oxygen donors of H_2O molecules (Supplementary Fig. 23a), complete suppression of hydrolysis remains challenging, resulting in the formation of partially hydrolyzed $SeOCl_2$ in concentrated $CaCl_2$ electrolytes (Fig. 2m and Supplementary Fig. 46). DFT structure optimizations further corroborate these observations. Four Se^{4+} species were modeled, including fully hydrolyzed H_2SeO_3, its deprotonated forms $HSeO_3^{-}$ and SeO_3^{2-}, and the partially hydrolyzed/partially chlorinated $SeOCl_2$ (top row of Supplementary Fig. 48). ELF maps (isosurfaces value = 0.5) analysis reveal that all four complexes adopt a trigonal pyramidal geometry (bottom row of Supplementary Fig. 48), consistent with the presence of a stereochemically active lone pair on Se^{4+} that induces spatial asymmetry and limits ligand rearrangement. These structural features match well with the Raman spectral assignments (Fig. 2m), highlighting the intrinsic O-donor preference of Se^{4+}.

IGMH maps provide quantitative insight into the bonding characteristics underlying the observed kinetic contrast (Supplementary Fig. 49). For H_2SeO_2, $HSeO_3^{-}$ and SeO_3^{2-}, the $\delta g_{\mathrm{inter}}$ maxima are located in deep-blue regions at markedly negative $sign(\lambda_2)\rho$ values, indicating that the Se–O and Se–OH bonds possess appreciable covalent character and are associated with high bond scission barriers (Supplementary Fig. 49a–c). In $SeOCl_2$, by contrast, the two Se–Cl contacts fall within moderately negative (blue) domains characteristic of halogen-bond–like, weaker interactions, while the Se–O feature is shifted toward less-negative $sign(\lambda_2)\rho$ values and exhibits less negative $\delta g_{\mathrm{inter}}$ relative to H_2SeO_2, reflecting attenuated covalency (Supplementary Fig. 49d). Therefore, these experimental and theoretical results reveal that Se^{4+} fundamentally differs from other HPE cations in that Cl^{-} cannot fully displace aqua, hydroxo, or oxo ligands. Instead, Se^{4+} stabilizes through oxo–chloride mixed coordination, favoring the formation of $SeOCl_2$ rather than purely chlorinated complexes. These bonding fingerprints rationalize the electrochemical behavior: $SeOCl_2$ undergoes reduction more rapidly because the process can proceed through a dissociative pathway involving the cleavage of two Se–Cl bonds with a lower bond dissociation energy, whereas H_2SeO_3 and its derivatives require the cleavage of three stronger Se–O and Se–OH bonds via multi-step proton-coupled electron transfer, resulting in sluggish reduction kinetics. This mechanistic distinction explains the electrochemical signatures: the $SeOCl_2$/Se redox couple exhibits low polarization and high current response, whereas the H_2SeO_3/Se redox couple shows pronounced polarization and sluggish kinetics (Fig. 3b, and Supplementary Fig. 66a, b).

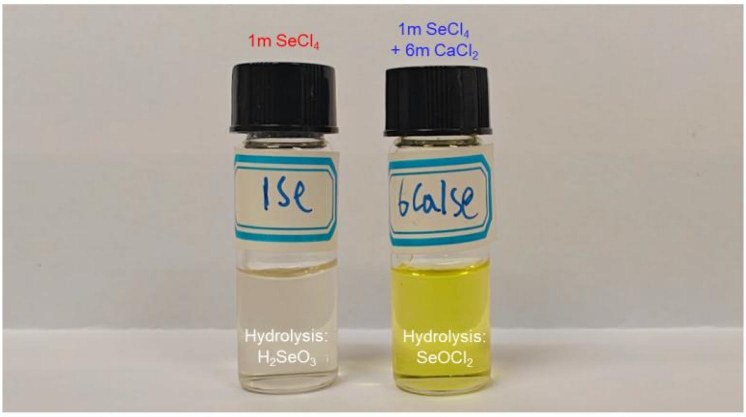

Supplementary Fig. 46 | Salting-in stabilization of Se^{4+} in 6 m $CaCl_2$-based SICE via $SeOCl_2$ coordination. Photograph showing complete Se^{4+} hydrolysis in 1 m $SeCl_4$ solution and partial Se^{4+} hydrolysis in 1 m $SeCl_4$ + 6 m $CaCl_2$ solution.

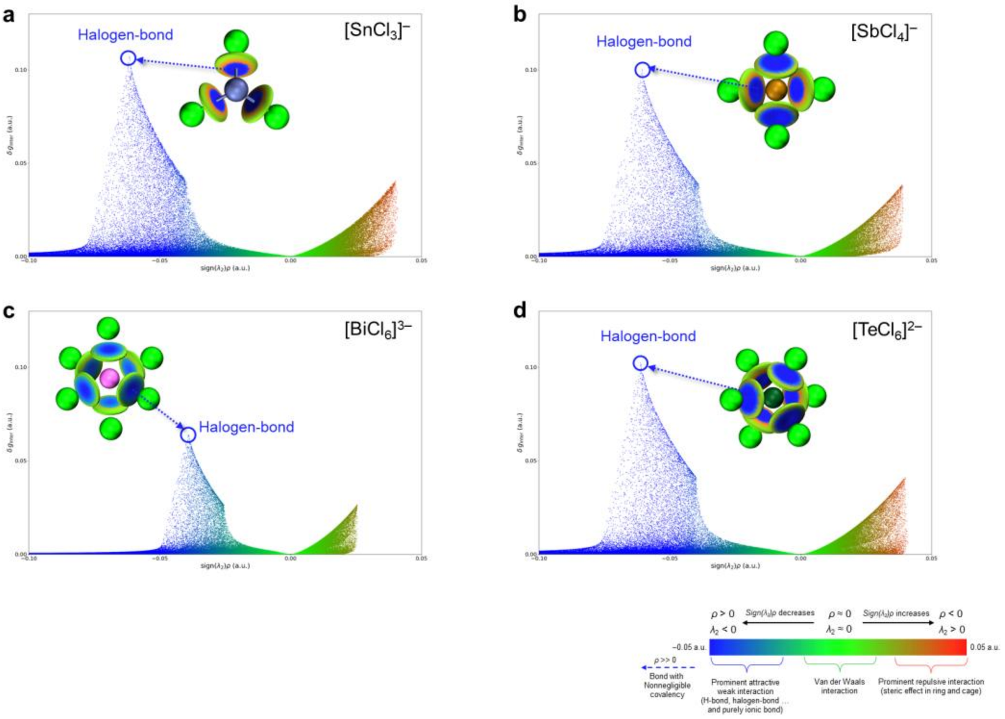

Supplementary Fig. 47 | IGMH analysis focusing exclusively on HPE cation–Cl⁻ interactions. a–d, Scatter plots of $\delta g_{\mathrm{inter}}$ vs. $sign(\lambda_2)\rho$ for cation–Cl^- interactions in $[\mathrm{SnCl_3}]^-$ (a), $[\mathrm{SbCl_4}]^-$ (b), $[\mathrm{BiCl_6}]^{3-}$ (c), and $[\mathrm{TeCl_6}]^{2-}$ (d). Insets: inter-fragment IGMH isosurfaces at $\delta g_{\mathrm{inter}} = 0.01$ a.u., colored by $sign(\lambda_2)\rho$. This panel highlights the interactions of Sn^{2+}, Sb^{3+}, Bi^{3+}, and Te^{4+} with Cl^-, enabling identification and comparison of interaction nature and strength across different chlorocomplexes.

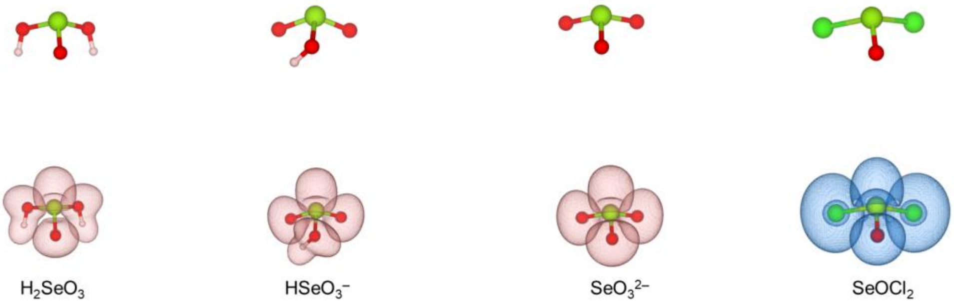

Supplementary Fig. 48 | Structures of oxo/chloro derivatives of Se(IV). DFT-optimized structures and corresponding ELF analysis (isosurface value = 0.5) of H_2SeO_3, $HSeO_3^-$, SeO_3^{2-}, and $SeOCl_2$.

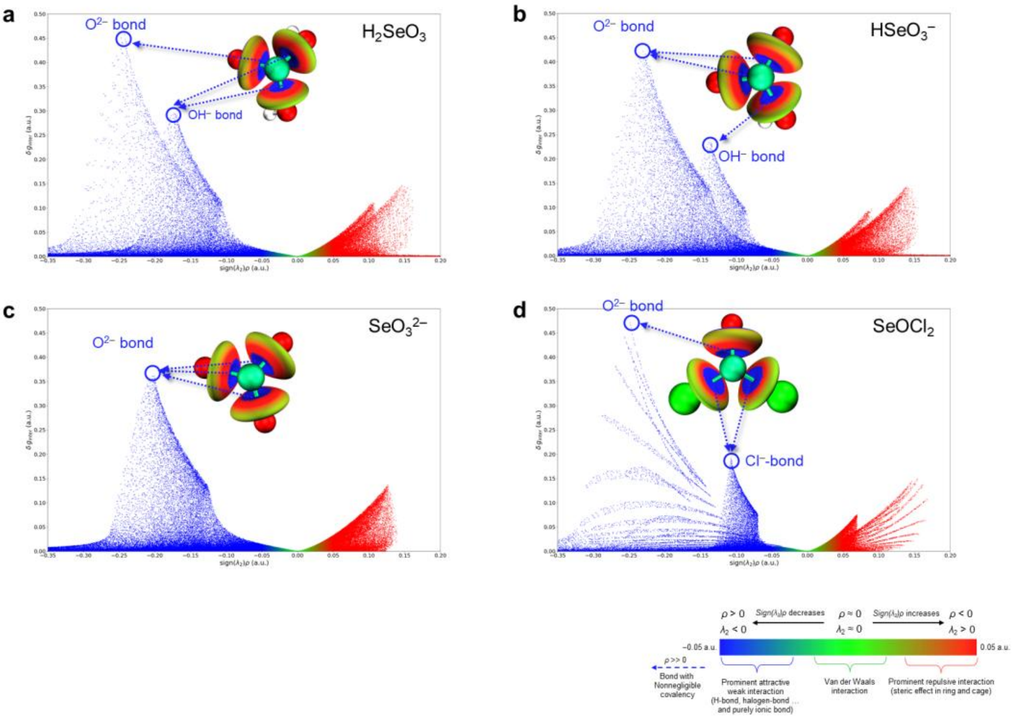

Supplementary Fig. 49 | IGMH analysis focusing exclusively on HPE cation–Cl⁻ interactions. a–d, Scatter plots of $\delta g_{\mathrm{inter}}$ vs. $sign(\lambda_2)\rho$ for interactions between Se^{4+} and surroding ion species in H_2SeO_3 (a), $HSeO_3^{-}$ (b), SeO_3^{2-} (c), and $SeOCl_2$ (d). Insets: inter-fragment IGMH isosurfaces at $\delta g_{\mathrm{inter}} = 0.01$ a.u., colored by $sign(\lambda_2)\rho$.

Supplementary Note 7. Three-electrode configurations for multielectron electrochemistry of HPEs (Supplementary Figs. 50, 51)

To enable the electrochemical investigation of HPEs, three types of conductive current collectors were specifically prepared, as shown in Supplementary Fig. 50. These include commercial Cu foil (Supplementary Fig. 50a, d, g), commercial Ti foil (Supplementary Fig. 50b, e, h), and a customized KB carbon-coated Ti mesh (Supplementary Fig. 50c, f, i). The corresponding XRD patterns confirm the phase purity of Cu (ref. code: 96-901-3018) and Ti (ref. code: 96-900-8518) substrates, while the KB-coated Ti mesh shows characteristic diffraction peaks from Ti along with a broad carbon signal. The HPE electrodes employed in this work are summarized in Supplementary Fig. 51. Commercially available Sn foil (Supplementary Fig. 51a, g, m; ref. code: 01-089-2958), Pb foil (Supplementary Fig. 51b, h, n; ref. code: 03-065-2873), and Bi foil (Supplementary Fig. 51d, j, p; ref. code: 96-500-0216) were used as electrodes after rolling to the thickness of 100 μm. For Sb, Se, and Te, powder materials were coated onto Ti meshes via a pressing method to fabricate the Sb (Supplementary Fig. 51c, i, o; ref. code: 96-500-0215), Se (Supplementary Fig. 51e, k, q; ref. code: 00-006-0362), and Te (Supplementary Fig. 51f, l, r; ref. code: 00-004-0555) electrodes. The XRD patterns of the prepared electrodes confirm the expected phases with no detectable impurity peaks, ensuring the structural integrity of the counter electrodes during subsequent electrochemical evaluations. The CV behaviors of the HPEs were systematically investigated using a three-electrode beaker cell configuration. KB carbon-coated Ti mesh served as the working electrode, while the corresponding HPE electrodes acted as the counter electrodes, and a KCl-saturated Ag/AgCl electrode (+0.199 V vs. SHE) was employed as the reference electrode. The electrolytes were individually tailored for each element to ensure appropriate solubility and stable complexation. Specifically, 1 m $SeCl_4$ electrolyte was used for Se deposition, while 1 m $SeCl_4$ + 6 m $CaCl_2$ solution was used to stabilize Se chlorocomplexes and suppress hydrolysis. For the remaining HPEs, the electrolyte systems included 1 m $SnCl_2$ + 6 m $CaCl_2$ (for Sn), 1 m $SbCl_3$ + 6 m $CaCl_2$ (for Sb), 1 m $BiCl_3$ + 6 m $CaCl_2$ (for Bi), and 1 m $TeCl_4$ + 6 m $CaCl_2$ (for Te). It is noteworthy that due to the limited solubility of $PbCl_2$ in 6 m $CaCl_2$ (~0.4 m), the Pb electrochemical tests were conducted in a 0.4 m $PbCl_2$ + 6 m $CaCl_2$ electrolyte. Fig. 3a, b, present the representative CV curves at a scan rate of 1 mV s^{-1}, demonstrating the distinct redox behavior of each HPE species. Moreover, Fig. 3c presents the galvanostatic deposition profiles recorded at a constant current density of 10 mA cm^{-2} using this three-electrode configuration, confirming the stable electrodeposition behavior of each HPE. Specifically, Cu foil, Ti foil, and KB-coated Ti mesh were used as current collectors for Sn and Pb, Sb and Bi, and Se and Te, respectively, tailored to match the distinct electrochemical and adhesion characteristics of each system.

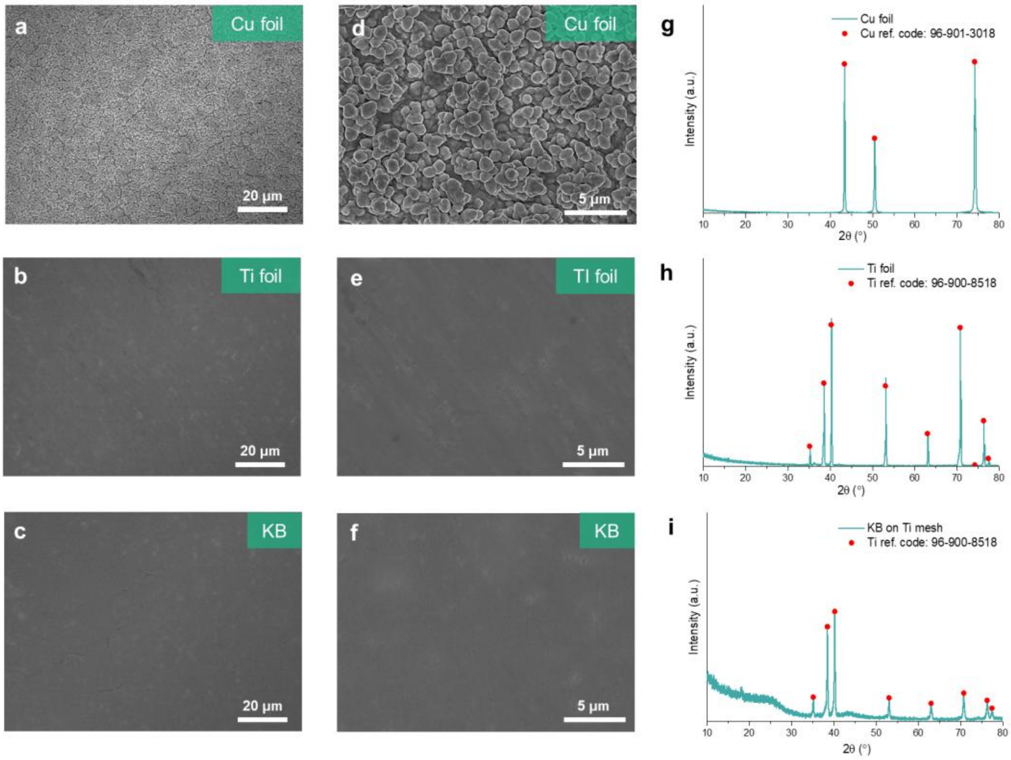

Supplementary Fig. 50 | Current collector used to investigate HPE plating/stripping behaviors. **a–f**, SEM images of Cu foil (a, d), Ti foil (b, e), and KB on Ti mesh (c, f) current collectors. **g–i**, Corresponding XRD patterns of Cu foil (g), Ti foil (h), and KB on Ti mesh (i).

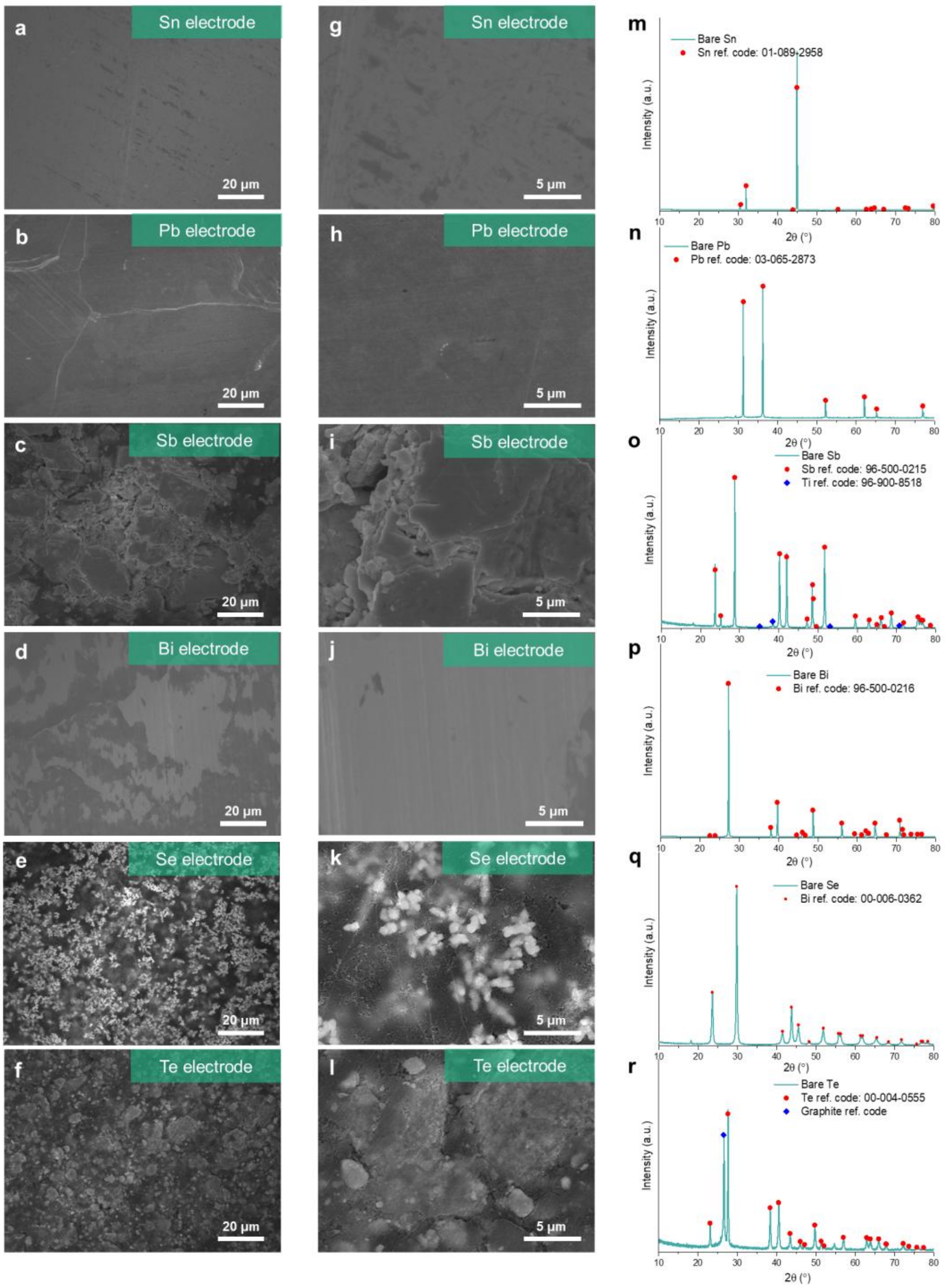

Supplementary Fig. 51 | HPE electrodes used for electrochemistry studies. a–l, SEM images of bare Sn (a, g), Pb (b, h), Sb (c, i), Bi (d, j), Se (e, k), and Te (f, l) electrodes. **m–r**, Corresponding XRD patterns of Sn (m), Pb (n), Sb (o), Bi (p), Se (q) and Te (r) electrodes.

Supplementary Note 8. Electrodeposition of HPEs and their alloys in SICEs (Supplementary Figs. 52–61)

Supplementary Note 8.1. Electrodeposition for HPEs (Supplementary Figs. 52–58)

The deposition morphology of the HPEs was characterized after galvanostatic electrodeposition at a constant current density of 10 mA cm^{-2} for 1 h under the three-electrode beaker configuration. As shown in Supplementary Fig. 52, SEM images at multiple magnifications were collected to comprehensively assess the morphologies. All HPE electrodeposits, including Pb (Supplementary Fig. 52a), Sn (Supplementary Fig. 52b), Sb (Supplementary Fig. 52c), Bi (Supplementary Fig. 52d), Te (Supplementary Fig. 52e), and Se (f Supplementary Fig. 52f), exhibit regularly packed and continuous deposition across the substrate surface. Distinct microstructural features are observed for each HPE: Pb deposits displayed compact stacked crystal domains, Sn formed faceted polygonal grains, Sb showed closely packed granular morphology, Bi exhibited layered flake-like structures, Te presented large hemispherical grains, and Se formed uniform and dense films. FIB technology was employed to prepare cross-sectional lamellae of electrodeposited Pb, Sn, Sb, Bi, and Te (Supplementary Figs. 53a–c, 54a–c, 55a–c, 56a–c, 57a–c). These samples were subsequently analyzed using HAADF-STEM to reveal their atomic-level structural characteristics (Fig. 3j–n, and Supplementary Figs. 53d–f, 54d–f, 55d–f, 56d–f, 57d–f). For the Pb deposit (Fig. 3j, and Supplementary Fig. 53), HAADF-STEM elemental mapping confirmed a homogeneous Pb distribution (Supplementary Fig. 53d), while atomic-resolution imaging revealed a well-ordered atomic arrangement with a lattice spacing of ~0.29 nm corresponding to the (111) plane of Pb crystal (Fig. 3j, and Supplementary Fig. 53e, f). In the Sn sample (Fig. 3k, and Supplementary Fig. 54), the uniform elemental Sn distribution was observed from elemental mapping (Supplementary Fig. 54d), and atomic-resolution HAADF-STEM imaging with the corresponding FFT pattern identified a crystalline structure with a ~0.29 nm lattice spacing, assigned to the (200) plane of Sn crystal (Fig. 3k, and Supplementary Fig. 54e, f). The Sb electrodeposit exhibited homogeneous Sb distribution across the cross-section (Supplementary Fig. 55). Atomic-resolution imaging revealed well-defined atomic columns with an interplanar spacing of ~0.31 nm, indexed to the (112) plane (Fig. 3l, and Supplementary Fig. 55e, f). For the Bi deposit, EDS mapping verified the uniform presence of Bi (Supplementary Fig. 56), and atomic-resolution HAADF-STEM imaging demonstrated a regular lattice with an interplanar distance of ~0.23 nm, corresponding to the (110) plane of Bi crystal (Fig. 3m, and Supplementary Fig. 56e, f). In the case of Te, elemental mapping showed a pure elemental Te signal (Supplementary Fig. 57), and atomic-resolution HAADF-STEM revealed a highly ordered atomic arrangement with a ~0.22 nm spacing indexed to the (110) plane of Te crystal (Fig. 3n, and Supplementary Fig. 57e, f).

In contrast to the crystalline electrodeposits observed for other HPEs, the Se deposit exhibits an amorphous structure, as shown in Fig. 3o and Supplementary Fig. 58. The HAADF-STEM image and corresponding EDS elemental mapping confirm uniform Se distribution across the deposit (Supplementary Fig. 58a). Notably, the atomic-resolution HAADF-STEM image with the corresponding FFT image lack any discernible lattice fringes (Fig. 3o, and Supplementary Fig. 58b), verifying the amorphous nature of the atomic Se arrangement. To further verify the crystallographic features of the electrodeposited HPEs, XRD analyses were conducted, as presented in Fig. 3p. For Sn, Pb, Sb, Bi, and Te deposits, the diffraction peaks match well with their corresponding reference patterns, confirming the successful electrodeposition of phase-pure metallic Sn, Pb, Sb, Bi, and Te, respectively. These results are consistent with the observed highly crystalline microstructures in the SEM and atomic-resolution HAADF-STEM characterizations. In contrast, the XRD pattern of the Se deposit exhibits a broad hump without distinct diffraction peaks (Fig. 3p), further corroborating its amorphous nature, as previously evidenced by HAADF-STEM imaging (Fig. 3o and Supplementary Fig. 58b).

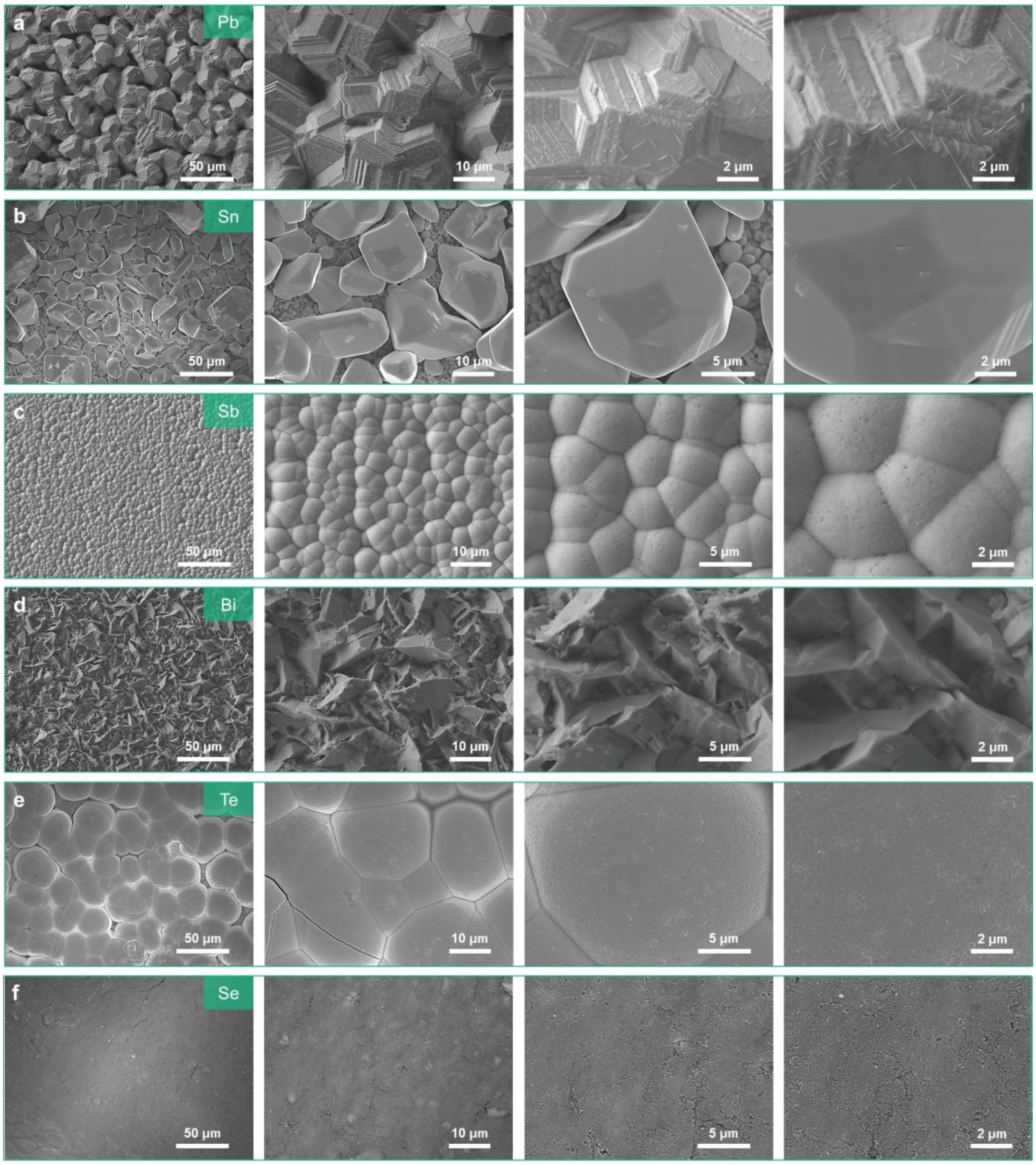

Supplementary Fig. 52 | Morphologies of HPE electrodeposits obtained from 6 m $CaCl_2$-based SICEs. a–f, SEM images of Pb (a), Sn (b), Sb (c), Bi (d), Te (e), and Se (f) electrodeposits after plating an areal capacity of 10 mAh cm^{-2} at a current density of 10 mA cm^{-2}, shown at different magnifications.

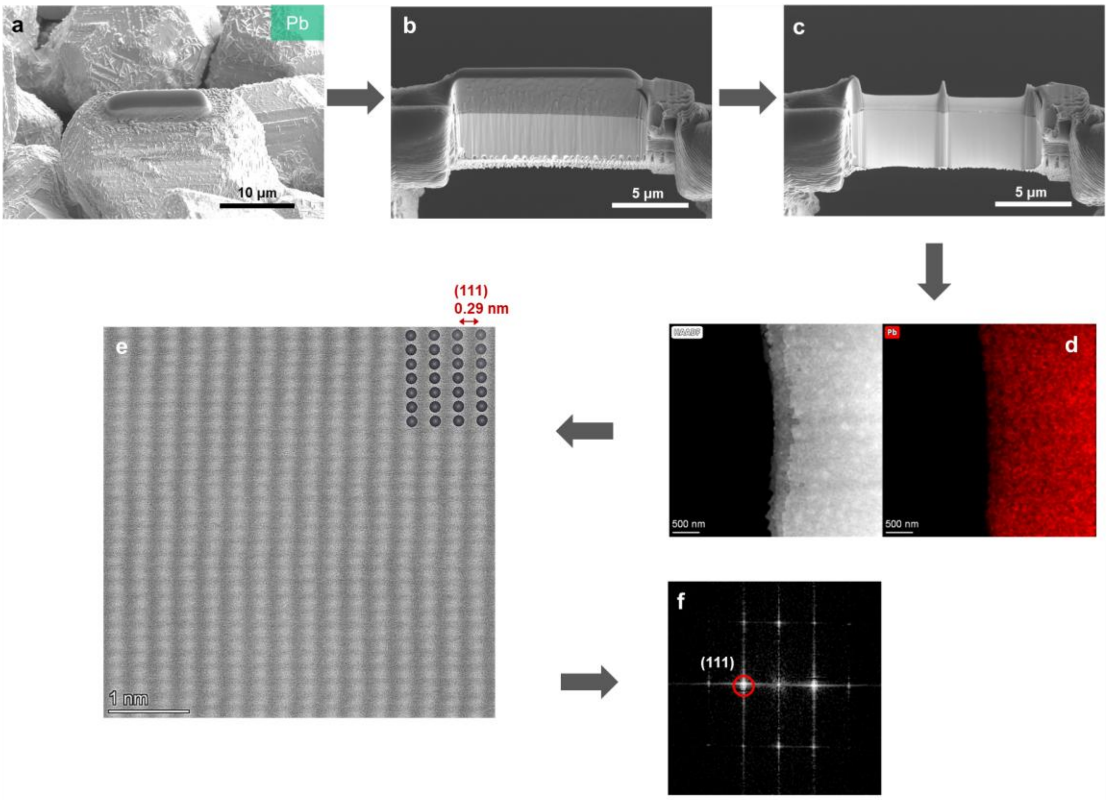

Supplementary Fig. 53 | Structural characterization of Pb electrodeposit obtained from 0.4 m $PbCl_2$ + 6 m $CaCl_2$ electrolyte after plating an areal capacity of 10 mAh cm^{-2} at a current density of 10 mA cm^{-2}. a–c, SEM images of FIB-prepared cross-sectioned Pb sample. **d**, HAADF-STEM image and corresponding EDS elemental map for Pb. **e**, Atomic-resolution HAADF-STEM image with superimposed structural simulation of atomic Sn arrangement. **f**, The corresponding FFT pattern of Pb.

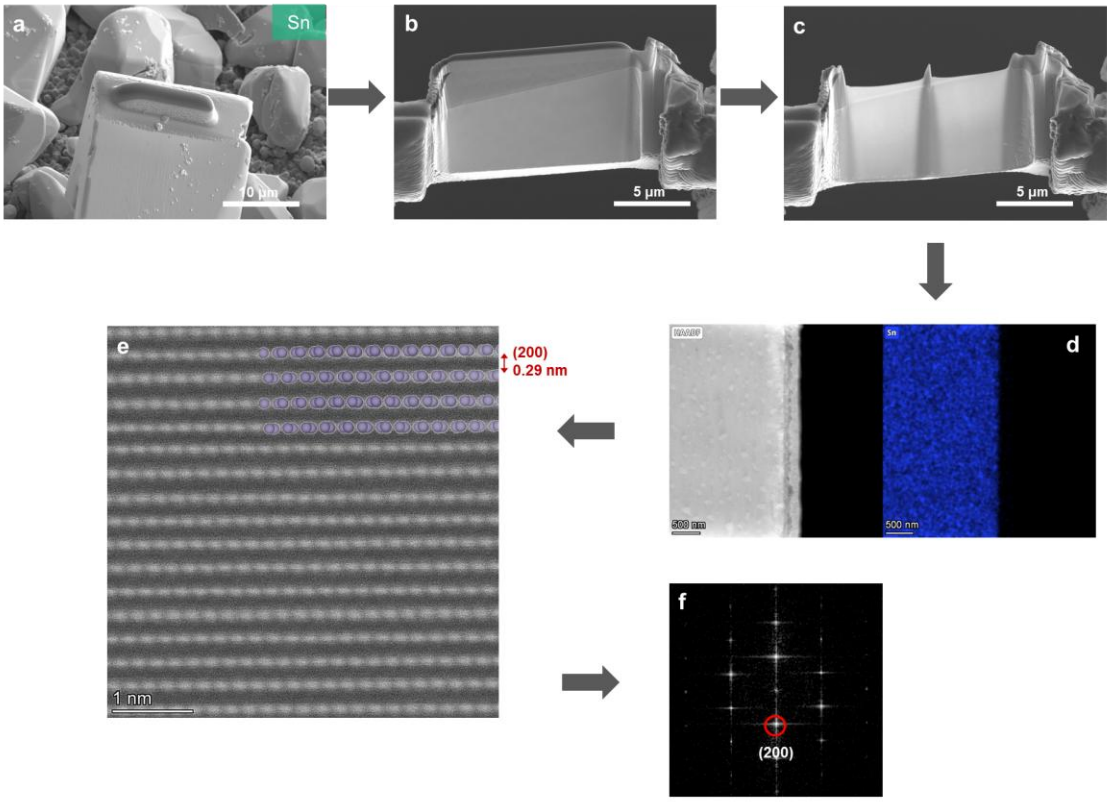

Supplementary Fig. 54 | Structural characterization of Sn electrodeposit obtained from 1 m $SnCl_2$ + 6 m $CaCl_2$ electrolyte after plating an areal capacity of 10 mAh cm^{-2} at a current density of 10 mA cm^{-2}. a–c, SEM images of FIB-prepared cross-sectioned Sn sample. **d**, HAADF-STEM image and corresponding EDS elemental map for Sn. **e**, Atomic-resolution HAADF-STEM image with superimposed structural simulation of atomic Sn arrangement. **f**, The corresponding FFT pattern of Sn.

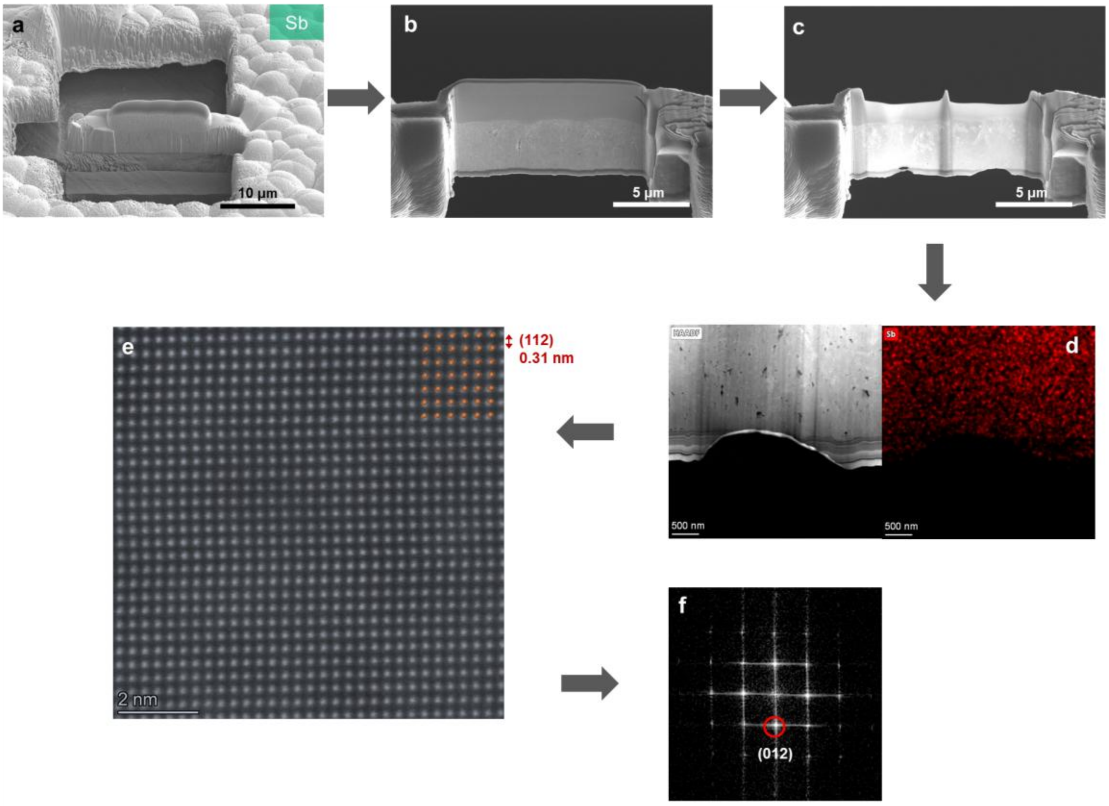

Supplementary Fig. 55 | Structural characterization of Sb electrodeposit obtained from 1 m $SbCl_3$ + 6 m $CaCl_2$ electrolyte after plating an areal capacity of 10 mAh cm^{-2} at a current density of 10 mA cm^{-2}. a–c, SEM images of FIB-prepared cross-sectioned Sb sample. **d**, HAADF-STEM image and corresponding EDS elemental map for Sb. **e**, Atomic-resolution HAADF-STEM image with superimposed structural simulation of atomic Sb arrangement. **f**, The corresponding FFT pattern of Sb.

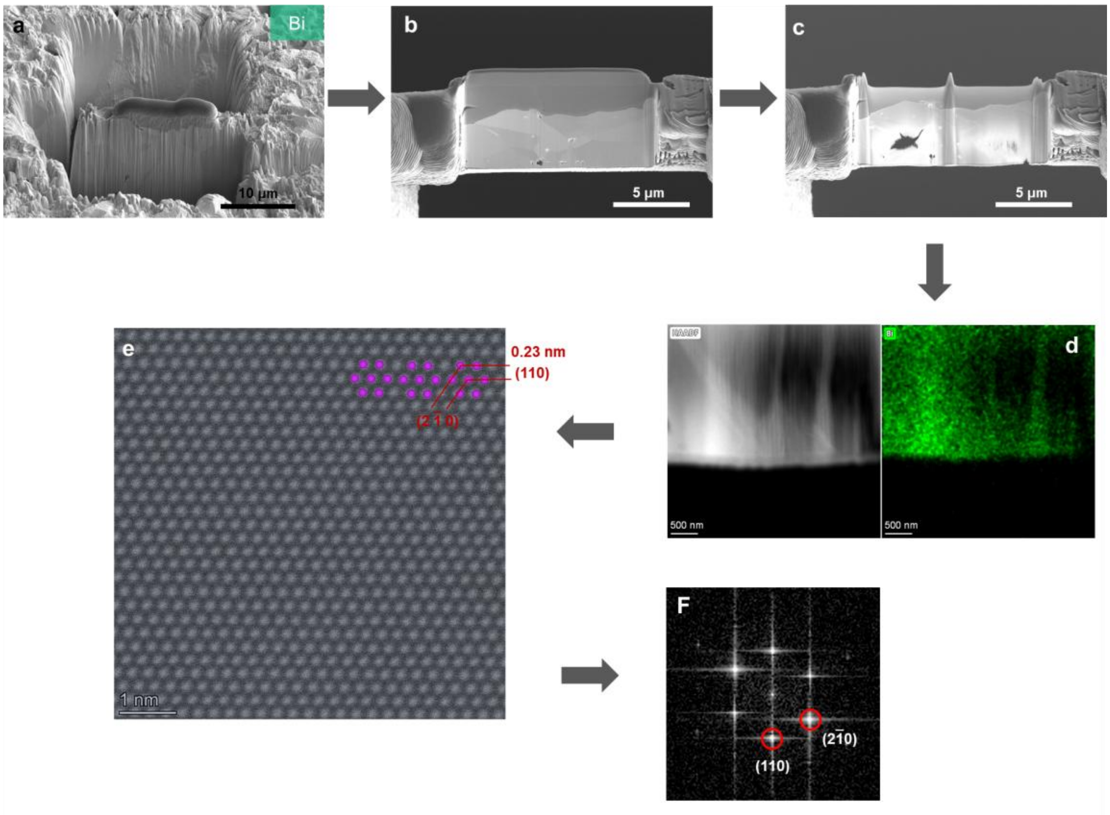

Supplementary Fig. 56 | Structural characterization of Bi electrodeposit obtained from 1 m $BiCl_3$ + 6 m $CaCl_2$ electrolyte after plating an areal capacity of 10 mAh cm^{-2} at a current density of 10 mA cm^{-2}. a–c, SEM images of FIB-prepared cross-sectioned Bi sample. **d**, HAADF-STEM image and corresponding EDS elemental map for Bi. **e**, Atomic-resolution HAADF-STEM image with superimposed structural simulation of atomic Bi arrangement. **f**, The corresponding FFT pattern of Bi.

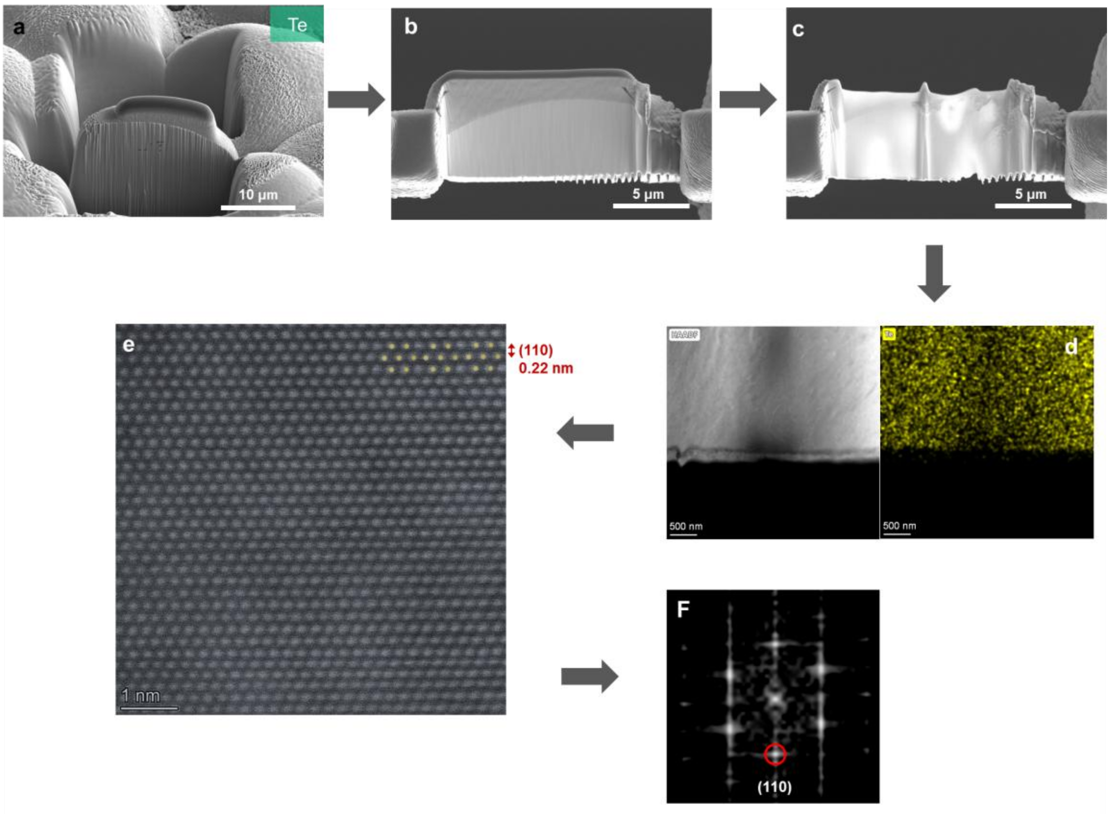

Supplementary Fig. 57 | Structural characterization of Te electrodeposit obtained from 1 m $TeCl_4$ + 6 m $CaCl_2$ electrolyte after plating an areal capacity of 10 mAh cm^{-2} at a current density of 10 mA cm^{-2}. a–c, SEM images of FIB-prepared cross-sectioned Te sample. **d**, HAADF-STEM image and corresponding EDS elemental map for Te. **e**, Atomic-resolution HAADF-STEM image with superimposed structural simulation of atomic Te arrangement. **f**, The corresponding FFT pattern of Te.

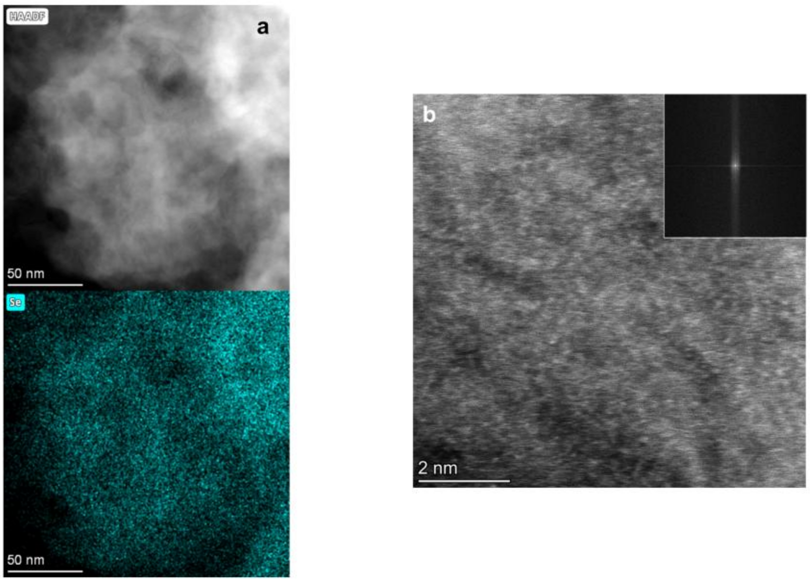

Supplementary Fig. 58 | Structural characterization of Se electrodeposit obtained from 1 m $SeCl_4$ + 6 m $CaCl_2$ electrolyte after plating an areal capacity of 10 mAh cm^{-2} at a current density of 10 mA cm^{-2}. a, HAADF-STEM image and corresponding EDS elemental map for Se deposit. **b**, Atomic-resolution HAADF-STEM image of amorphous atomic Se arrangement. Inset: the corresponding FFT image of Se.

Supplementary Note 8.2. Electrodeposition for HPE alloys (Supplementary Figs. 59–61)

Bi–Sb alloy films were synthesized via a galvanostatic deposition strategy using a three-electrode setup, where Cu foil served as the working electrode, Pt foil as the counter electrode, and a KCl-saturated Ag/AgCl electrode as the reference electrode. A series of hybrid $BiCl_3$/$SbCl_3$ salts with a fixed total HPE cations concentration of 1.0 m were formulated in 6 m $CaCl_2$ electrolyte to control the resulting alloy composition. As shown in Supplementary Fig. 59, SEM images and corresponding EDS elemental mapping analyses confirm homogeneous co-deposition of Bi and Sb across different alloy ratios. The 1Bi9Sb, 5Bi5Sb, and 9Bi1Sb alloys (derived from electrolytes containing 0.1 m $BiCl_3$ + 0.9 m $SbCl_3$, 0.5 m $BiCl_3$ + 0.5 m $SbCl_3$, and 0.9 m $BiCl_3$ + 0.1 m $SbCl_3$, respectively, each in 6 m $CaCl_2$) exhibit distinct yet well-integrated grain morphologies, with no observable phase segregation at the microscale. EDS spectra further validate the controlled composition of the Bi–Sb alloys (Supplementary Fig. 60a–c), confirming a gradual Bi enrichment with increasing $BiCl_3$ ratio in the electrolyte. Specifically, the Bi atomic ratio increases from 1.2 at% in 9Sb1Bi to 79.2 at% in 1Sb9Bi, demonstrating tunable alloying through electrolyte formulation. Complementary XRD patterns (Supplementary Fig. 60d) indicate the formation of the $Bi_{0.8}Sb_{0.2}$ alloy phase (ref. code: 01-084-4835) in the 1Bi9Sb deposit at a low $BiCl_3$ ratio, whereas for the 1Sb9Bi deposit, the XRD peaks exhibit a shift relative to those of pure Sb, confirming the formation of a new alloy phase. With an increased $BiCl_3$ content, the sample 5Sb5Bi corresponds to a $B_{0.06}Sb_{0.94}$ alloy phase (ref. code: 00-035-0517). These results collectively confirm that the Bi–Sb alloy composition and phase structure can be precisely modulated via electrolyte design, enabling rational control over the electrodeposition process and the resulting microstructure. Pb–Sn alloy was synthesized via a galvanostatic deposition strategy using a three-electrode setup, where Cu foil served as the working electrode, Pt foil as the counter electrode, and a KCl-saturated AgCl/Ag electrode as the reference electrode. The electrolyte comprised 0.36 m $PbCl_2$ and 0.04 m $SnCl_2$ in 6 m $CaCl_2$, yielding an alloy deposit denoted as 9Pb1Sn, corresponding to the mole ratio of Pb^{2+} to Sn^{2+}. As shown in Supplementary Fig. 61a, b, SEM imaging and corresponding EDS elemental mapping reveal a homogeneous co-deposition of Pb and Sn without obvious phase segregation at the microscale. The alloy composition, quantified by EDS analysis (Supplementary Fig. 61c), shows a Pb atomic ratio of 88.7 at% and a Sn atomic ratio of 11.3 at%, closely matching the designed electrolyte formulation. Complementary XRD analysis confirmed that the electrodeposit was predominantly composed of a Pb-rich $Pb_{0.951}Sn_{0.049}$ phase, accompanied by a minor $Pb_{0.015}Sn_{0.985}$ phase (Supplementary Fig. 61d). The diffraction peaks matched well with standard reference patterns (ref. code 01-085-4619 and ref. code 01-072-2802, respectively). These results collectively validate that a controlled Pb–Sn alloy composition and phase structure can be achieved through electrolyte design and galvanostatic deposition conditions.

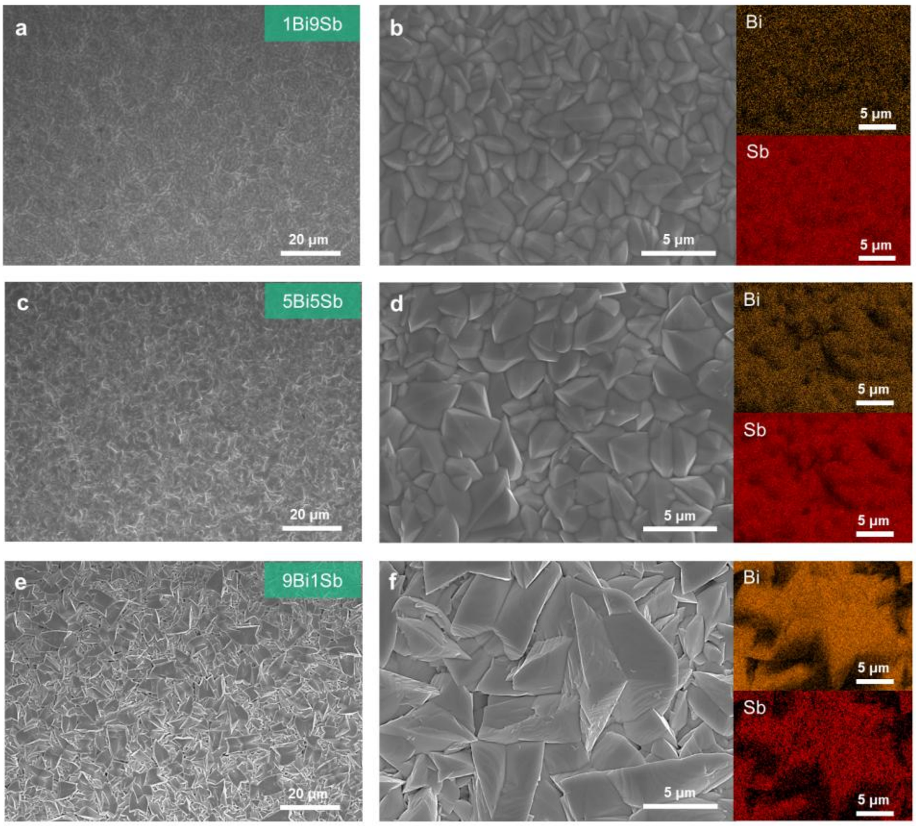

Supplementary Fig. 59 | Morphological and compositional characterization of BiSb alloy electrodeposits obtained at a current density of 10 mA cm^{-2} and a fixed areal capacity of 10 mAh cm^{-2} from 6 m $CaCl_2$-based SICEs. a, **b**, SEM image and corresponding EDS elemental map for BiSb deposit in 0.1 m $BiCl_3$ + 0.9 m $SbCl_3$ + 6 m $CaCl_2$ electrolyte (denoted as 1Bi9Sb). **c**, **d**, SEM image and corresponding EDS elemental map for BiSb deposit in 0.5 m $BiCl_3$ + 0.5 m $SbCl_3$ + 6 m $CaCl_2$ electrolyte (denoted as 5Bi5Sb). **e**, **f**, SEM image and corresponding EDS elemental map for BiSb deposit in 0.9 m $BiCl_3$ + 0.1 m $SbCl_3$ + 6 m $CaCl_2$ electrolyte (denoted as 9Bi1Sb).

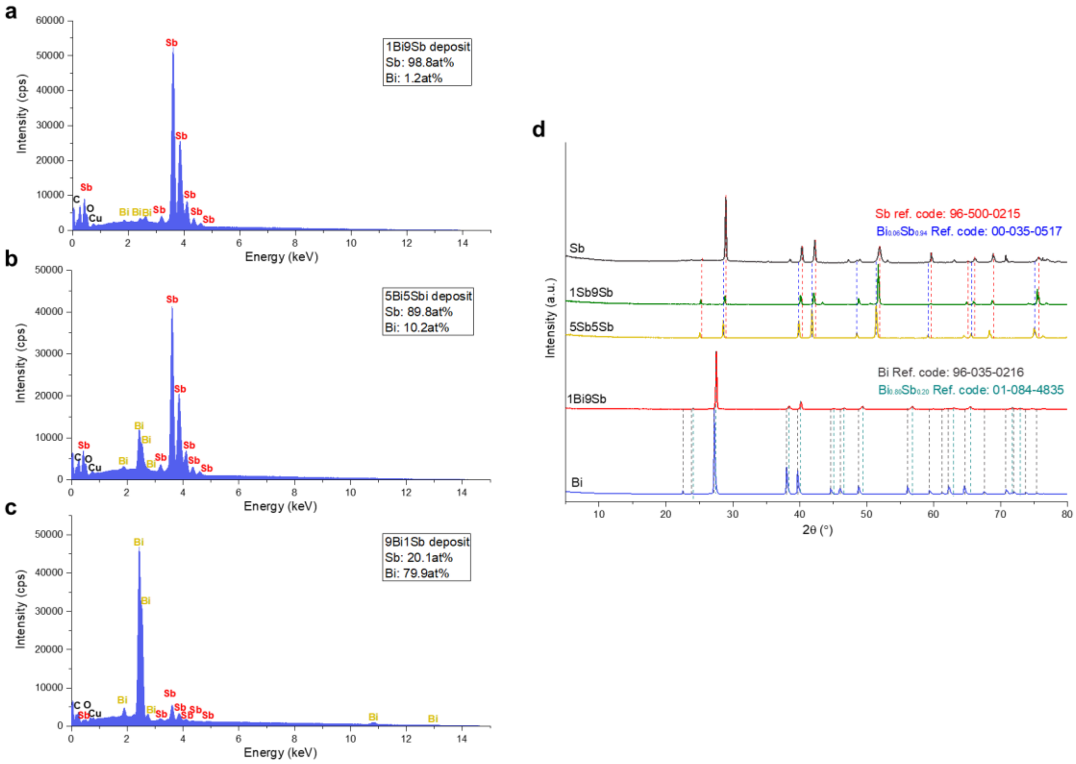

Supplementary Fig. 60 | Compositional and structural characterization of BiSb alloy electrodeposits obtained at a current density of 10 mA cm^{-2} and a fixed areal capacity of 10 mAh cm^{-2} from 6 m $CaCl_2$-based SICEs. a–c, EDS spectra of BiSb alloys obtained from in 0.1 m $BiCl_3$ + 0.9 m $SbCl_3$ + 6 m $CaCl_2$ electrolyte (a), 0.5 m $BiCl_3$ + 0.5 m $SbCl_3$ + 6 m $CaCl_2$ electrolyte (b), and 0.9 m $BiCl_3$ + 0.1 m $SbCl_3$ + 6 m $CaCl_2$ electrolyte (c). **d**, Corresponding XRD patterns. Bi and Sb XRD patterns were obtained from Fig. 3p of Bi and Sb electrodeposits.

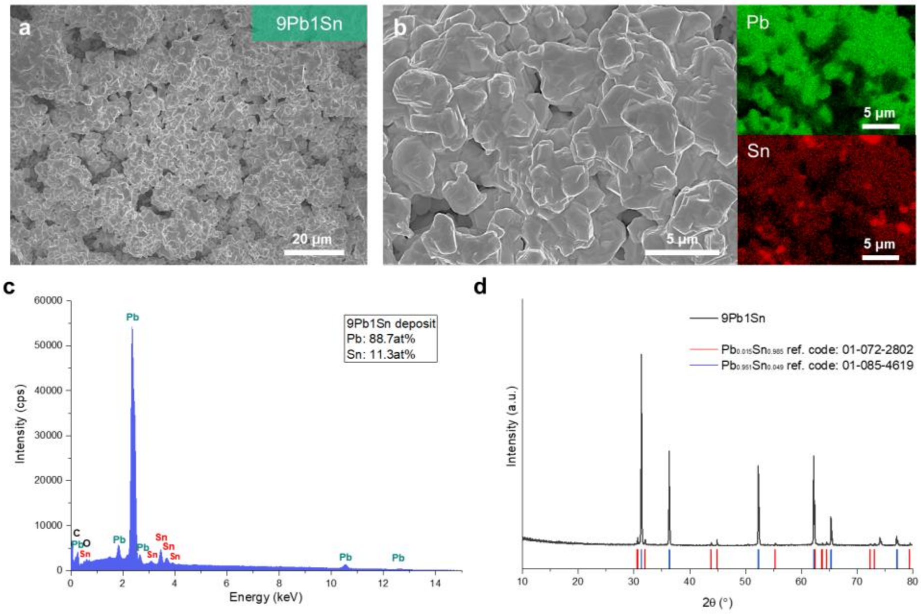

Supplementary Fig. 61 | Morphological and compositional characterization of PbSn alloy electrodeposits obtained at a current density of 10 mA cm^{-2} and a fixed areal capacity of 10 mAh cm^{-2} from 6 m $CaCl_2$-based SICEs. **a**, SEM image PbSn alloy deposit. **b**, **c**, Corresponding EDS elemental map (b) and spectra (c). **d**, XRD pattern of PbSn alloy deposit. PbSn deposit (denoted as 9Pb1Sn) was obtained from 0.36 m $PbCl_2$ + 0.04 m $SnCl_2$ + 6 m $CaCl_2$ electrolyte.

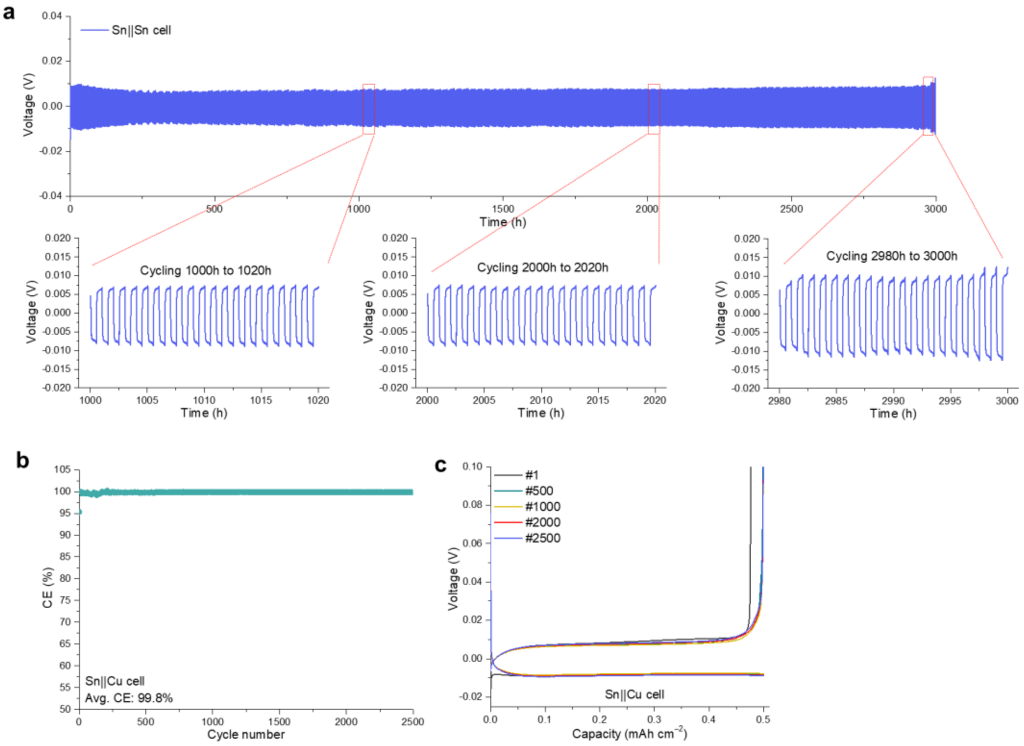

Supplementary Fig. 62 | Electrochemical Sn plating/stripping performance in 1 m $SnCl_2$ + 6 m $CaCl_2$ electrolyte. a, Cycling stability of the Sn||Sn symmetric cell operated at a current density of 1 mA cm^{-2} with an areal capacity of 0.5 mAh cm^{-2}. **b**, **c**, CE (b) and corresponding voltage-capacity profiles (c) of the Sn||Cu asymmetric cell under a current density of 1 mA cm^{-2} and a fixed plated areal capacity of 0.5 mAh cm^{-2}.

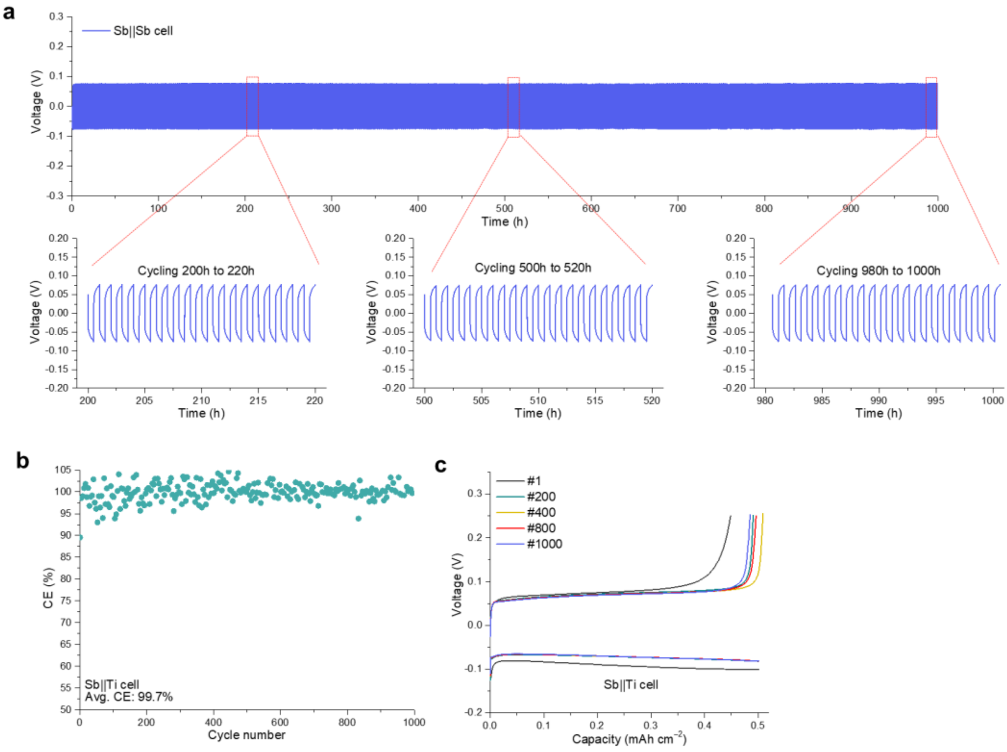

Supplementary Fig. 63 | Electrochemical Sn plating/stripping performance in 1 m $SbCl_3$ + 6 m $CaCl_2$ electrolyte. a, Cycling stability of the Sb||Sb symmetric cell operated at a current density of 1 mA cm^{-2} with an areal capacity of 0.5 mAh cm^{-2}. **b**, **c**, CE (b) and corresponding voltage-capacity profiles (c) of the Sb||Ti asymmetric cell under a current density of 1 mA cm^{-2} and a fixed plated areal capacity of 0.5 mAh cm^{-2}.

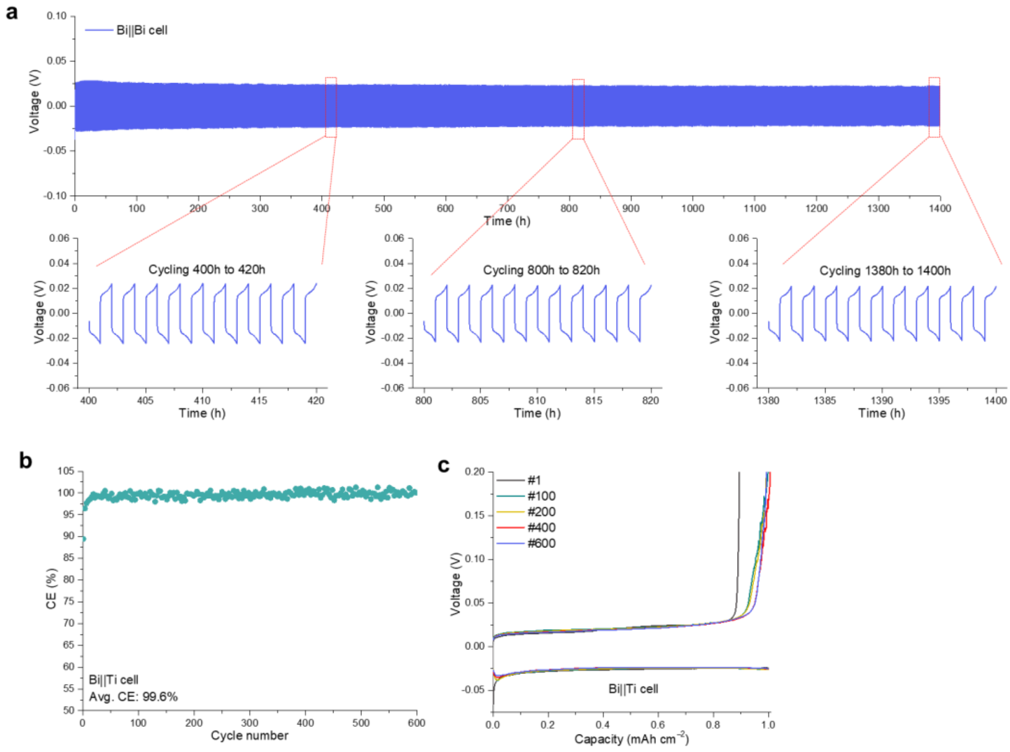

Supplementary Fig. 64 | Electrochemical Bi plating/stripping performance in 1 m $BiCl_3$ + 6 m $CaCl_2$ electrolyte. a, Cycling stability of the Bi||Bi symmetric cell operated at a current density of 1 mA cm^{-2} with an areal capacity of 1 mAh cm^{-2}. **b**, **c**, CE (b) and corresponding voltage-capacity profiles (c) of the Bi||Ti asymmetric cell under a current density of 1 mA cm^{-2} and a fixed plated areal capacity of 1 mAh cm^{-2}.

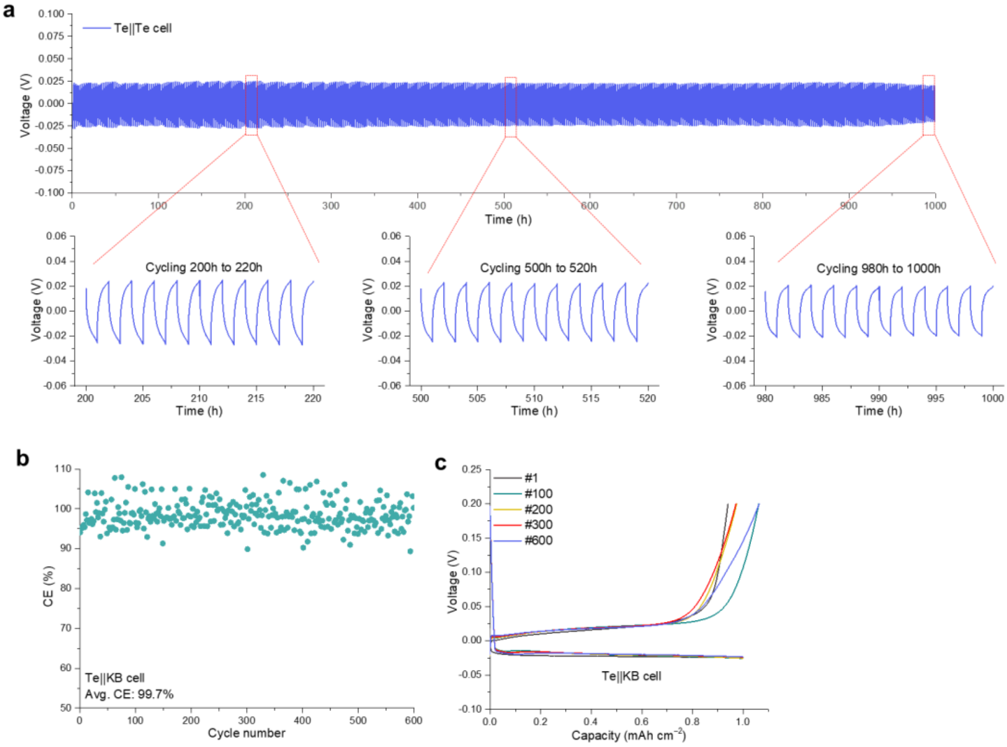

Supplementary Fig. 65 | Electrochemical Te plating/stripping performance in 1 m $TeCl_4$ + 6 m $CaCl_2$ electrolyte. a, Cycling stability of the Te||Te symmetric cell operated at a current density of 1 mA cm^{-2} with an areal capacity of 1 mAh cm^{-2}. **b**, **c**, CE (b) and corresponding voltage-capacity profiles (c) of the Te||KB asymmetric cell under a current density of 1 mA cm^{-2} and a fixed plated areal capacity of 1 mAh cm^{-2}.

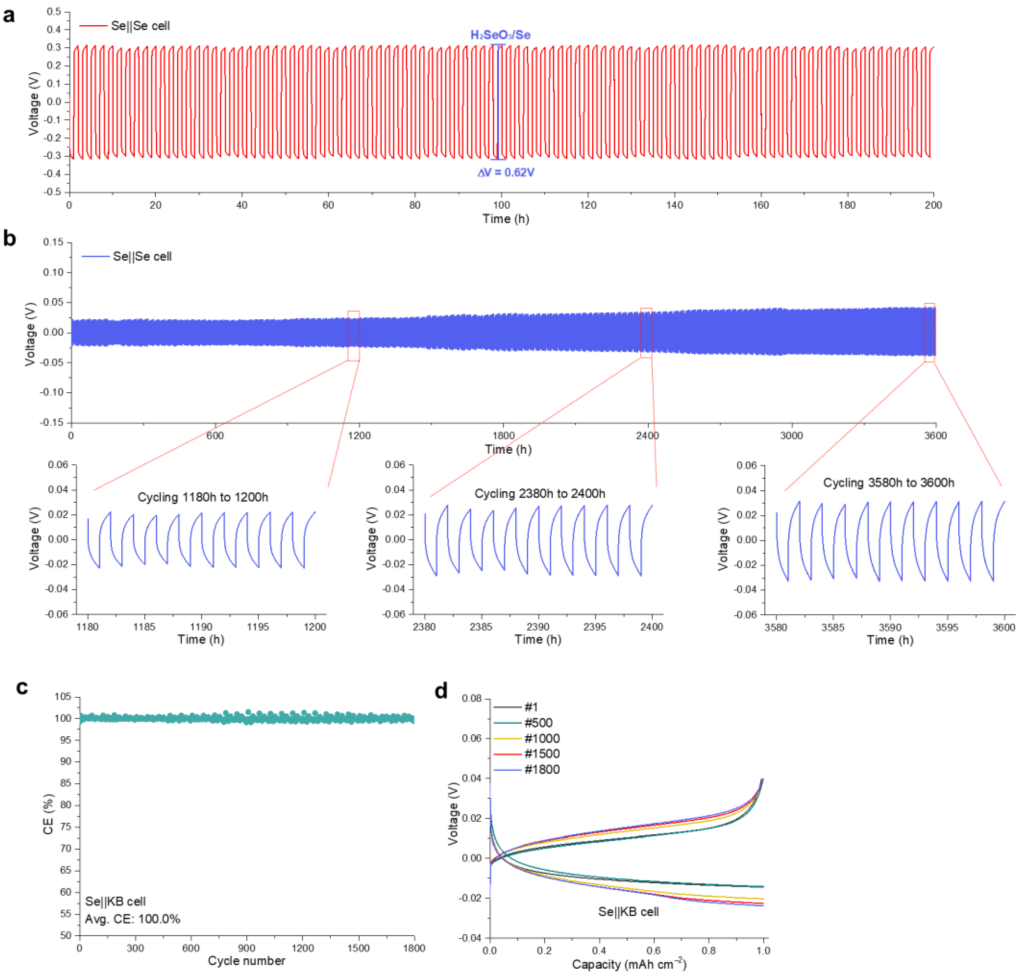

Supplementary Fig. 66 | Enhanced electrochemical Se plating/stripping performance in SICE. a, **b**, Cycling stability of the Se||Se symmetric cells operated at a current density of 1 mA cm^{-2} with an areal capacity of 1 mAh cm^{-2} in 1 m $SeCl_4$ electrolyte (a) and 1 m $SeCl_4$ + 6 m $CaCl_2$ electrolyte (b), As evidenced by Se||Se symmetric cells, the Se/H_2SeO_3 redox couple exhibits a substantially higher plating/stripping overpotential (~620 mV) compared to the Se/$SeOCl_2$ system (~50 mV). **c**, **d**, CE (c) and corresponding voltage-capacity profiles (d) of the Se||KB asymmetric cell under a current density of 1 mA cm^{-2} and a fixed plated areal capacity of 1 mAh cm^{-2}.

Supplementary Note 9. Evaluation of heavy p-block electrochemical reversibility enabled by $CaCl_2$-based SICEs (Supplementary Figs. 67–75)

To assess the electrochemical reversibility of HPEs (Pb, Sn, Sb, Bi, Te, and Se) in $CaCl_2$-based SICEs, symmetric HPE cells were subjected to 50 plating/stripping cycles, after which they were disassembled for post-cycling analysis. SEM images across multiple magnifications reveal that all cycled HPE electrodes retain their structural integrity without the emergence of dendrites, cracks, or obvious degradation (Supplementary Fig. 67). Specifically, Pb and Sn electrodes (Supplementary Fig. 67a, b) preserve their compact polycrystalline faceted architectures with well-defined grain boundaries, indicative of stable morphology during repeated plating and stripping. The Sb electrode shows a densely packed nanoparticulate film (Supplementary Fig. 67c), and Bi electrode retains its regularly lamellar structure without exfoliation or fragmentation (Supplementary Fig. 67d). Meanwhile, Te and Se electrodes exhibit homogeneously distributed particle-like morphologies without secondary phase growth or agglomeration (Supplementary Fig. 67e, f). Complementary XRD analyses confirm the preservation of the primary crystalline phases for all HPEs, with no detectable impurity peaks or byproduct signals after cycling (Supplementary Fig. 68). It should be noted that the post-cycling XRD pattern of Se electrode is not amorphous, primarily because the pristine Se powder is crystalline (Supplementary Fig. 51e, k, q). After 50 cycles, both crystalline and amorphous Se phases coexist, which gives rise to the observed crystalline diffraction pattern. This is further confirmed by the XRD pattern of Se deposited on KB-coated current collector after 50 cycles, which is fully amorphous (Supplementary Fig. 75f). Using asymmetric HPE cells, we further conducted morphological and structural characterizations of Pb, Sn, Sb, Bi, Te, and Se deposits on current collectors after 50 plating/stripping cycles in $CaCl_2$-based SICEs (Supplementary Figs. 69–75). The post-cycled Pb deposit onto current collector still shows uniform grain sizes and well-defined facts, with cross-sectional SEM and atomic-resolution HAADF-STEM imaging confirming the (111) lattice fringe (~0.29 nm) with FFT pattern, corresponding to Pb crystal, without detectable impurity phases (Supplementary Fig. 69). The post-cycled Sn deposit also maintains faceted polygonal crystals with sharp and well-defined edges, with HAADF-STEM analyses showing clear (200) plane (~0.29 nm) of Sn crystal (Supplementary Fig. 70). In the case of post-cycled Sb deposit, densely packed spherical grains are observed, suggesting highly uniform deposition without significant coarsening; corresponding HAADF-STEM imaging reveals well-resolved (012) plane (~0.31 nm) and a sharp FFT pattern of Sb crystal (Supplementary Fig. 71). The Bi deposit exhibits the interconnected lamellar grains, maintaining layered features with observable grain boundaries, and atomic-resolution imaging confirms the retention of the Bi (012) plane (0.33 nm) after post-cycling plating behavior (Supplementary Fig. 72). The post-cycled Te deposit exhibits a compact, bulk-like morphology, and HAADF-STEM analysis reveals a distinct (011) lattice spacing of ~0.33 nm, confirming preservation of the crystalline framework (Supplementary Fig. 73). In contrast, the Se deposit remains amorphous after cycling, with SEM imaging showing a smooth morphology and HAADF-STEM analysis revealing the absence of lattice fringes and only diffuse FFT signals, consistent with the stability of its amorphous structure (Supplementary Fig. 74). In addition, the EDS spectrum confirms the high-purity Se deposition (inset of Supplementary Fig. 74c). Subsequent XRD pattern analyses of the HPE deposits on current collectors after 50 plating/stripping cycles reveal that the crystalline phases of all HPEs are well preserved (Supplementary Fig. 75a–e). In the case of Se, the deposited phase is amorphous

(Supplementary Fig. 75f). These observations are consistent with the HAADF-STEM mapping results. Therefore, no dendritic growth, pulverization, or secondary phase formation was observed after 50 cycles for any HPE, either on the cycled electrodes or on the deposits collected from current collectors. These observations underscore the ability of the $CaCl_2$-based SICE system to maintain structural integrity and support highly reversible electrochemistry across a wide range of HPEs.

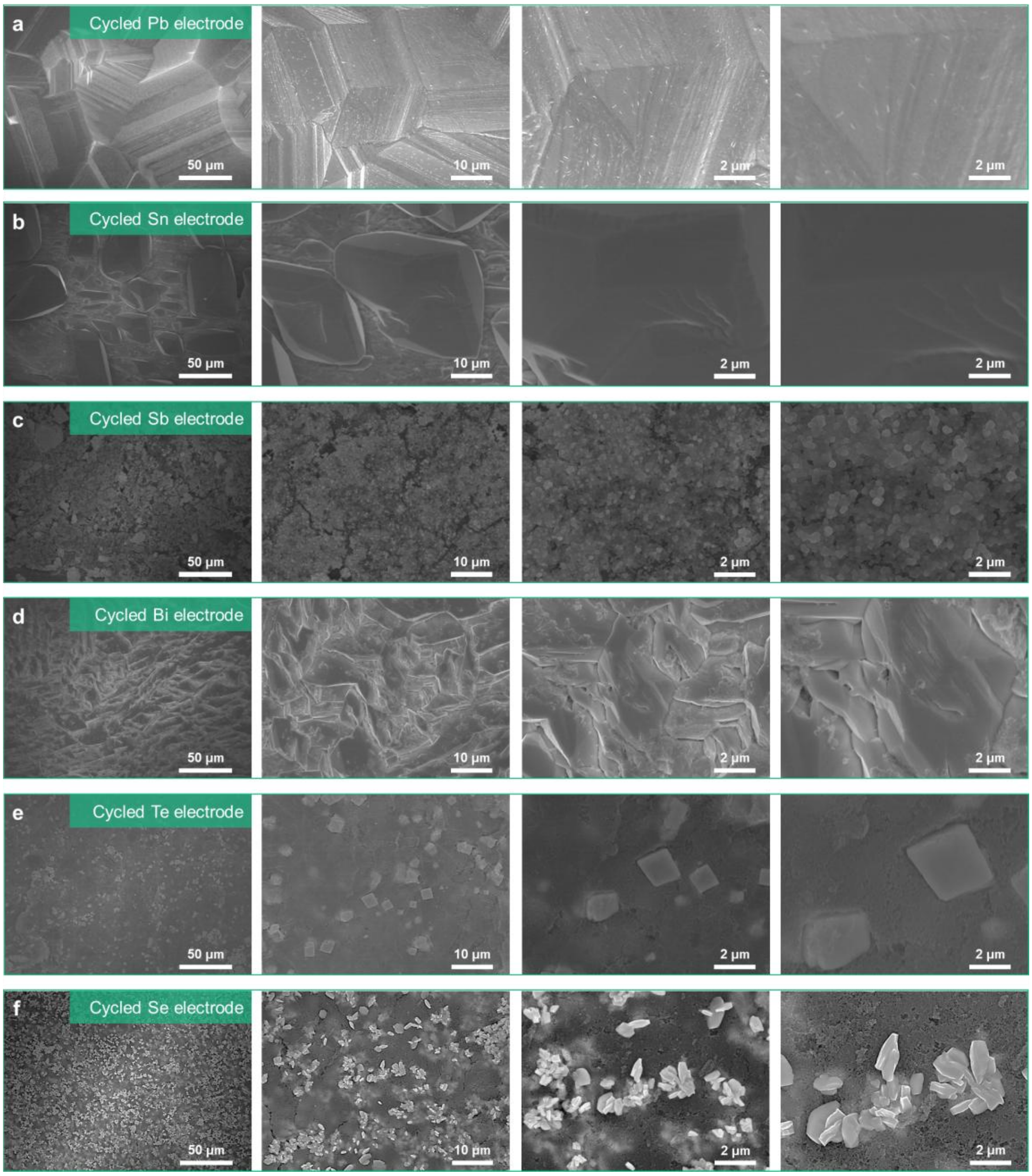

Supplementary Fig. 67 | Morphologies of cycled HPE electrodes in 6 m $CaCl_2$-based SICEs. a–f, SEM images at different magnifications of Pb (a), Sn (b), Sb (c), Bi (d), Te (e), and Se (f) electrodes obtained for the corresponding symmetric cells after 50 stripping/plating cycles.

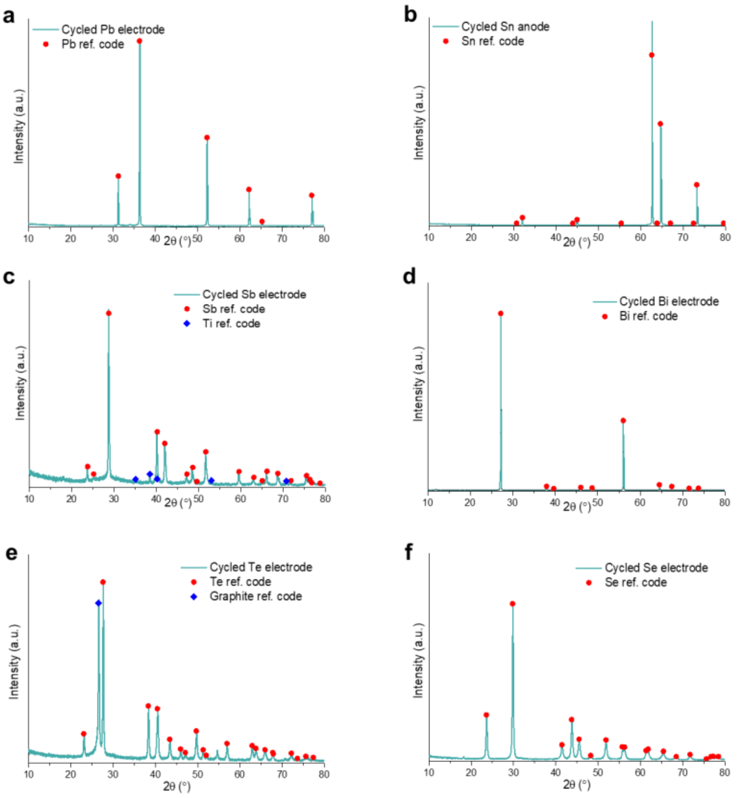

Supplementary Fig. 68 | Structural characterization of cycled HPE electrodes in 6 m $CaCl_2$-based SICEs. a–f, XRD patterns of Pb (a), Sn (b), Sb (c), Bi (d), Te (e), and Se (f) electrodes obtained for the corresponding symmetric cells after 50 stripping/plating cycles.

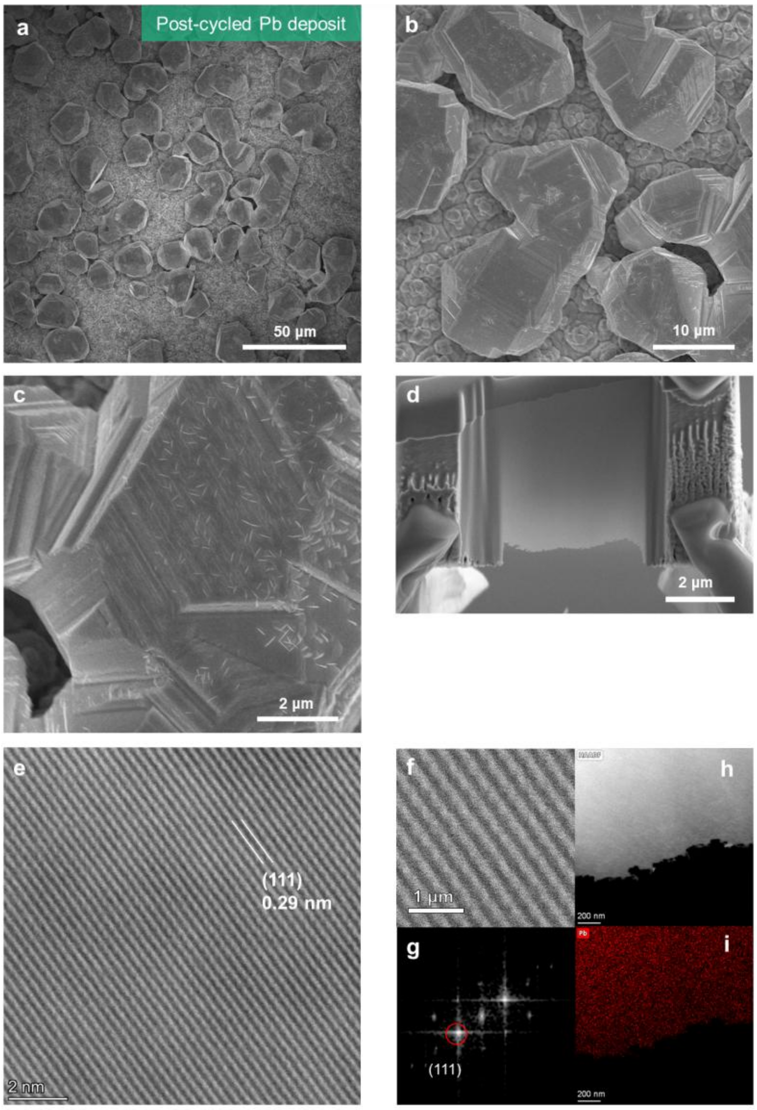

Supplementary Fig. 69 | Morphological and structural characterization of Pb electrodeposit from the Pb||Cu cell in 0.4 m $PbCl_2$ + 6 m $CaCl_2$ electrolyte after 50th plating cycle at 1 mA cm^{-2} and 1 mAh cm^{-2} on Cu foil. a–c, SEM images of Pb deposits at increasing magnifications. **d**, Cross-sectional SEM image of the FIB-prepared Pb layer. **e–g**, Atomic-resolution HAADF-STEM image (e) with showing an enlarged atomic arrangement (f), and corresponding FFT pattern (g). **h**, **i**, HAADF-STEM image and corresponding EDS elemental map for Pb.

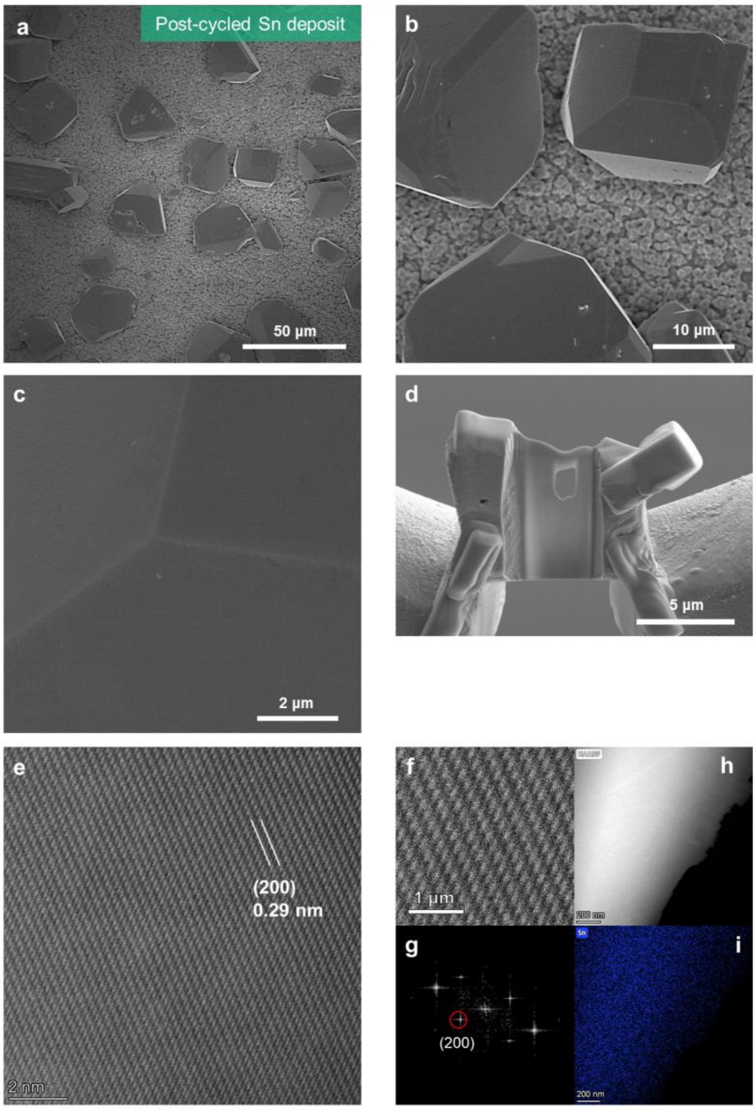

Supplementary Fig. 70 | Morphological and structural characterization of Sn electrodeposit from the Sn||Cu cell in 1 m $SnCl_2$ + 6 m $CaCl_2$ electrolyte after 50th plating cycle at 1 mA cm^{-2} and 0.5 mAh cm^{-2} on Cu foil. a–c, SEM images of Sn deposits at increasing magnifications. **d**, Cross-sectional SEM image of the FIB-prepared Sn layer. **e–g**, Atomic-resolution HAADF-STEM image (e) with showing an enlarged atomic arrangement (f), and corresponding FFT pattern (g). **h**, **i**, HAADF-STEM image and corresponding EDS elemental map for Sn.

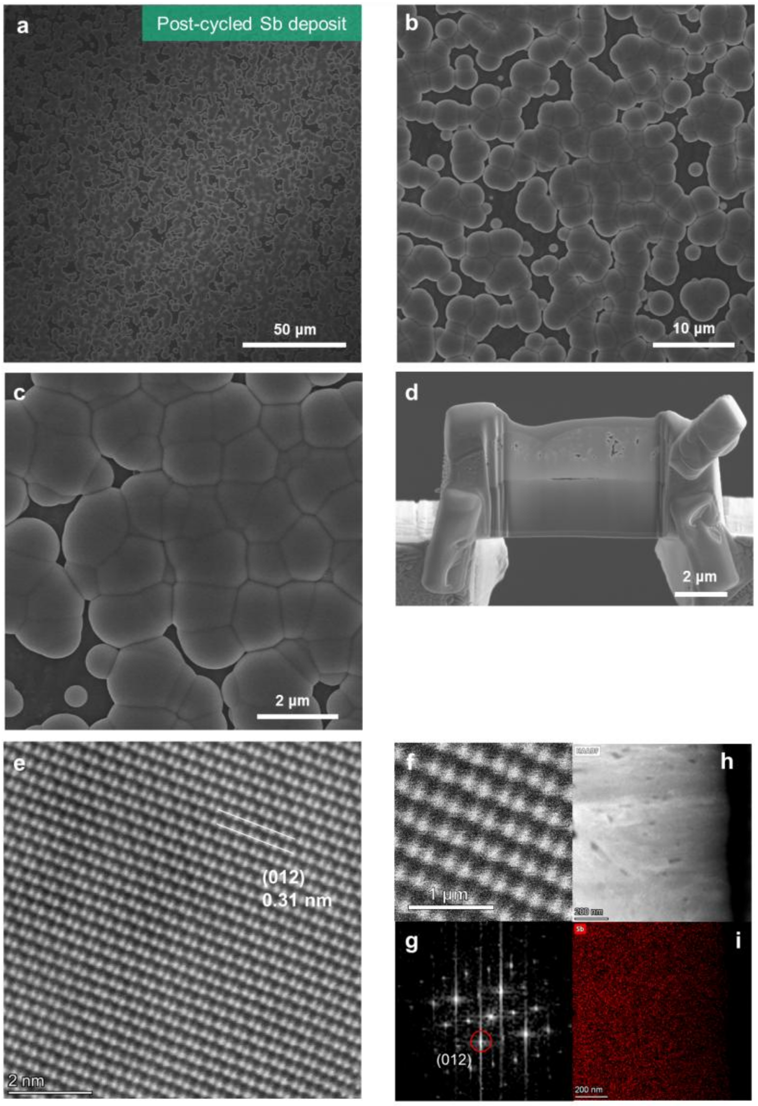

Supplementary Fig. 71 | Morphological and structural characterization of Sb electrodeposit from the Sb||Ti cell in 1 m $SbCl_3$ + 6 m $CaCl_2$ electrolyte after 50th plating cycle at 1 mA cm^{-2} and 0.5 mAh cm^{-2} on Ti foil. a–c, SEM images of Sb deposits at increasing magnifications. **d**, Cross-sectional SEM image of the FIB-prepared Sb layer. **e–g**, Atomic-resolution HAADF-STEM image (e) with showing an enlarged atomic arrangement (f), and corresponding FFT pattern (g). **h**, **i**, HAADF-STEM image and corresponding EDS elemental map for Sb.

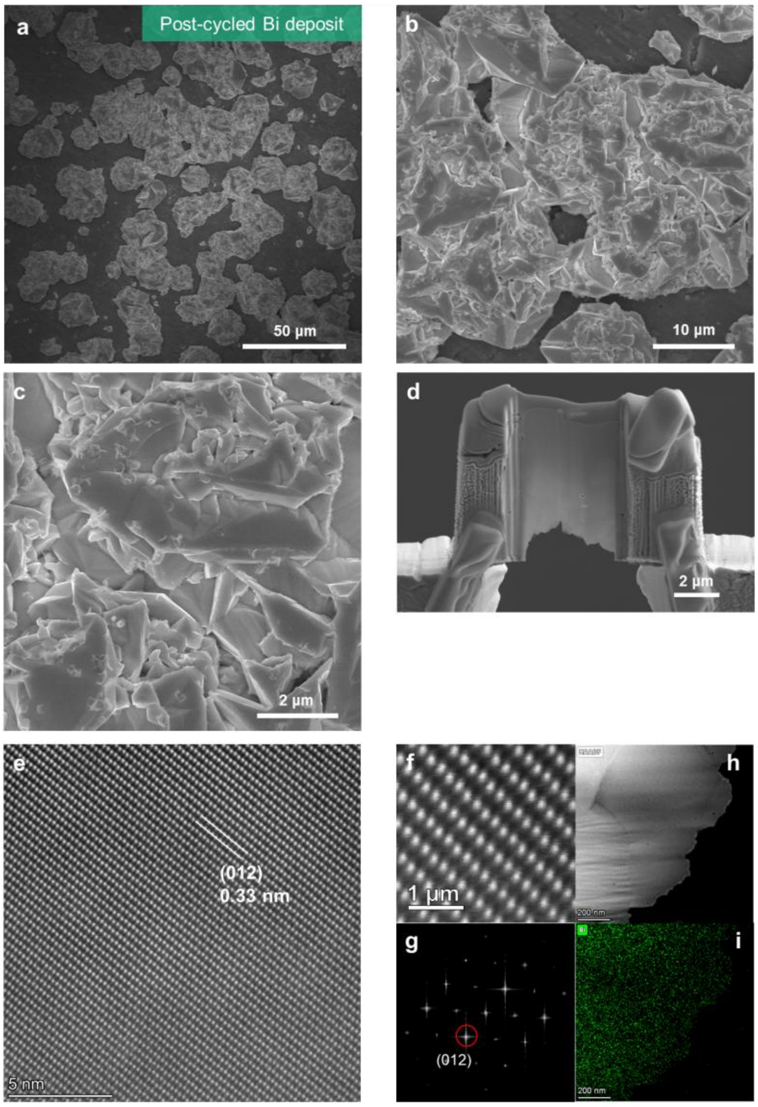

Supplementary Fig. 72 | Morphological and structural characterization of Bi electrodeposit from the Bi||Ti cell in 1 m $BiCl_3$ + 6 m $CaCl_2$ electrolyte after 50th plating cycle at 1 mA cm^{-2} and 1 mAh cm^{-2} on Ti foil. a–c, SEM images of Bi deposits at increasing magnifications. **d**, Cross-sectional SEM image of the FIB-prepared Bi layer. **e–g**, Atomic-resolution HAADF-STEM image (e) with showing an enlarged atomic arrangement (f), and corresponding FFT pattern (g). **h**, **i**, HAADF-STEM image and corresponding EDS elemental map for Bi.

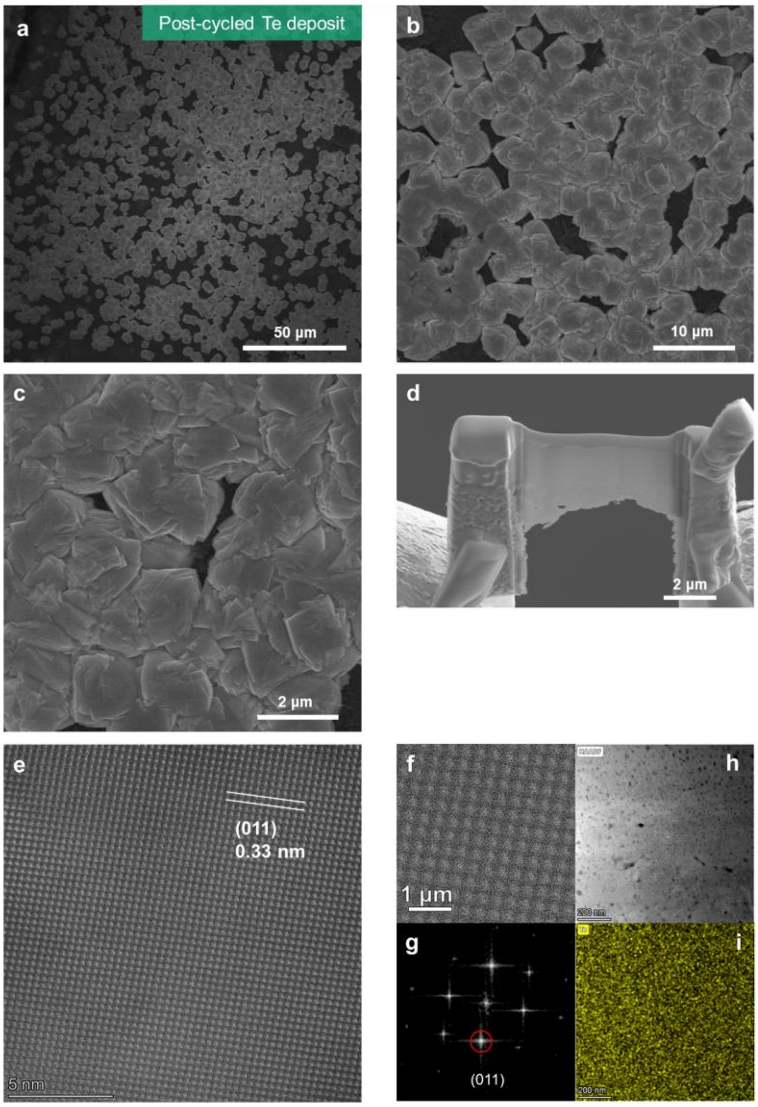

Supplementary Fig. 73 | Morphological and structural characterization of Te electrodeposit from the Te‖KB cell in 1 m $TeCl_4$ + 6 m $CaCl_2$ electrolyte after 50th plating cycle at 1 mA cm^{-2} and 1 mAh cm^{-2} on KB-coated current collector. a–c, SEM images of Te deposits at increasing magnifications. **d**, Cross-sectional SEM image of the FIB-prepared Te layer. **e–g**, Atomic-resolution HAADF-STEM image (e) with showing an enlarged atomic arrangement (f), and corresponding FFT pattern (g). **h**, **i**, HAADF-STEM image and corresponding EDS elemental map for Te.

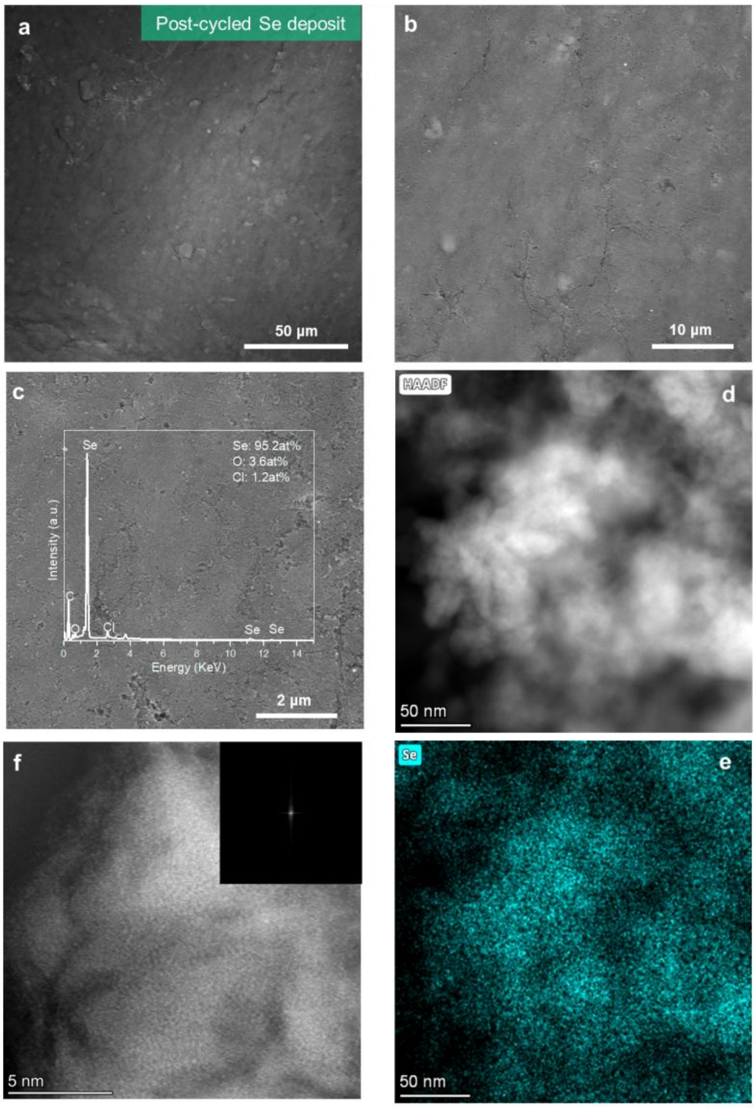

Supplementary Fig. 74 | Morphological and structural characterization of Se electrodeposit from the Se||KB cell in 1 m $SeCl_4$ + 6 m $CaCl_2$ electrolyte after 50th plating cycle at 1 mA cm^{-2} and 1 mAh cm^{-2} on KB-coated current collector. a–c, SEM images of Se deposits at increasing magnifications. Inset is the corresponding SEM-coupled EDS spectra. **d**, **e**, HAADF-STEM image and corresponding EDS elemental map for Se. **f**, Atomic-resolution HAADF-STEM image. Inset is the FFT pattern.

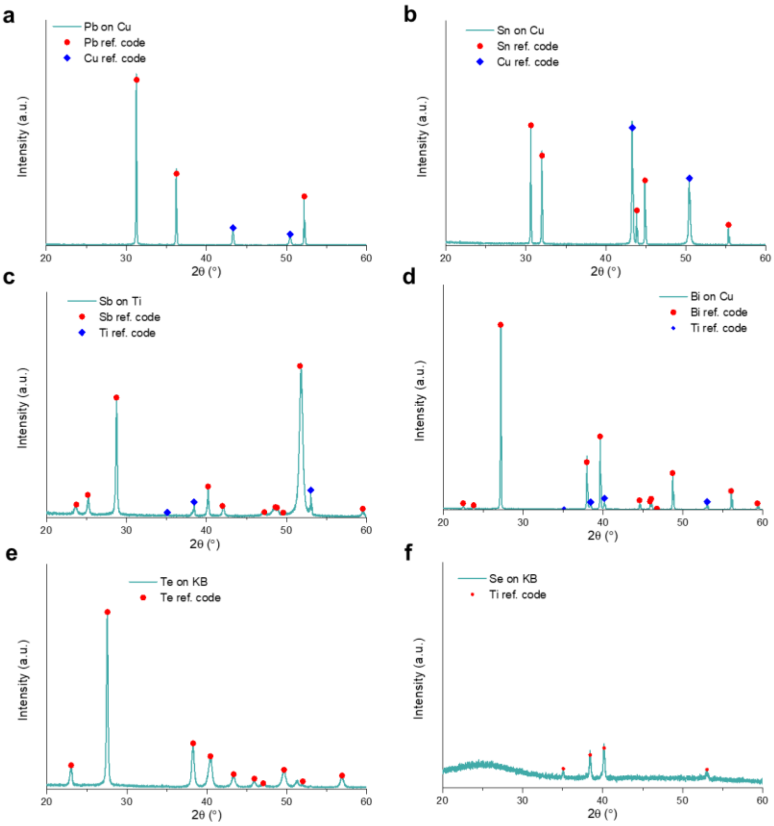

Supplementary Fig. 75 | Structural characterization of electrodeposited HPEs on current collectors from corresponding asymmetric cells after 50th plating cycle in 6 m $CaCl_2$-based SICEs. a–f, XRD patterns of Pb (a), Sn (b), Sb (c), Bi d), Te (e), and Se (f) deposits collected after 50 cycles from the corresponding asymmetric cells.

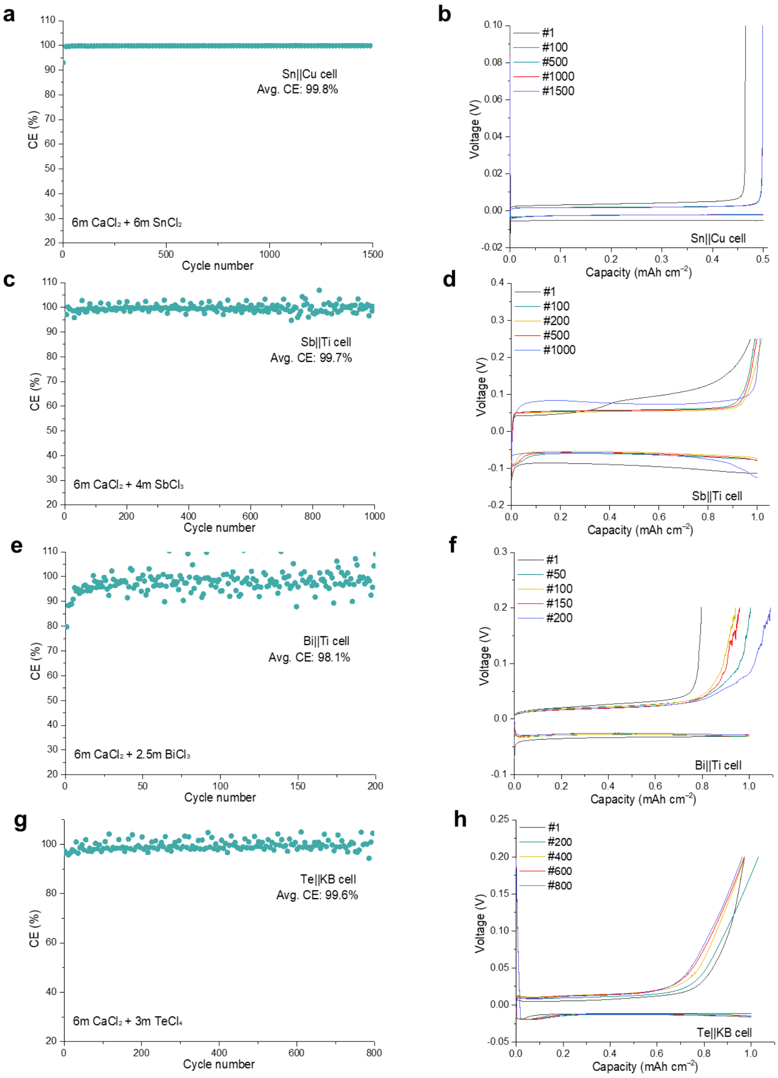

Supplementary Fig. 76 | Evaluation of reversible heavy p-block electrochemistry using asymmetric cells in 6 m $CaCl_2$-based SICEs at high HPE cations concentrations. a–h, Plating/stripping behaviors of Sn in 6 m $SnCl_2$ + 6 m $CaCl_2$ (a, b), Sb in 4 m $SbCl_3$ + 6 m $CaCl_2$ (c, d), Bi in 2.5 m $BiCl_3$ + 6 m $CaCl_2$ (e, f), and Te in 3 m $TeCl_4$ + 6 m $CaCl_2$ (g, h), all tested at a fixed current density of 1 mA cm^{-2} with plated areal capacities of 0.5 or 1 mAh cm^{-2}. Corresponding CE plots are shown in (a, c, e, g). Corresponding voltage-capacity curves are shown in (b, d, f, h).

Supplementary Note 10. Enabling rechargeable aqueous batteries with HPE electrodes via SICEs (Supplementary Fig. 77e, f, and Supplementary Fig. 80c–f)

To further validate the general applicability of aqueous HPE-based batteries, we illustrated a schematic configuration of Bi-based cells employing $BiCl_3$ cathode (Supplementary Fig. 77e), with the Cl^-/Cl_2 redox couple selected as a representative system for experimental evaluation. Using a 1 m $BiCl_3$ + 6 m $CaCl_2$ electrolyte, the Bi||$BiCl_3$ full battery exhibited stable and overlapping charge/discharge profiles with a high output voltage of ~1.2 V at 10 C (174 mA g^{-1} as 1 C), maintaining consistent performance over 150 cycles (Supplementary Fig. 80c, d). It highlights the excellent electrochemical reversibility, high-rate capability, and capacity retention enabled by the Cl^--coordinate SICE. This finding underscores the potential of multielectron Bi^{3+}/Bi conversion chemistry for high-power aqueous energy storage applications. In addition, we explored the electrochemical feasibility of Sb-based batteries to access deeper redox states and validate the broader applicability of the SICE. Specifically, we constructed a quasi-Sb-symmetric Sb||$SbCl_3$ full battery using a 1 m $SbCl_3$ + 6 m $CaCl_2$ electrolyte, where both the anode and cathode utilize Sb-based redox couples. The anode operates via the reversible Sb^{3+}/Sb plating/stripping process, while the cathode undergoes a multielectron Sb^{5+}/Sb^{3+} conversion reaction, enabling a total cell voltage of ~0.7 V (Supplementary Fig. 77f). This Sb-symmetric configuration not only simplifies cell design but also leverages the full redox window of Sb species. Impressively, the Sb||$SbCl_3$ full battery delivered a high specific capacity of 217 mAh g^{-1} and retained ~90% of its initial capacity over 8,000 cycles at a rate of 5 C (1 C = 235 mA g^{-1}; Supplementary Fig. 80e, f), with minimal polarization. These results affirm the exceptional cycling stability and redox reversibility achieved in the chloride-coordinate salting-in environment, and highlight the promise of scalable aqueous Sb-based multielectron battery systems for long-life energy storage applications. Electrochemical characterization revealed that the $Sb^{3+} \leftrightarrow Sb^{5+}$ redox process proceeds with excellent reversibility under the Cl^--rich salting-in environment. We attribute this behavior to a solid–solid phase conversion between $SbCl_3$ and $SbCl_5$. The successful realization of reversible Sb^{5+}/Sb^{3+} redox chemistry is particularly notable, because of the inherent instability of HPE cations in water. Given that the primary objective of this study at current stage is to demonstrate the feasibility and diversity of aqueous HPE-based battery chemistries, a detailed mechanistic analysis of the $SbCl_3/SbCl_5$ conversion was not conducted. Nonetheless, we believe these findings point to a promising direction for future investigation, where the stabilization of high-valent species in water could be further elucidated and potentially extended to other HPE systems.

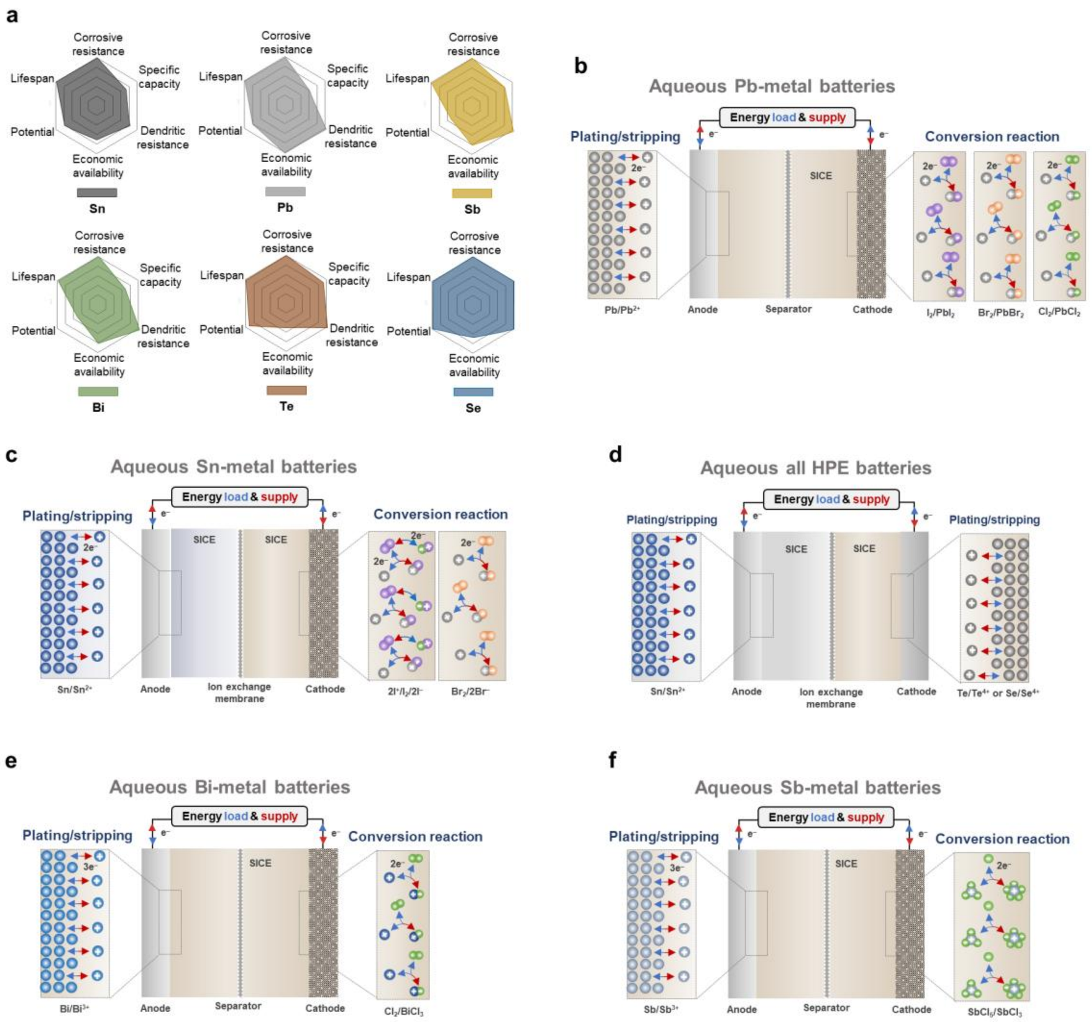

Supplementary Fig. 77 | Promising SICE-enabled HPE-based battery architectures. a, Radar plots comparing key electrochemical and practical metrics of various HPEs as electrode materials. **b**, Schematic of a rechargeable Pb-metal battery paired with conversion-type cathodes. The anode operates via the $[PbCl_3]^-/Pb$ couple, while the cathode involves I_2/PbI_2, $Br_2/PbBr_2$, or $Cl_2/PbCl_2$ conversion reactions. **c**, Schematic of an aqueous Sn-metal battery paired with I_2 or KBr cathodes. The anode is based on the $[SnCl_3]^-/Sn$, whereas the cathode follows a four-electron $2I^+/I_2/2I^-$ or $2KBr/Br_2$ redox reaction. An ion-exchange membrane prevents Sn^{2+} crossover and subsequent oxidation to Sn^{4+} during charging at cathode side. **d**, Schematic of a hybrid Sn-metal battery paired with four-electron Te or Se cathodes. The anode is governed by the $[SnCl_3]^-/Sn$ couple, and the cathode involves the $[TeCl_6]^{2-}/Te$ or $SeOCl_2/Se$ redox pair, separated by an ion-exchange membrane to prevent cross-contamination. **e**, Schematic of a Bi||$BiCl_3$ battery based on the $[BiCl_6]^{3-}/Bi$ anode and $BiCl_3/Cl_2$ cathode. **f**, Schematic of a quasi-symmetric Sb//$SbCl_3$ battery operating between the $[SbCl_4]^-/Sb$ anode and $SbCl_5/SbCl_3$ cathode couples.

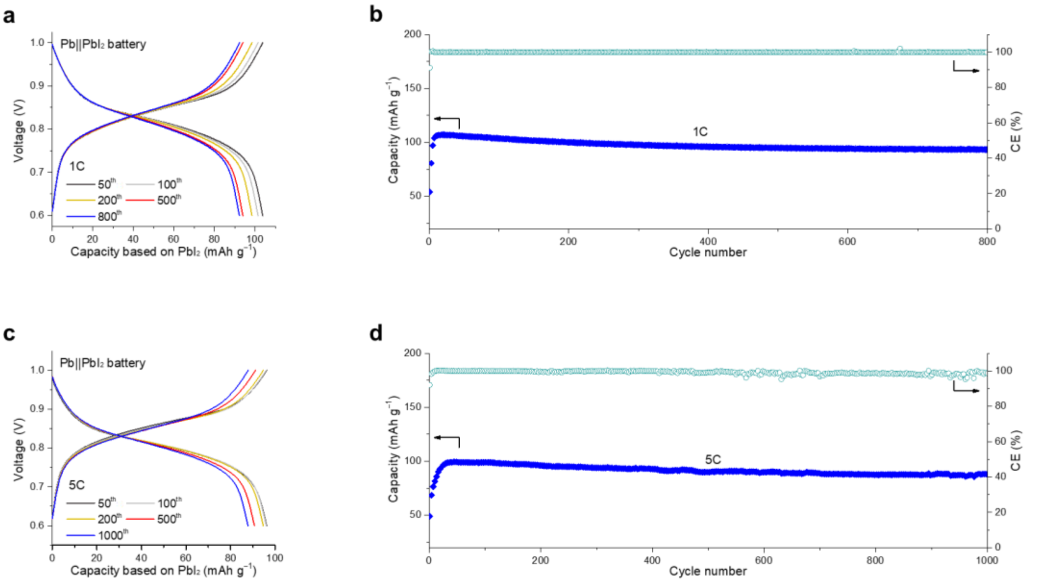

Supplementary Fig. 78 | Rechargeable aqueous Pb||PbI_2 full batteries in 0.4 m $PbCl_2$ + 6 m $CaCl_2$ electrolyte. a, **b**, Galvanostatic charge/discharge profiles (a) and cycling performance (b) of Pb||PbI_2 full battery at 1 C. **c**, **b**, Galvanostatic charge/discharge profiles (c) and cycling performance (d) of Pb||PbI_2 full battery at 5 C.

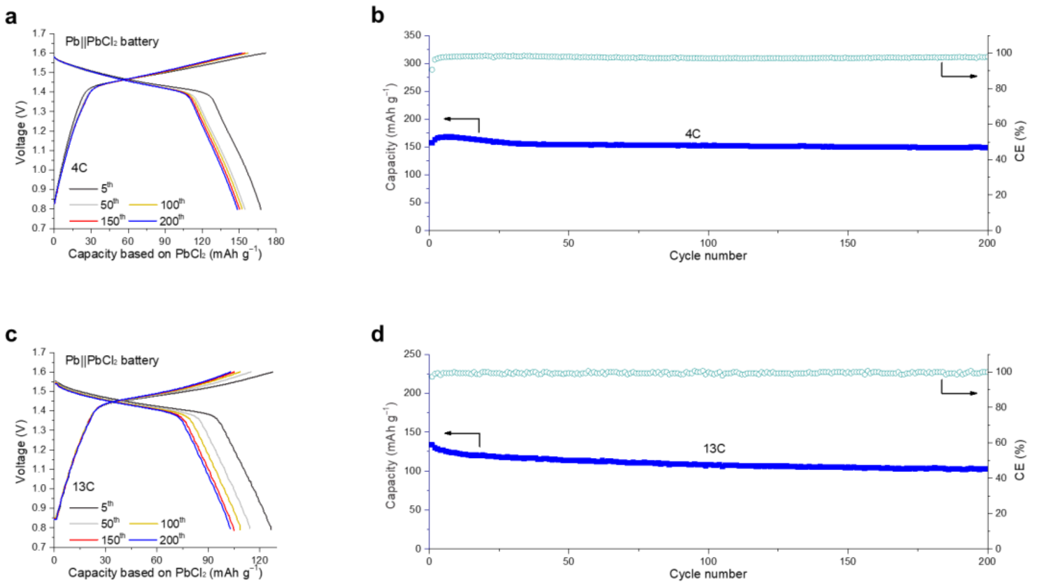

Supplementary Fig. 79 | Rechargeable aqueous Pb||$PbCl_2$ full batteries in 0.4 m $PbCl_2$ + 6 m $CaCl_2$ electrolyte. a, **b**, Galvanostatic charge/discharge profiles (a) and cycling performance (b) of Pb||$PbCl_2$ full battery at 4 C. **c**, **d**, Galvanostatic charge/discharge profiles (c) and cycling performance (d) of Pb||$PbCl_2$ full battery at 13 C.

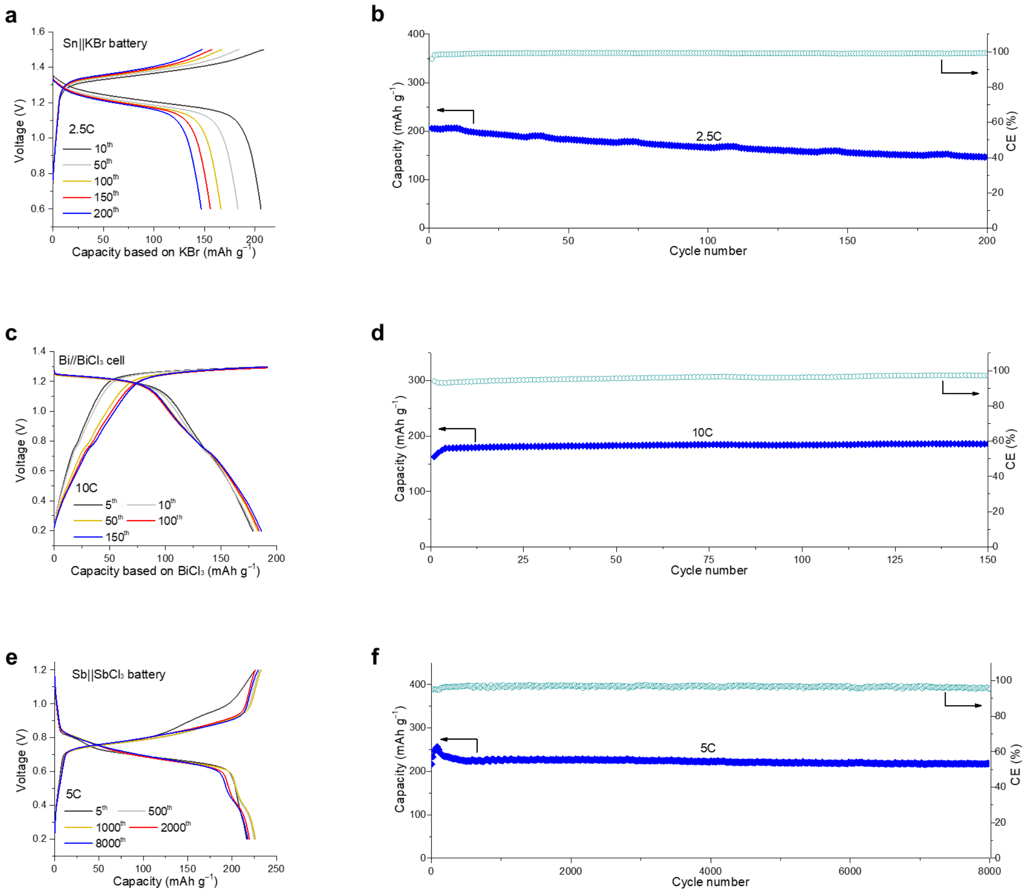

Supplementary Fig. 80 | Rechargeable aqueous HPEs-based batteries in 6 m $CaCl_2$-based SICEs. a, **b**, Galvanostatic charge/discharge profile (a) and cycling performance (b) of Sn||KBr full battery at 2.5 C. **c**, **d**, Galvanostatic charge/discharge profile (c) and cycling performance (d) of Bi||$BiCl_3$ full battery at 10 C. **e**, **f**, Galvanostatic charge/discharge profile (e) and cycling performance (f) of Sb||$SbCl_3$ battery at 5 C.

Supplementray References

1. Murray, J. S. & Politzer, P. Molecular electrostatic potentials and noncovalent interactions. *Wiley Interdiscip. Rev.:Comput. Mol. Sci.* **7**, e1326 (2017).
2. Persson, I. Hydrated metal ions in aqueous solution: How regular are their structures? *Pure Appl. Chem.* **82**, 1901–1917 (2010).
3. Sun, Q. The Raman OH stretching bands of liquid water. *Vib. Spectrosc.* **51**, 213–217 (2009).
4. Behnajady, B., Moghaddam, J., Behnajady, M. A. & Rashchi, F. Determination of the optimum conditions for the leaching of lead from zinc plant residues in NaCl–H_2SO_4–$Ca(OH)_2$ media by the taguchi method. *Ind. Eng. Chem. Res.* **51**, 3887–3894 (2012).
5. Wang, Q. et al. Towards highly stable Sn^{2+} electrolyte for aqueous tin batteries using hydroquinone antioxidant. *Angew. Chem., Int. Ed.* **64**, e202418928 (2025).
6. Chang, S. et al. A low-acidity chloride electrolyte enables exceptional reversibility and stability in aqueous tin metal batteries. *Angew. Chem., Int. Ed.* **64**, e202414346 (2024).
7. Currie, M. et al. Chlorostannate(II) ionic liquids: Speciation, Lewis acidity, and oxidative stability. *Inorg. Chem.* **52**, 1710–1721 (2013).
8. Hathaway, E. J. & Maroni, V. A. Structural studies of stannous chloride-potassium chloride melts by Raman spectroscopy. *J. Phys. Chem.* **76**, 2796–2798 (1972).
9. Ullah, I. et al. Concentrated chloride electrolytes enable high-efficiency, long-cycling, and dendrite-free aqueous trivalent antimony batteries. *Angew. Chem., Int. Ed.* **64**, e202502279 (2025).
10. Milne, J. Spectrophotometric studies on Sb(III) in hydrochloric-acid solutions. *Can. J. Chem.* **53**, 888–893 (1975).
11. El-Adel, L., Ouasri, A., Rhandour, A. & Hajji, L. Raman-Infrared spectroscopy, thermal behaviour, dielectric, and UV-fluorescence studies of $[C_6H_5NH_3]_3BiCl_6 \cdot 3H_2O$. *Solid State Commun.* **340**, 114541 (2021).
12. Berg, R. W., Poulsen, F. W. & Bjerrum, N. J. Low temperature vibrational spectroscopy. I. Hexachlorotellurates. *J. Chem. Phys.* **67**, 1829–1837 (1977).
13. Chou, I.-M., Wang, R. & Fang, J. In situ redox control and Raman spectroscopic characterisation of solutions below 300 °C. *Geochem. Persp. Let.* **20**, 1–5 (2021).
14. Milne, J. Raman spectra of seleninyl halides. *Spectrochim. Acta, Part A* **38**, 569–574 (1982).